

Reconstruction of Complex Dynamical Systems Affected by Strong Measurement Noise

Frank Böttcher^{*} and Joachim Peinke[†]

Institute of Physics, University of Oldenburg, D-26111 Oldenburg, Germany

David Kleinhans and Rudolf Friedrich

Institute of Theoretical Physics, University of Münster, D-48149 Münster, Germany

Pedro G. Lind and Maria Haase

University of Stuttgart, Pfaffenwaldring 27, D-70569 Stuttgart, Germany

(Received 16 June 2005; revised manuscript received 18 July 2006; published 1 September 2006)

This Letter reports on a new approach to properly analyze time series of dynamical systems which are spoilt by the simultaneous presence of dynamical noise and measurement noise. It is shown that even strong external measurement noise as well as dynamical noise which is an intrinsic part of the dynamical process can be quantified correctly, solely on the basis of measured time series and proper data analysis. Finally, real world data sets are presented pointing out the relevance of the new approach.

DOI: 10.1103/PhysRevLett.97.090603

PACS numbers: 05.40.Ca, 02.50.Ey, 05.10.Gg

A major challenge in analyzing time series originating from complex systems is to reveal the underlying process dynamics. Typically the simultaneous involvements of nonlinearities, dynamical noise, and measurement noise cause problems for many experimental situations and account for the complexity of this task. The handling of these complications is the central concern of this Letter.

To extract an underlying signal disturbed by noise, linear and nonlinear predictor models or noise reduction schemes are widely used (for discussion see [1] and references therein). Here we choose an alternative approach based on the broad class of Langevin processes, which describes a variety of complex dynamical systems.

Let us consider a one-dimensional Langevin process (the extension to more dimensions is straightforward) that is given by

$$\dot{x} = D^{(1)}(x) + \sqrt{D^{(2)}(x)}\Gamma(t). \quad (1)$$

The term $\Gamma(t)$ represents Gaussian white noise with $\langle \Gamma(t) \rangle = 0$ and $\langle \Gamma(t')\Gamma(t) \rangle = \delta(t - t')$. The terms $D^{(n)}(x)$ are called the drift coefficient ($n = 1$) and the diffusion coefficient ($n = 2$) and reflect the deterministic and the stochastic part, respectively. $\sqrt{D^{(2)}}$ fixes the amplitude of the stochastic part and is referred to as *dynamical noise*. If $D^{(2)}$ depends on x , it is called multiplicative noise; otherwise it is called additive noise.

In recent years a parameter-free reconstruction of the coefficients and thus of the corresponding Langevin process has been achieved [2–6]. It has been successfully demonstrated that traffic flow dynamics [7], the chaotic dynamics of an electronic circuit [8,9], or the human heart beat rhythm [10] can be reconstructed without need of any *a priori* models but just from measured time series and the estimated drift and diffusion coefficients. This estimation is based on the evaluation of the first ($n = 1$) and the

second ($n = 2$) conditional moments:

$$M^{(n)}(x, \tau) = \langle [x(t + \tau) - x(t)]^n \rangle|_{x(t)=x}, \quad (2)$$

from which the coefficients are derived according to

$$D^{(n)}(x) = \lim_{\tau \rightarrow 0} \frac{1}{\tau} M^{(n)}(x, \tau). \quad (3)$$

For ideal time series with a sufficient temporal resolution the coefficients $D^{(n)}(x)$ can unambiguously be obtained from Eq. (3). For real data sets, however, the sampling frequency might be too low to resolve the dynamics properly as was pointed out in [11,12]. For small but finite τ the conditional moments are better approximated by an *Ito-Taylor series expansion* (e.g., [12–14]):

$$\begin{aligned} M^{(1)}(x, \tau) &\approx \tau D^{(1)}(x) + \mathcal{O}(\tau^2), \\ M^{(2)}(x, \tau) &\approx \tau D^{(2)}(x) + \mathcal{O}(\tau^2). \end{aligned} \quad (4)$$

Depending on the process it might be necessary to consider further higher order terms for estimating the coefficients. To finally decide whether an obtained set of coefficients represents the real dynamics at least a consistency check between the statistical properties (moments, probability densities, etc.) of the reconstructed and of the original time series has to be performed (cf. [15]).

Another important effect that complicates a proper estimation of $D^{(n)}$ is the presence of *measurement noise* $\sigma\zeta(t)$ [with $\langle \zeta(t) \rangle = 0$ and $\langle \zeta(t)\zeta(t') \rangle = \delta(t - t')$], which is superimposed on the data. Measurement noise corresponds to a rather unavoidable experimental situation (e.g., [1,16,17]) and means that $y(t) = x(t) + \sigma\zeta(t)$ is examined rather than $x(t)$. For instance, take the measurement of a turbulent velocity time series. The resolution is chosen in such a way that the largest fluctuations (on the largest time scales) are resolved. A certain amount of measurement noise might be negligible for these large scale fluctuations

but can well be significant for the fluctuations on the smallest scales where the fluctuations are much smaller. More generally, the term “measurement noise” refers to any superimposed uncorrelated noise that is present in some complex system; it might even be generated by the complex system itself.

To reconstruct the unknown dynamics $x(t)$ from the accessible $y(t)$ it is thus essential to quantify $\sigma\zeta(t)$ and its influence on the reconstruction of coefficients according to Eqs. (3) and (4), which will be the central concern of this Letter.

In [8,9,18] it has been shown that measurement noise results in an offset term, γ_n , for the conditional moments

$$M^{(n)}(y, \tau) \rightarrow M^{(n)}(x, \tau) + \gamma_n, \quad (5)$$

$$\gamma_1 = 0, \quad \gamma_2 = 2\sigma^2. \quad (6)$$

Any nonzero offset causes a strong overestimation of the coefficients, $D^{(n)}$, because it leads to a divergence of $M^{(n)}(y, \tau)/\tau$ in Eq. (3). In [8] it was therefore proposed to use the offset γ_2 to quantify measurement noise and to take the slope of the conditional moments (as a function of τ) as an estimate of the coefficients.

In this Letter we will show that Eqs. (5) and (6) are restricted to the special case of low measurement noise, that $M^{(1)}(y, \tau)$ must exhibit a τ -independent part (i.e., $\gamma_1 \neq 0$), and that the slope of the conditional moment, $M^{(n)}$, is no longer proportional to the corresponding coefficient, $D^{(n)}$. In Fig. 1 the effect of measurement noise on $M^{(1)}$ is shown for two real world examples, in which a strong offset at $\tau = 0$ causes a divergence of $M^{(1)}/\tau$. Finally, we propose an improved method to quantify measurement noise even for very large noise levels. To this end a general calculation of the conditional moments will be performed. Thus we can explain the measurement noise dependence of the second and the first conditional moment and propose an improved reconstruction of the underlying process. For an Ornstein-Uhlenbeck process the results are analytical; for non-Ornstein-Uhlenbeck processes the corresponding analysis can be performed numerically.

Let us start with the calculation of the conditional moments from the accessible data $y(t)$ spoilt by superimposed measurement noise. Using the definition according to Eq. (2) the following expressions can be derived:

$$\begin{aligned} M^{(1)}(y, \tau) &= \langle y(t + \tau) - y(t) \rangle|_{y(t)=y(x(t)+\sigma\zeta(t))} \\ &= \tau \int D^{(1)}(x)f(x|y)dx + \int (x - y)f(x|y)dx \\ &= m^{(1)}(y, \tau) + \gamma_1(y), \end{aligned} \quad (7)$$

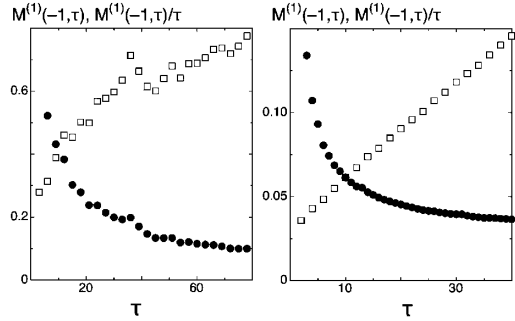


FIG. 1. Both plots show measured $M^{(1)}$ (squares) and $M^{(1)}/\tau$ (circles) as a function of lag τ . The left plot refers to the North Atlantic Oscillation index [23], the right one to an increment time series of financial exchange rates [18]. Units are arbitrary for clarity of presentation. For both systems a significant offset of the first conditional moment is observed causing a divergence of $M^{(1)}/\tau$.

$$\begin{aligned} M^{(2)}(y, \tau) &= \tau \int [2(x - y)D^{(1)}(x) + D^{(2)}(x)]f(x|y)dx \\ &\quad + \sigma^2 + \int (x - y)^2 f(x|y)dx \\ &= m^{(2)}(y, \tau) + \gamma_2(y). \end{aligned} \quad (8)$$

The coefficients, $D^{(n)}$, are implicitly given by the conditional moments that exhibit a τ dependent as well as a τ -independent part, denoted with $m^{(n)}(y, \tau)$ and $\gamma_n(y)$, respectively. According to *Bayes' theorem* the unknown probability density $f(x|y)$ is given by $\frac{f(y|x)p(x)}{\int f(y|x)p(x)dx}$, where $f(y|x)$ denotes nothing other than the distribution of measurement noise. Here we consider Gaussian distributed measurement noise with variance σ^2 . The distribution of the process $x(t)$, given by Eq. (1), is denoted by $p(x)$. For stationary processes the distribution is known to be

$$p(x) = \frac{\mathcal{N}}{D^{(2)}(x)} \exp \left[2 \int_{-\infty}^x \frac{D^{(1)}(x')}{D^{(2)}(x')} dx' \right], \quad (9)$$

where \mathcal{N} denotes a proper normalization factor; cf. [19]. To extract the coefficients from the four equations of Eqs. (7) and (8) we assume for convenience (but not necessarily) that the coefficients can be modeled as polynomials. For instance, take the case of a multiplicative process with $D^{(1)} = d_{11}x$ and $D^{(2)} = d_{20} + d_{21}x + d_{22}x^2$. Then 5 parameters (σ , d_{11} , d_{20} , d_{21} , and d_{22}) have to be derived by minimizing the distance between the four measured functions, $\hat{\gamma}_n(y)$, $\hat{m}^{(n)}(y)$, and the solutions given by Eqs. (7) and (8), i.e.,

$$\min \left\{ \sum_i [\hat{\gamma}_1(y_i) - \gamma_1(y_i)]^2 + [\hat{\gamma}_2(y_i) - \gamma_2(y_i)]^2 + [\hat{m}^{(1)}(y_i) - m^{(1)}(y_i)]^2 + [\hat{m}^{(2)}(y_i) - m^{(2)}(y_i)]^2 \right\}. \quad (10)$$

For an Ornstein-Uhlenbeck process and for pure noise, Eqs. (7) and (8) can even be solved analytically. For the latter case

[i.e., $y(t) = \sigma\zeta(t)$] the moments are given by

$$M^{(1)}(y, \tau) = -y, \quad M^{(2)}(y, \tau) = y^2 + \sigma^2. \quad (11)$$

This means that for pure noise the moments as a function of τ have vanishing slope but nonzero offset, while for an ideal process according to Eq. (1) the situation is reversed. Data from real processes will generally lead to $M^{(n)}$ values with nonzero offsets and nonzero slopes.

Next we consider an *Ornstein-Uhlenbeck process* (given by $D^{(1)} = -\alpha x$ and $D^{(2)} = \beta$) to which measurement noise is added. In this case $p(x)$ is a Gaussian distribution with zero mean and variance $s^2 = \beta/(2\alpha)$. The offsets

$$\gamma_1(y) = -\frac{\sigma^2}{\lambda^2}y, \quad \gamma_2(y) = \sigma^2 + \frac{\sigma^2 s^2}{\lambda^2} + \frac{\sigma^4}{\lambda^4}y^2 \quad (12)$$

and the $m^{(n)}$ values

$$\begin{aligned} m^{(1)}(y, \tau) &= \tau[-\alpha y - \alpha \gamma_1(y)], \\ m^{(2)}(y, \tau) &= \tau(\beta - 2\alpha[\gamma_2(y) - \sigma^2] + y\gamma_1(y)) \end{aligned} \quad (13)$$

can be derived exactly from Eqs. (7) and (8) (see [20] for details). Note that $\lambda^2 := s^2 + \sigma^2$ has been used and that γ_2 approaches $2\sigma^2$ in the small σ limit in accordance with Eq. (6).

From Eq. (13) it is seen that the slopes of the moments, $m^{(n)}/\tau$, are affected by γ_n . Thus simply taking the slope as an estimate of the coefficients—as suggested by Eq. (6)—is not appropriate in the presence of larger measurement noise, even for rather simple cases such as the Ornstein-Uhlenbeck process. Estimates according to Eq. (3) will be increasingly in error as $\gamma_n(y)$ dominates the conditional moments $M^{(n)}(y, \tau)$ for large σ .

For illustration let us consider a numerical realization of an Ornstein-Uhlenbeck process with $\alpha = \beta = 1$. Figure 2(a) shows the pure process ($\sigma = 0$), and Fig. 2(b) shows the process with strong superimposed measurement noise ($\sigma = 1$), corresponding to a negative signal-to-noise ratio of approximately $S/N = 20\log_{10}(s/\sigma) = -3dB$. Without measurement noise the coefficients are directly obtained either from the slopes of the conditional moments or by using Eq. (3) as shown in previous works. The reconstructed drift coefficient of Fig. 2(e) is found to be $\alpha = 1 \pm 0.01$, and analogously $D^{(2)} = \beta = 1 \pm 0.01$ is well reconstructed [see Fig. 2(f)].

In presence of measurement noise the moments $M^{(n)}(y, \tau)$ are still linear functions of τ but, in agreement with Eqs. (7) and (8), exhibit an additional offset term as can be seen in Fig. 2(d). From the measured $M^{(n)}(y, \tau)$ the terms $m^{(n)}(y, \tau)$ and $\gamma_n(y)$ are obtained as follows:

$$\begin{aligned} m^{(1)}/\tau &= -(0.34 \pm 0.02)y, \\ m^{(2)}/\tau &= (0.33 \pm 0.02) + (0.42 \pm 0.01)y^2, \\ \gamma_1 &= (0.667 \pm 0.001)y, \\ \gamma_2 &= (1.33 \pm 0.02) + (0.445 \pm 0.002)y^2. \end{aligned} \quad (14)$$

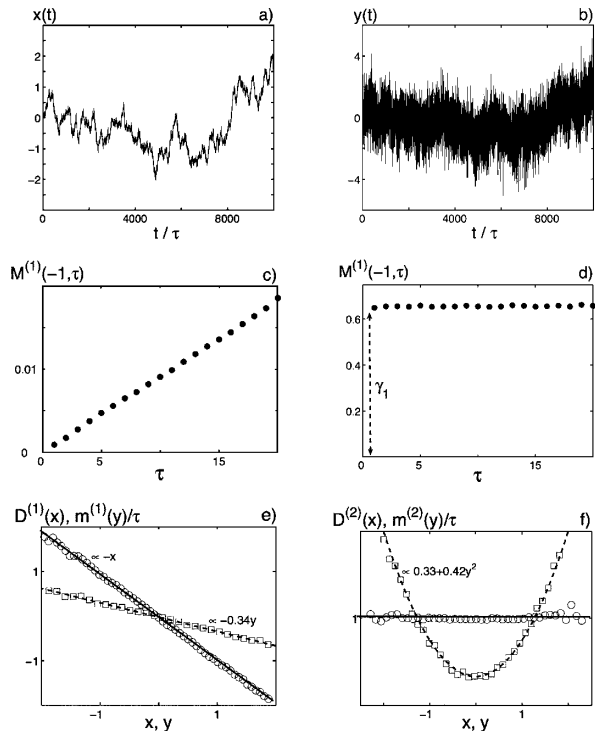


FIG. 2. (a) and (b) show an excerpt of an Ornstein-Uhlenbeck process ($\tau = 10^{-3}$, $\alpha = 1$, and $\beta = 1$) with $\sigma = 0$ in (a) and $\sigma = 1$ in (b). In (c) and (d) the derived $M^{(1)}$ are shown, where (c) refers to $x = -1$ and $\sigma = 0$, and (d) to $y = -1$ and $\sigma = 1$. In (e) and (f) the symbols represent the measured $D^{(n)}$, fitted by the solid lines ($\sigma = 0$), and $m^{(n)}/\tau$, fitted by the dashed lines ($\sigma = 1$), according to Eq. (13).

Using Eq. (12) we obtain the drift coefficient $D^{(1)}(x) = -\alpha x$ with $\alpha = 1.01 \pm 0.02$ in good agreement with the expected value of $\alpha = 1$.

To reconstruct the diffusion term $D^{(2)} = \beta$ the knowledge of $\gamma_1(y)$ and $\gamma_2(y)$ even at a single position y is sufficient when α is known. For instance, for $y = -1$ the measured offsets are $\gamma_1 = 0.65$ and $\gamma_2 = 1.74$, leading to $s = 0.73$ and $\sigma = 0.99$. With $s = \sqrt{\beta/(2\alpha)}$ it follows that $\beta = 1.01 \pm 0.04$. To improve the accuracy of the parameters a least squares algorithm is applied.

Based on the foregoing discussion of an Ornstein-Uhlenbeck process, two important new results can already be given. First, we see that the estimation of the magnitude of measurement noise by the simple approach according to Eqs. (5) and (6) is misleading. For instance, from the offset $\gamma_2(y = 0) = 2\sigma^2 \approx 1.34 \pm 0.02$ a σ^2 value of 0.67, which is about 67% of the real value, would be extracted. This underestimation has already been reported in [8] and can now be understood quantitatively. Second, if the small- τ -estimate $m^{(2)}/\tau$ is taken as an approximation of $D^{(2)}$, as it is commonly done, then an artificial quadratic diffusion term [see Fig. 2(f)] is obtained, masquerading as multiplicative noise or a bad temporal resolution [12].

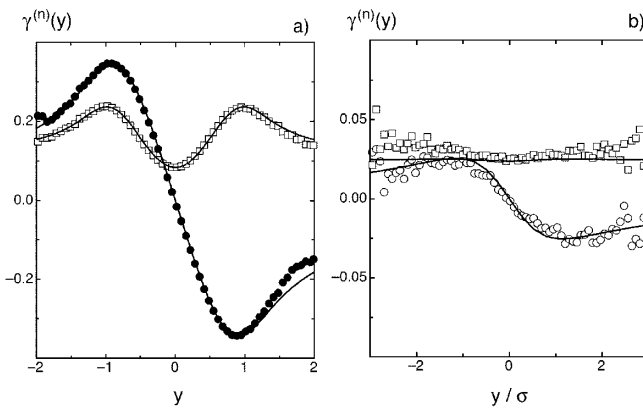


FIG. 3. Symbols represent measured offsets and solid lines the fits according to Eqs. (7) and (8). In both plots circles refer to γ_1 and squares to γ_2 . (a) Iterated multiplicative process with $D^{(1)} = -x$, $D^{(2)} = 0.1 + 0.5x^2$, and $\sigma = 0.25$. (b) Normalized financial increment time series.

Finally, we consider a *general non-Ornstein-Uhlenbeck process* where the coefficients, $D^{(n)}$, are implicitly given only by $m^{(n)}$ and γ_n according to Eqs. (7)–(9). As an example, let us consider a process with multiplicative noise ($D^{(2)} = b + cx^2$) and linear drift ($D^{(1)} = -ax$) which is observed in various systems ranging from finance to turbulence (cf. [15,21,22]). Here we take $a = 1$, $b = 0.1$, and $c = 0.5$ and iterate numerically. The measurement noise amplitude is $\sigma = 0.25$, which corresponds to a signal-to-noise ratio of $S/N = 0$. Figure 3(a) shows the observed offsets, γ_n , together with the (numerical) solutions according to Eqs. (7) and (8) for the iterated multiplicative process. Figure 3(b) refers to the financial increment time series for which the reconstructed coefficients are found to be $D^{(1)}(x) = -0.0012x$ and $D^{(2)}(x) = 0.0014 + 0.001x^2$ and the measurement noise amplitude is $\sigma = 0.11$. This result shows that multiplicative dynamical noise causes intermittent heavy-tailed volatility statistics in financial data as was proposed, and this is not due to a spurious effect of measurement noise, as for the case of Fig. 2(f)].

From the examples of Fig. 3 we see again that the understanding of the influence of measurement noise on the conditional moments, i.e., on γ_n and $m^{(n)}/\tau$, is the key to achieving a proper reconstruction of the underlying dynamical process (including the contribution of dynamical noise and measurement noise) from pure data analysis. Naively applying the definition according to Eq. (3) will no longer be appropriate as soon as measurement noise is present.

To conclude, we have shown (for numerical as well as real world data) that adding measurement noise to signals generated from a Langevin process leads to a fundamental modification of the data analysis via the conditional moments. A general equation describing this modification has been presented and for the class of Ornstein-Uhlenbeck

processes analytical results are given. This makes it possible to extract the strength of measurement noise, σ , the standard deviation of the underlying process, s , as well as the drift and diffusion coefficients, $D^{(1)}$ and $D^{(2)}$, rather precisely even in presence of very strong measurement noise. It is noteworthy that the evaluation of the process' coefficients is solely based on analyzing the conditional moments, which are directly obtained from the time series without any need of premanipulating (e.g., filtering, modeling) the data.

We wish to acknowledge stimulating discussions with M. Siefert, St. Barth, M. Hölling, A. Nawroth, and S.G. Bradley.

*Electronic address: frank.boettcher@uni-oldenburg.de

†Electronic address: peinke@uni-oldenburg.de

- [1] H. Kantz and T. Schreiber, *Nonlinear Time Series Analysis* (Cambridge University Press, Cambridge, England, 1997).
- [2] R. Friedrich and J. Peinke, Phys. Rev. Lett. **78**, 863 (1997).
- [3] S. Siegert, R. Friedrich, and J. Peinke, Phys. Lett. A **243**, 275 (1998).
- [4] G. Ryskin, Phys. Rev. E **56**, 5123 (1997).
- [5] R. Friedrich *et al.*, Phys. Lett. A **271**, 217 (2000).
- [6] J. Gradišek, S. Siegert, R. Friedrich, and I. Grabec, Phys. Rev. E **62**, 3146 (2000).
- [7] S. Kriso, J. Peinke, R. Friedrich, and P. Wagner, Phys. Lett. A **299**, 287 (2002).
- [8] M. Siefert, A. Kittel, R. Friedrich, and J. Peinke, Europhys. Lett. **61**, 466 (2003).
- [9] M. Siefert and J. Peinke, Int. J. Bifurcation Chaos Appl. Sci. Eng. **14**, 2005 (2004).
- [10] T. Kuusela, Phys. Rev. E **69**, 031916 (2004).
- [11] M. Ragwitz and H. Kantz, Phys. Rev. Lett. **87**, 254501 (2001).
- [12] P. Sura and J. Barsugli, Phys. Lett. A **305**, 304 (2002).
- [13] R. Friedrich, C. Renner, M. Siefert, and J. Peinke, Phys. Rev. Lett. **89**, 149401 (2002).
- [14] P. E. Kloeden and E. Platen, *Numerical Solution of Stochastic Differential Equations* (Springer, New York, 1999).
- [15] C. Renner, J. Peinke, and R. Friedrich, J. Fluid Mech. **433**, 383 (2001).
- [16] J. P. M. Heald and J. Stark, Phys. Rev. Lett. **84**, 2366 (2000).
- [17] E. J. Kostelich and T. Schreiber, Phys. Rev. E **48**, 1752 (1993).
- [18] C. Renner, J. Peinke, and R. Friedrich, Physica (Amsterdam) **298A**, 499 (2001).
- [19] H. Risken, *The Fokker-Planck Equation* (Springer, New York, 1989).
- [20] F. Böttcher, Ph.D. thesis, Oldenburg, 2005.
- [21] M. Waechter, F. Riess, T. Schimmel, U. Wendt, and J. Peinke, Eur. Phys. J. B **41**, 259 (2004).
- [22] M. Tutkun and L. Mydlarski, New J. Phys. **6**, 49 (2004).
- [23] P. G. Lind, A. Mora, J. A. C. Gallas, and M. Haase, Int. J. Bifurcation Chaos Appl. Sci. Eng. (to be published).

Estimation of Kramers-Moyal coefficients at low sampling rates

Christoph Honisch* and Rudolf Friedrich

Institute for Theoretical Physics, University of Muenster, D-48149 Muenster, Germany

(Dated: October 11, 2018)

A new optimization procedure for the estimation of Kramers-Moyal coefficients from stationary, one-dimensional, Markovian time series data is presented. The method takes advantage of a recently reported approach that allows to calculate exact finite sampling interval effects by solving the adjoint Fokker-Planck equation. Therefore it is well suited for the analysis of sparsely sampled time series. The optimization can be performed either making a parametric ansatz for drift and diffusion functions or also parameter free. We demonstrate the power of the method in several numerical examples with synthetic time series.

PACS numbers: 05.10.Gg, 05.45.Tp, 05.45.Xt

I. INTRODUCTION

The behavior of complex systems consisting of a large number of degrees of freedom can often be described by low dimensional macroscopic order parameter equations [1]. Thereby the influence of the microscopic degrees of freedom is treated via noise terms of Langevin type [2]. In case of a single order parameter $q(t)$ its time evolution can be described by

$$\dot{q} = h(q, t) + g(q, t)\Gamma(t) \quad (1)$$

where $\Gamma(t)$ is a Gaussian distributed white noise term satisfying $\langle \Gamma(t) \rangle = 0$ and $\langle \Gamma(t)\Gamma(t') \rangle = \delta(t-t')$. Here and in the following Ito's interpretation of stochastic integrals is used [2].

The same information is contained in the corresponding Fokker-Planck equation (FPE) for the probability density function of $f_q(x, t)$

$$\frac{\partial f_q(x, t)}{\partial t} = \hat{L}(x, t)f_q(x, t). \quad (2)$$

Here we have introduced the Fokker-Planck operator

$$\hat{L}(x, t) = -\frac{\partial}{\partial x}D^{(1)}(x, t) + \frac{\partial^2}{\partial x^2}D^{(2)}(x, t) \quad (3)$$

which contains the Kramers-Moyal (KM) coefficients

$$D^{(n)}(x, t) = \lim_{\tau \rightarrow 0} \frac{1}{n! \tau} \langle [q(t+\tau) - q(t)]^n \rangle|_{q(t)=x} \quad (4)$$

also referred to as drift and diffusion for $n = 1$ and $n = 2$, respectively. The connection to the functions g and h in Eq. (1) is $h(x, t) = D^{(1)}(x, t)$ and $g(x, t) = \sqrt{2}D^{(2)}(x, t)$.

As was recently shown [3, 4], it is possible to set up an equation of the form (1) by estimating the conditional averages in (4) from a data set of the variable $q(t)$. This method was applied in various fields of science, see Ref. [5] for an overview.

There are two major problems connected to the estimation of drift and diffusion coefficients from measured “real world” time series. The first problem consists in the occurrence of measurement noise. In Ref. [6] it was shown that measurement noise spoils the Markov property, the latter being a requirement for the KM analysis. A promising approach to handle Gaussian distributed exponentially correlated measurement noise was recently proposed by Lehle [7].

The other problem in the Kramers-Moyal analysis is that one has to perform the limit $\tau \rightarrow 0$, while data sets are recorded at finite sampling intervals. Also in real world processes the intrinsic noise is not strictly δ -correlated, which results in a finite Markov-Einstein time, i. e., a finite time interval τ_{ME} such that for time intervals $\tau < \tau_{ME}$ the Markov property does no longer hold. It is observed that in case of a finite Markov-Einstein time, the KM coefficients go to zero with decreasing time interval τ .

Ragwitz and Kantz [8] were the first who presented a formula to estimate the KM coefficients that takes into account finite sampling interval effects at first order in the sampling interval. In a comment on this article Friedrich *et al.* [9] presented correction terms in form of an infinite series expansion in the sampling interval. Very recently Antenedo *et al.* presented exact analytical expressions for the finite time KM coefficients (s. Eq. (5)) for processes with linear drift and quadratic diffusion [10] and later for other common processes [11].

A very elegant way to obtain finite time KM coefficients for arbitrary (but sufficiently smooth) drift and diffusion terms was recently presented by Lade [12]. He reinterpreted the series expansion presented in [9] in a way that finite time coefficients can be obtained by solving the adjoint Fokker-Planck equation. Since this can be done at least numerically, Lades method opens up the possibility to deduce the true KM coefficients from measured finite time coefficients by an optimization approach. This is the topic of the present work.

Of course, finite time KM coefficients can also be obtained by simulating Langevin equations and measuring the conditional moments at a finite τ . This was done in the iterative method developed by Kleinhans *et al.*

*Electronic address: c.honisch@uni-muenster.de

[13, 14]. But since this is numerically very demanding, the method was only applied to situations where very few parameters had to be optimized. In this article we show that an optimization based on Lades method can even be performed without a parametric ansatz for drift and diffusion coefficients, which should make it more applicable for a larger class of diffusion processes.

In the next section we review the method of Lade [12] that allows for a calculation of exact finite time effects. The following section gives a description of our new optimization procedure. Section IV contains four numerical examples in which the functionality of our method is demonstrated.

II. EXACT FINITE SAMPLING INTERVAL EFFECTS

From now on we assume the Langevin process of interest to be stationary, i.e., drift and diffusion do not explicitly depend on time. We define the *finite time coefficients* as

$$D_{\tau}^{(n)}(x) = \frac{1}{n! \tau} M_{\tau}^{(n)}(x) \quad (5)$$

with the conditional moments

$$M_{\tau}^{(n)}(x) = \int_{-\infty}^{\infty} (x' - x)^n p(x', t + \tau | x, t) dx'. \quad (6)$$

The conditional probability density function $p(x', t + \tau | x, t)$ is the solution of the corresponding FPE with the initial condition $\delta(x' - x)$, so it can be expressed as

$$p(x', t + \tau | x, t) = e^{\hat{L}(x')\tau} \delta(x' - x). \quad (7)$$

Inserting this in (6) results in

$$\begin{aligned} M_{\tau}^{(n)}(x) &= \langle (x' - x)^n | e^{\hat{L}(x')\tau} | \delta(x' - x) \rangle \\ &= \langle e^{\hat{L}^\dagger(x')\tau} (x' - x)^n | \delta(x' - x) \rangle \\ &= e^{\hat{L}^\dagger(x')\tau} (x' - x)^n \Big|_{x'=x}, \end{aligned} \quad (8)$$

where we use the notation $\langle f | g \rangle = \int_{-\infty}^{\infty} f(x') g(x') dx'$ for the inner product. \hat{L}^\dagger is the adjoint Fokker-Planck operator

$$\hat{L}^\dagger(x') = D^{(1)}(x') \frac{\partial}{\partial x'} + D^{(2)}(x') \frac{\partial^2}{\partial x'^2}. \quad (9)$$

The main point of Lade's article [12] is to interpret eq. (8) as the solution to the partial differential equation

$$\left| \begin{array}{l} \frac{\partial W_{n,x}(x', t)}{\partial t} = \hat{L}^\dagger(x') W_{n,x}(x', t) \\ W_{n,x}(x', 0) = (x' - x)^n \end{array} \right. \quad (10)$$

at $t = \tau$, $x = x_0$, i.e.:

$$M_{\tau}^{(n)}(x) = W_{n,x}(x, \tau). \quad (11)$$

For simple drift and diffusion coefficients, eq. (10) can be solved analytically. E.g., for an Ornstein-Uhlenbeck process [2] with $D^{(1)}(x) = -\gamma x$ and $D^{(2)}(x) = D$, one obtains [12]

$$W_{1,x}(x', t) = x' e^{-\gamma t} - x \quad (12)$$

$$W_{2,x}(x', t) = (x' e^{-\gamma t} - x)^2 + \frac{D}{\gamma} (1 - e^{-2\gamma t}). \quad (13)$$

With Eq. (5) and (11) we get

$$D_{\tau}^{(1)}(x) = -\frac{x}{\tau} (1 - e^{-\gamma\tau}) \quad (14)$$

$$D_{\tau}^{(2)}(x) = \frac{1}{2\tau} \left[x^2 (1 - e^{-\gamma\tau})^2 + \frac{D}{\gamma} (1 - e^{-2\gamma\tau}) \right]. \quad (15)$$

A process with linear drift $D^{(1)}(x) = -\gamma x$ and quadratic diffusion $D^{(2)}(x) = \alpha + \beta x^2$ gives the same finite time drift as for the Ornstein-Uhlenbeck process. For the diffusion we obtain

$$\begin{aligned} W_{2,x}(x', t) &= x^2 - \frac{\alpha}{\beta - \gamma} \left(1 - e^{2(\beta - \gamma)t} \right) \\ &\quad + x'^2 e^{2(\beta - \gamma)t} - 2x x' e^{-\gamma t}, \end{aligned} \quad (16)$$

which leads to

$$\begin{aligned} D_{\tau}^{(2)}(x) &= \frac{1}{2\tau} \left[x^2 \left(1 + e^{2(\beta - \gamma)\tau} - 2e^{-\gamma\tau} \right) \right. \\ &\quad \left. - \frac{\alpha}{\beta - \gamma} \left(1 - e^{2(\beta - \gamma)\tau} \right) \right]. \end{aligned} \quad (17)$$

If an analytical solution cannot be obtained one has to solve eq. (10) numerically up to $t = \tau$ for all x values of interest.

An alternative way to calculate finite time effects would be to solve the real FPE, instead of the adjoint FPE, which yields the whole transition pdf. But this would involve a Dirac δ -function as an initial condition which is expected to cause numerical problems. The adjoint FPE can be easily solved via a simple forward-time centered-space scheme. For the spatial derivatives on the left and right boundaries we use second order forward and backward finite differences, respectively.

III. THE OPTIMIZATION PROCEDURE

The first step of the optimization is to estimate the conditional moments (6) for a set of τ values $\{\tau_1, \dots, \tau_M\}$, $\tau_i < \tau_{i+1}$, and a set of x values $\{x_1, \dots, x_N\}$, $x_i < x_{i+1}$. The latter should be the same values that are later on used for the numerical integration of the adjoint FPE. In a histogram based regression the size of the bins located at x_i is limited through the available amount of data. Therefore a kernel based regression as described in [15] is favorable which results in a smooth curve. We denote the estimated conditional moments by $\hat{M}_{\tau_i}^{(1,2)}(x_j)$. It is also important to calculate statistical errors $\hat{\sigma}_{ij}^{(1,2)}$.

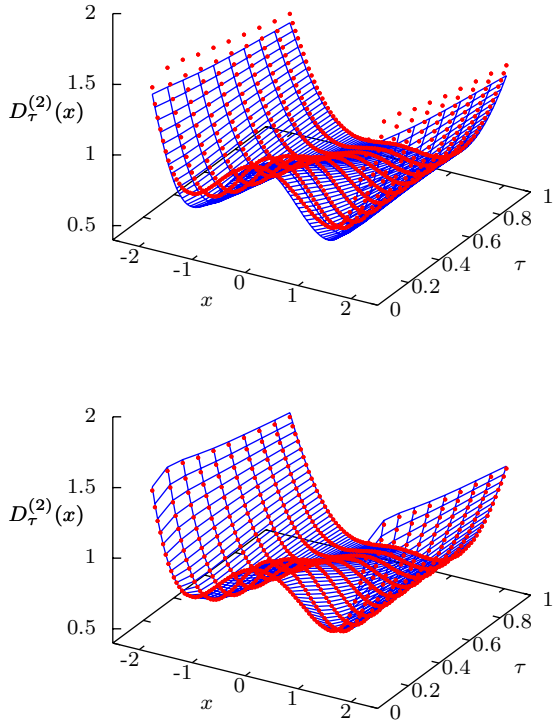


FIG. 1: (Color online) Illustration of the optimization procedure. The red dots in both graphs show the estimated finite time coefficients $\hat{D}_\tau^{(2)}(x) = \hat{M}_\tau^{(2)}(x)/(2\tau)$ for the example of Sec. IV C. The blue surface in the top panel corresponds to $D_\tau^{(2)}(x, \sigma_{\text{ini}})$. By minimizing $V(\sigma)$ we seek a set of parameters σ such that $D_\tau^{(1,2)}(x, \sigma)$ conforms to $\hat{D}_\tau^{(1,2)}(x)$, respectively, as is the case for the diffusion in the lower panel.

The optimization can be performed with or without the use of parameterized drift and diffusion functions. In the former case one has to embed the drift and diffusion functions into a family of functions $D^{(1)}(x, \sigma)$ and $D^{(2)}(x, \sigma)$, respectively, with a set of parameters denoted by σ .

In the latter case one has to define a set of sampling points $\{x_1^s, \dots, x_K^s\}$, $K < N$, and represent $D^{(1)}$ and $D^{(2)}$ as a spline interpolation through these sampling points. Then the set of parameters to be optimized is $\sigma = \{D^{(1)}(x_1^s), \dots, D^{(1)}(x_K^s), D^{(2)}(x_1^s), \dots, D^{(2)}(x_K^s)\}$. In both cases $D_{\tau_1}^{(1)}$ and $D_{\tau_1}^{(2)}$ can be used to construct an initial guess σ_{ini} .

For a specific set of parameters σ , the conditional moments (6) can be calculated as described in sec. II, yielding $M_{\tau_i}^{(1,2)}(x_j, \sigma)$. Since these computations are to be performed for each x_j individually, it is very easy and efficient to parallelize this part for the use on parallel computers.

The final step is to find the minimum of the least

square potential

$$V(\sigma) = \sum_{i=1}^M \sum_{j=1}^N \left[\frac{\left\{ \hat{M}_{\tau_i}^{(1)}(x_j) - M_{\tau_i}^{(1)}(x_j, \sigma) \right\}^2}{\left(\hat{\sigma}_{ij}^{(1)} \right)^2} + \frac{\left\{ \hat{M}_{\tau_i}^{(2)}(x_j) - M_{\tau_i}^{(2)}(x_j, \sigma) \right\}^2}{\left(\hat{\sigma}_{ij}^{(2)} \right)^2} \right]. \quad (18)$$

Fig. 1 illustrates the idea of this procedure.

For the optimization we use a trust region algorithm [16]. It turns out that for large sampling intervals τ_1 , the best results are achieved, when only that single τ_1 is used, i.e. $M = 1$ in Eq. (18). For smaller sampling intervals the accuracy can be improved by the use of more τ values.

After the optimization procedure has converged to a certain set of parameters σ_{res} , one can perform a self-consistency check by comparing graphically the functions $D_\tau^{(1,2)}(x, \sigma_{\text{res}})$ and $\hat{D}_\tau^{(1,2)}(x)$ as in Fig. 1.

IV. NUMERICAL EXAMPLES

A. Ornstein-Uhlenbeck process

As a first numerical example we consider an Ornstein-Uhlenbeck process with $D^{(1)}(x) = -x$ and $D^{(2)}(x) = 1$. A synthetic time series with 10^7 data points is computed using a forward Euler scheme with a time step $\Delta t = 10^{-3}$, but only every 1000th time step is stored. So the minimal time increment, that is available for the data analysis, is $\tau_1 = 1$. The symbols with the error bars in Fig. 2 show the estimated finite time coefficients $D_{\tau_1}^{(1)}(x)$ (top) and $D_{\tau_1}^{(2)}(x)$ (bottom). From this it seems reasonable to make the parametric ansatz $D^{(1)}(x) = -ax$ and $D^{(2)}(x) = b + cx^2$. As an initial guess, we choose $a_{\text{ini}} = 0.63$, $b_{\text{ini}} = 0.43$ and $c_{\text{ini}} = 0.2$. The corresponding curves are shown in blue in Fig. 2. The resulting parameters from the optimization are $a_{\text{res}} = 0.9966$, $b_{\text{res}} = 0.9995$ and $c_{\text{res}} = 0.00032$. These values correspond to the red curves in Fig. 2. For comparison we also plot the black dots which correspond to the true parameters $a = 1$, $b = 1$ and $c = 0$.

B. Multiplicative noise

The next example is a system with multiplicative noise, i.e., the diffusion term depends on x . We choose $D^{(1)}(x) = -x$ and $D^{(2)}(x) = 1 + x^2$. In the same manner as in the previous example, we construct a time series with 10^8 data points and a sampling interval $\tau_1 = 1$. From the estimated finite time coefficients for $D_{\tau_1}^{(1,2)}$ we again deduce the parametric ansatz $D^{(1)}(x) = -ax$ and $D^{(2)}(x) = b + cx^2$ and take as an initial guess $a_{\text{ini}} = 0.63$,

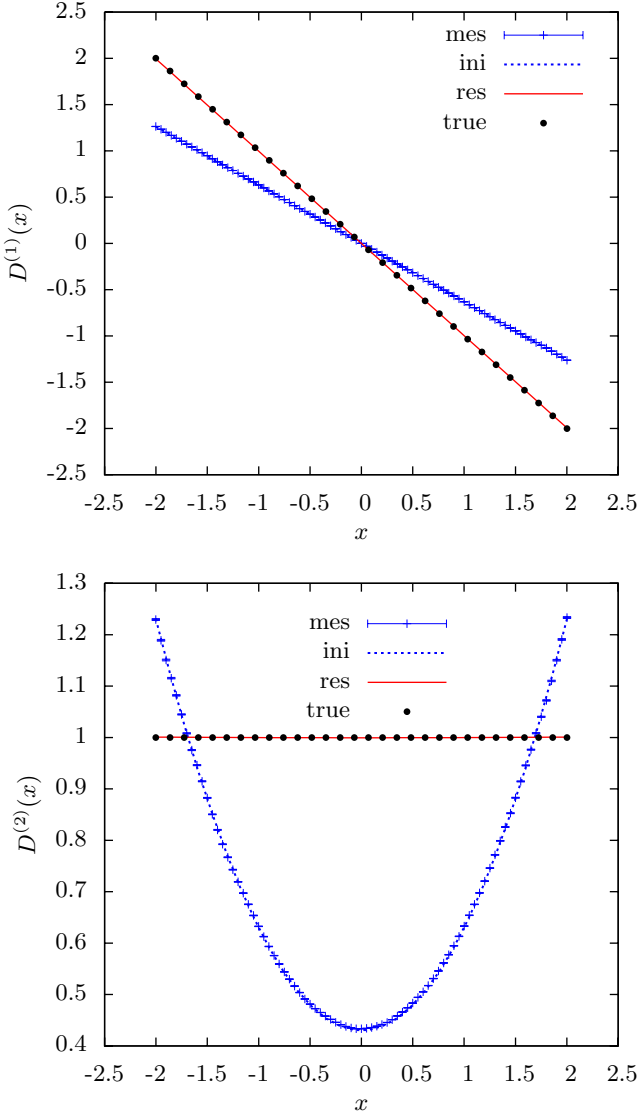


FIG. 2: (Color online) Results for an Ornstein-Uhlenbeck process with $D^{(1)}(x) = -x$, $D^{(2)}(x) = 1$. The analyzed time series consists of 10^7 data points with a sampling interval $\tau_1 = 1$. The blue crosses with error bars are the estimated finite time coefficients $D_{\tau_1}^{(1)}$ (top) and $D_{\tau_1}^{(2)}$ (bottom). The blue dotted curves show the initial guesses for the optimization, the red solid ones show the result. For comparison also the true coefficients are plotted (black dots).

$b_{\text{ini}} = 1.0$ and $c_{\text{ini}} = 0.7$. The finite time coefficients as well as the initial condition are depicted in blue in Fig. (3). From the optimization we obtain the parameters $a_{\text{res}} = 0.9989$, $b_{\text{res}} = 1.004$ and $c_{\text{res}} = 0.9963$. The corresponding curves are shown in red in Fig. (3) as well as the true coefficients with $a = b = c = 1$ (black dots).

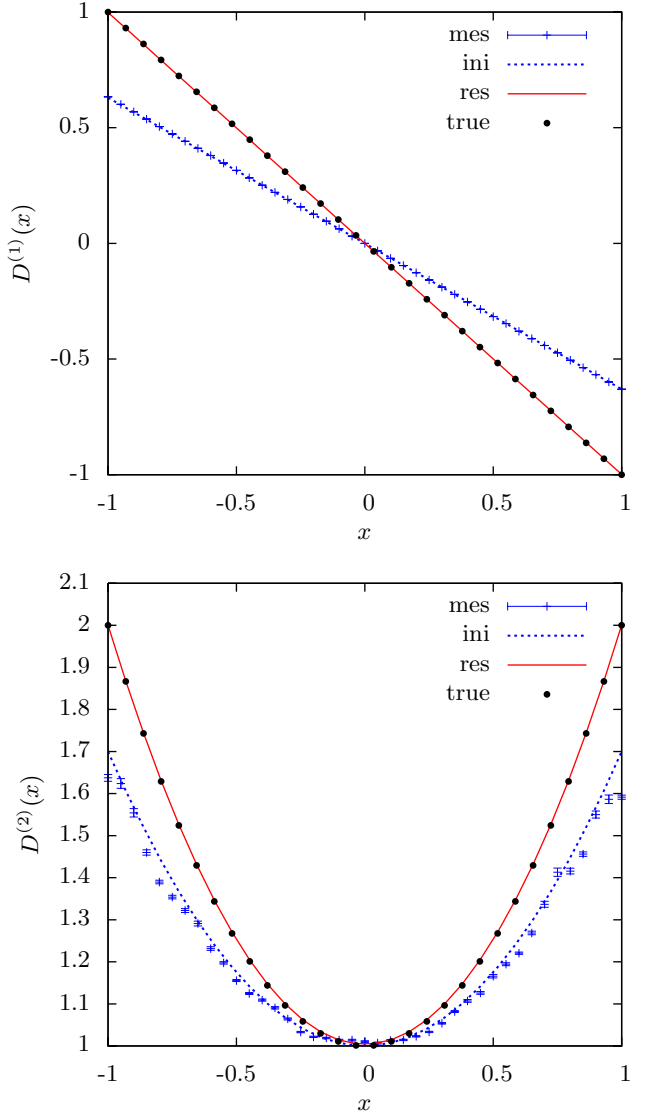


FIG. 3: (Color online) System with multiplicative noise: $D^{(1)}(x) = -x$, $D^{(2)}(x) = 1 + x^2$. The analyzed time series consists of 10^8 data points with a sampling interval $\tau_1 = 1$. The representation is analog to Fig. 2.

C. Bistable system

The first example for a parameter free optimization is a bistable system with $D^{(1)}(x) = x - x^3$ and $D^{(2)}(x) = 1$. The blue dots in Fig. (4) correspond to the finite time coefficients $D_{\tau_1}^{(1,2)}$. They are used as the initial guess for the parameters σ to be optimized. The terms $M_{\tau_i}^{(1,2)}(x_j, \sigma)$ in Eq. (18) are now calculated by a spline interpolation between these sampling points. They are shown in blue in Fig. (4). The resulting parameters that minimize (18) are the red squares from which the red spline curves are calculated. The latter represent the resulting drift and diffusion coefficients.

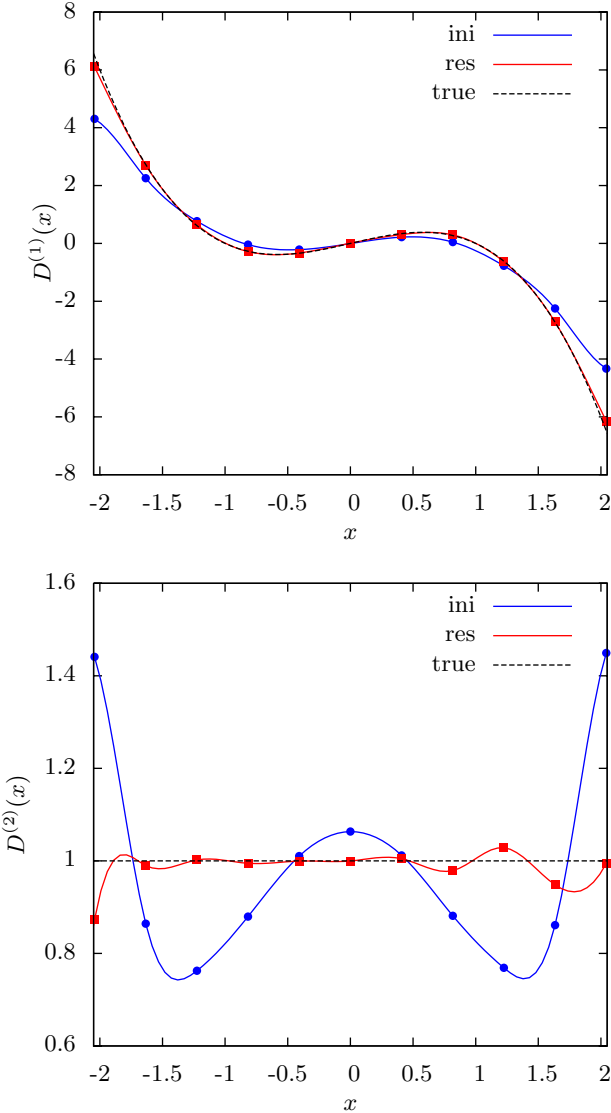


FIG. 4: (Color online) Bistable system with $D^{(1)}(x) = x - x^3$, $D^{(2)}(x) = 1$. The analyzed time series consists of 10^7 data points with a sampling interval $\tau_1 = 0.1$. The blue and red symbols are sampling points, from which the corresponding curves are computed as spline interpolations, and serve as optimization parameters. The blue dots represent the initial condition derived from the finite time coefficients $D_{\tau_1}^{(1,2)}$. The red squares show the result of the optimization. The black dashed curves show the true coefficients for comparison.

D. Phase dynamics

As a last example, we consider a phase variable ϕ that can also be a phase difference $\phi = \phi_1 - \phi_2$ between two coupled nonlinear oscillators. The reconstruction of phase dynamics from data sets is an important theoretical problem that is relevant in many different fields of science. The problem was among others tackled by Kralemann *et al.* [17]. We suggest the KM approach as a less

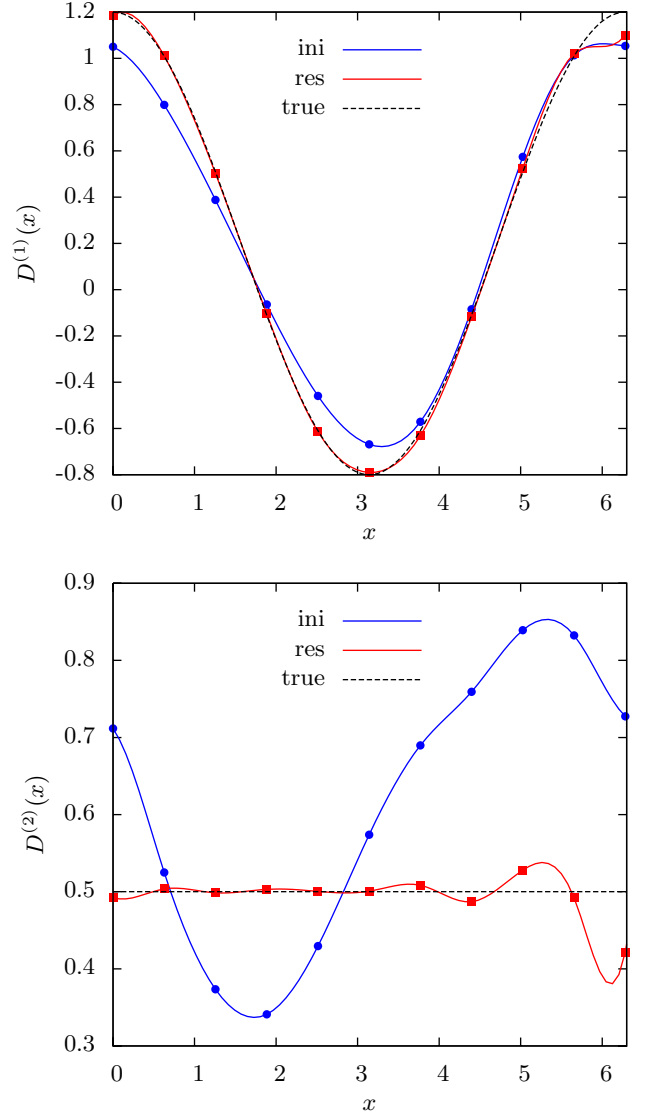


FIG. 5: (Color online) Phase dynamics with $D^{(1)}(x) = 0.2 + \cos(x)$, $D^{(2)}(x) = 0.5$. The analyzed time series consists of 10^7 data points with a sampling interval $\tau_1 = 1$. The representation is analog to Fig. 4

cumbersome alternative.

In the case of phase dynamics, the drift and diffusion coefficients must be 2π -periodic, i.e., $D^{(n)}(x) = D^{(n)}(x + 2\pi)$. Therefore, it makes sense to define the KM coefficients as

$$D^{(n)}(x, t) = \lim_{\tau \rightarrow 0} \frac{1}{n! \tau} \langle [\phi(t + \tau) - \phi(t)]^n \rangle|_{\phi(t) \bmod 2\pi = x}. \quad (19)$$

Phase dynamics are often governed by Langevin equations of the form

$$\dot{\phi} = \omega + \cos(\phi) + \sqrt{2D} \Gamma. \quad (20)$$

We consider the case $\omega = 0.2$; $D = 0.5$, so we have

$D^{(1)}(x) = 0.2 + \cos(x)$ and $D^{(2)}(x) = 0.5$. Fig. 5 shows the result in the same representation as in Fig. 4.

V. SUMMARY AND OUTLOOK

We have presented a novel optimization procedure for the estimation of drift and diffusion coefficients for one-dimensional Markovian time series that suffer from large

sampling intervals. The optimization can be performed both in a parametric and non-parametric fashion. Therefore, it is applicable for a large class of diffusion processes. The usefulness of our method is demonstrated in four examples with synthetic time series. The method yields good results, even if the sampling interval is of the order of the typical time scales of the deterministic part of the dynamics.

-
- [1] H. Haken, *Synergetics*, Springer Series in Synergetics (Springer-Verlag, 1978).
 - [2] H. Risken, *The Fokker-Planck Equation* (Springer-Verlag, 1984).
 - [3] S. Siegert, R. Friedrich, and J. Peinke, Phys. Lett. A **243**, 275 (1998).
 - [4] R. Friedrich, S. Siegert, J. Peinke, S. Lück, M. Siefert, M. Lindemann, J. Raethjen, G. Deuschl, and G. Pfister, Phys. Lett. A **271**, 217 (2000).
 - [5] R. Friedrich, J. Peinke, and M. R. R. Tabar, in *Encyclopedia of Complexity and Systems Science*, edited by R. A. Meyers (Springer-Verlag, 2009), pp. 3574 – 3597.
 - [6] D. Kleinhans, R. Friedrich, M. Wächter, and J. Peinke, Phys. Rev. E **76**, 041109 (2007).
 - [7] B. Lehle, Analysis of stochastic time series in the presence of strong measurement noise, Phys. Rev. E, accepted.
 - [8] M. Ragwitz and H. Kantz, Phys. Rev. Lett. **87**, 254501 (2001).
 - [9] R. Friedrich, C. Renner, M. Siefert, and J. Peinke, Phys. Rev. Lett. **89**, 149401 (2002).
 - [10] C. Anteneodo and R. Riera, Phys. Rev. E **80**, 031103 (2009).
 - [11] C. Anteneodo and S. M. D. Queirós, Phys. Rev. E **82**, 041122 (2010).
 - [12] S. J. Lade, Phys. Lett. A **373**, 3705 (2009).
 - [13] D. Kleinhans, R. Friedrich, A. Nawroth, and J. Peinke, Physics Letters A **346**, 42 (2005).
 - [14] D. Kleinhans and R. Friedrich, Physics Letters A **368**, 194 (2007), ISSN 0375-9601.
 - [15] D. Lamouroux and K. Lehnertz, Phys. Lett. A **373**, 3507 (2009).
 - [16] Y.-X. Yuan, in *ICIAM 99: Proceedings of the Fourth International Congress on Industrial & Applied Mathematics* (2000).
 - [17] B. Kralemann, L. Cimponeriu, M. Rosenblum, A. Pikovsky, and R. Mrowka, Phys. Rev. E **77**, 066205 (2008).

Physics of brain dynamics: Fokker–Planck analysis reveals changes in EEG δ – θ interactions in anaesthesia

A Bahraminasab¹, F Ghasemi², A Stefanovska^{1,3},
P V E McClintock¹ and R Friedrich²

¹ Department of Physics, Lancaster University, Lancaster LA1 4YB, UK

² Institute of Theoretical Physics, Westfälische Wilhelms-Universität
Wilhelm-Klemm-Strasse 9, 48149 Münster, Germany

E-mail: aneta@lancaster.ac.uk

New Journal of Physics **11** (2009) 103051 (12pp)

Received 3 June 2009

Published 27 October 2009

Online at <http://www.njp.org/>

doi:10.1088/1367-2630/11/10/103051

Abstract. We use drift and diffusion coefficients to reveal interactions between different oscillatory processes underlying a complex signal and apply the method to EEG δ and θ frequencies in the brain. By analysis of data recorded from rats during anaesthesia, we consider the stability and basins of attraction of fixed points in the phase portrait of the deterministic part of the retrieved stochastic process. We show that different classes of dynamics are associated with deep and light anaesthesia, and we demonstrate that the predominant directionality of the interaction is such that θ drives δ .

³ Author to whom any correspondence should be addressed.

Contents

| | |
|---|-----------|
| 1. Introduction | 2 |
| 2. Experimental methods and data acquisition | 3 |
| 3. Fokker–Planck analysis | 4 |
| 4. Application to δ and θ brain waves in anaesthesia | 6 |
| 4.1. Stationary solution for retrieved drift and diffusion coefficients | 6 |
| 4.2. Dynamics and fixed points (FPs) | 8 |
| 5. Tests of the validity of the results | 10 |
| 6. Concluding remarks | 10 |
| Acknowledgments | 11 |
| References | 11 |

1. Introduction

Complex signals typically contain a great deal of information about the underlying processes that generate them, but the extraction of such information can be difficult and requires methods drawn from physics and nonlinear science [1]–[4]. This is especially true of signals derived from living systems. Their complexity arises in part from nonlinear interactions between subsystems oscillating on widely differing timescales, and in part from the confusing influence of seemingly random fluctuations. Electroencephalographic (EEG) recordings of brain activity [1] exemplify the problem. It has long been appreciated [5] that they exhibit continuous widespread oscillations, but their origin remains barely understood. As in the case of cardiovascular signals [6], there are multiple rhythms enclosed within broad-band noise. In dynamical terms, these oscillations might be attributed to limit-cycle attractors, because analyses of short segments often reveal spectral peaks in particular frequency ranges. Interactions between the processes generating some of these EEG waves have been demonstrated [7] but not yet explored much.

Understanding the interdependences between complex dynamical systems is of quite general scientific importance, e.g. in physics, chemistry, biology and neuroscience; it can also be of importance for, e.g. economics and sociology. Often, the underlying equations of motion are unknown, but a detailed quantitative description of interdependences can nonetheless be achieved by time-series analysis of experimentally measured observables. In recent years, a number of methods have been developed that allow one to detect and to quantify the strengths of the possible interactions [8]. Asymmetric approaches have facilitated the detection of directional coupling from time series. At some risk of over-simplification they can conveniently be divided into three main groups: techniques based on interrelationships between parameters of oscillatory dynamics and, in particular, phase dynamics [9]–[11]; state-space-based methods [12, 13] and information-theoretic approaches [14, 15].

State-space-based approaches provide strong methods for detecting generalized synchronization or directionality patterns between two coupled systems. Also, the fact that there are not many free parameters involved in driving the state-space patterns makes such measures relatively easy to implement, and robust. Their main challenges are in finding well-defined quantitative measures of directionality or driver-response and in that it is often difficult to localize the reconstructed properties in time. Generally, all three groups of methods tend

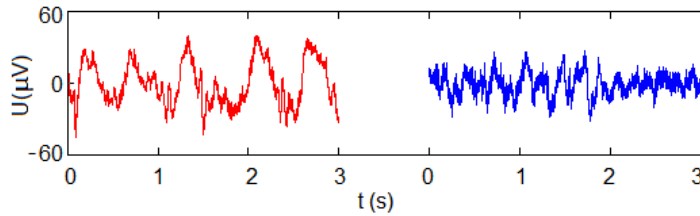


Figure 1. Short (3 s) segments of EEG signal for deep (left) compared with light (right) anaesthesia.

to make rather strict assumptions about the dynamics of the systems that generate the time series, e.g. that they should be linear systems, or in the case of self-sustained oscillators that they should be weakly-coupled. Furthermore, many of the approaches focus preferentially on the low-dimensional deterministic part of the dynamics. In reality, however, the influences of noise on nonlinear dynamical systems can be far from trivial [16]–[18] and they constitute a subject of continuing interest and importance. Real signals frequently result from dissipative dynamical systems under the influence of noise, and it is often useful to describe them in terms of Fokker–Planck formalism [19].

In this paper, we combine the multidimensional Fokker–Planck equation [16, 20] with mathematical modelling of the system dynamics, enabling us to extract model parameters directly from the measured time series [2, 3, 20]. We concentrate on the interactions between EEG θ waves and δ waves in anaesthesia, and characterize some of their properties. Following [20, 21] we apply a two-dimensional (2D) Markov analysis to EEG signals recorded [22] from rats during deep and light anaesthesia (see examples in figure 1); and we carry out a stability analysis of the deterministic part of the derived equations. We find in these experiments that the dynamics falls into different universality classes for the states of deep and light anaesthesia, enabling us to distinguish robustly between them. Although we treat brain dynamics explicitly, the method is applicable to complex systems quite generally.

In section 2, we describe succinctly how our experimental data were acquired from rats and pre-processed prior to analysis. Section 3 describes the basic method used for the analysis, and section 4 discusses how we applied it to the rat EEG signals and considers the results that emerge. Section 5 describes some simple tests undertaken to eliminate artifacts and to check the validity of the results. Finally, in section 6, we summarize and consider the main results, and draw conclusions.

2. Experimental methods and data acquisition

A full description of how the signals were measured has already been given elsewhere [22], so here we just summarize the salient features. The experiments were performed on 10 adults, male Wistar rats weighing 250–300 g. The animals were each anaesthetized with a single intraperitoneal injection of ketamine hydrochloride ($45 \text{ mg} (\text{kg body wt})^{-1}$) and xylazine hydrochloride ($7 \text{ mg} (\text{kg body wt})^{-1}$). (Measurements were also carried out on a second group of rats anaesthetized with pentobarbital [22] but these are not discussed here.) As soon as the rat could no longer hold its upright posture, 10–15 min after administration of the drug, it was placed in a darkened Faraday cage where sensors were mounted and recording

started immediately. The EEG was recorded over the left and right parietal cortex with three hypodermic needles inserted under the animal's scalp to serve as electrodes. The EEG was differentially amplified by $10^3 \times$ and low-pass filtered with a cut-off frequency of 300 Hz. The resultant signal was fed through a signal conditioning system, digitized at 1 kHz with 16-bit resolution, and stored on the hard disk of a laptop computer.

Depth of anaesthesia was assessed at 5 min intervals by a nociceptive stimulus, the skin-pinch test, applied to the sole of the animal's front paw [23]. The recording started with a negative test response, i.e. when the rat stopped responding with a reflex withdrawal of the limb. The monitoring was terminated on the reappearance of a positive pinch-test response, as the animal immediately started to move thereby terminating reliable data recording. The duration of recording varied from rat to rat and was on average 87 min. The measurements were at a constant room temperature of $24 \pm 1^\circ\text{C}$.

The EEG power spectrum is conventionally divided [24] into the frequency bands: δ (0.5–3.5 Hz); θ (3.5–7.5 Hz); α (7.5–12.5 Hz); β (12.5–25 Hz); γ_1 (25–35 Hz); γ_2 (35–50 Hz); and γ_3 (50–100 Hz). We calculated the time evolution within each band by application of the continuous wavelet transform [6]. The EEG signal was bandpass-filtered, but only after extensive investigation of its time-frequency content by wavelet analysis, and particular care taken to avoid any introduction of phase lags.

The transition from deep to light anaesthesia was determined by application of several criteria: as the times when both cardiac and respiratory frequencies significantly increased and became significantly more variable [22]; as the times when the amplitude of δ -waves dramatically decreased; and as the times when the amplitudes of θ and γ significantly increased. These different criteria yielded consistent results. The transition is most probably associated with the effects of the ketamine wearing off faster than those of xylazine so that in the light phase the effect of xylazine is dominant.

3. Fokker–Planck analysis

We define a state vector $\mathbf{q} = \{\delta(t), \theta(t)\}$ composed of the signals of the δ and θ bands, hypothesize that it follows a stochastic process of form

$$\partial_t q_i = D_i^{(1)}(\mathbf{q}, t) + \sum_{j=1}^2 \sqrt{D_{ij}^{(2)}(\mathbf{q}, t)} \Gamma_j(t),$$

and approximate the fluctuations $\Gamma_j(t)$ by Gaussian white noise. We suppose that the process is Markovian, an assumption that can subsequently be validated by data analysis. The drift vector $\mathbf{D}^{(1)}$ describing the deterministic part of the dynamics, and the diffusion matrix $\mathbf{D}^{(2)}$ determining the strength of the driving noise, are

$$\begin{aligned} D_i^{(1)}(\mathbf{q}, t) &= \lim_{\tau_M \rightarrow 0} \frac{1}{\tau_M} \langle (q_i(t + \tau_M) - q_i(t)) | \mathbf{q}, t \rangle, \\ D_{ij}^{(2)}(\mathbf{q}, t) &= \lim_{\tau_M \rightarrow 0} \frac{1}{2\tau_M} \langle (q_i(t + \tau_M) - q_i(t))(q_j(t + \tau_M) - q_j(t)) | \mathbf{q}, t \rangle. \end{aligned} \tag{1}$$

We have used the Itô interpretation of the stochastic integral and conditional expectation values $\langle \cdot \rangle$ that can be determined from the experimental data; $\sqrt{\mathbf{D}^{(2)}}$ is to be calculated by diagonalizing the matrix $\mathbf{D}^{(2)}$, taking the square root of each of its elements, and transforming the result back into the original system of coordinates [16].

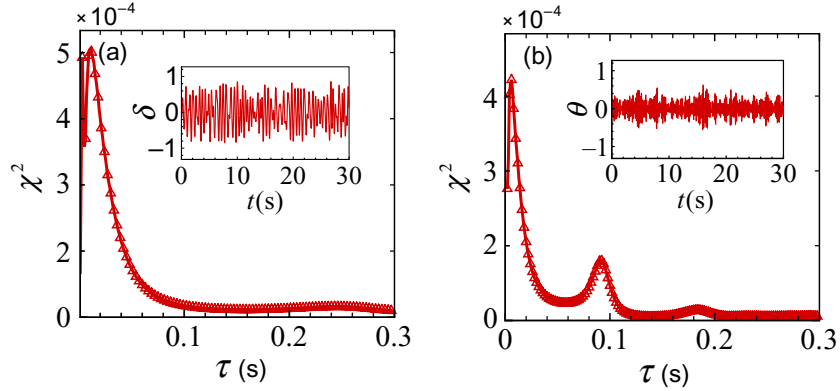


Figure 2. Plots of χ^2 to test the Markov property of (a) δ and (b) θ fluctuations in a rat's EEG as a function of timescale, τ . The minimum value of χ^2 occurs around $\tau_M \simeq 0.1$ s, corresponding to the Markov timescale within a σ confidence level. The insets plot short samples of the signals being analysed.

The Markov condition requires an n -point conditional probability function (CPF) $P(\mathbf{q}(t + n\tau) | \mathbf{q}(t + (n-1)\tau), \dots, \mathbf{q}(t + \tau), \mathbf{q}(t))$ to be equal to a two-point CPF $P(\mathbf{q}(t + n\tau) | \mathbf{q}(t + (n-1)\tau))$. The timescale τ in which this condition is fulfilled is the *Markov timescale* (τ_M). For multidimensional stochastic variables, it is hardly possible to check the Markov condition directly by means of n -point CPFs. We therefore use three-point CPFs, for which the Markov condition corresponds [25] to

$$\chi^2 = \int \left(\prod_{i=1}^3 dx_i \right) \frac{[P(x_3, x_2, x_1) - P(x_3|x_2)P(x_2, x_1)]^2}{\sigma_J^2 + \sigma_M^2} \quad (2)$$

being zero. Here,

$$x_3 = x_3(t + 2\tau), \quad x_2 = x_2(t + \tau), \quad x_1 = x_1(t),$$

and x represents one of the components of \mathbf{q} , i.e. q_i . σ_J^2 and σ_M^2 are the variances of $P(x_3, x_2, x_1)$ and $P(x_3|x_2)P(x_2, x_1)$, respectively. Figure 2 shows χ^2 calculated for both δ and θ waves from a rat EEG signal as a function of the timescale τ . In both cases, the minimum value of χ^2 occurs just after 0.1 s, after which it hardly changes, corresponding to τ_M with one σ confidence level.

Using equation (1) with this value of τ_M , we can estimate the drift and diffusion coefficients from $\delta(t)$ and $\theta(t)$ as shown in figure 3. In doing so, we used 1D coefficients, i.e. in deriving the drift and diffusion coefficients for each variable, the effect of the other variable was integrated. Both coefficients can be well-approximated by low-order polynomials. The $D_i^{(1)}$ with $i = \delta, \theta$ indicate an overall damping behaviour, as shown earlier [26]. Moreover, the behaviour of $D_{\delta\delta}^{(2)}$ and $D_{\theta\theta}^{(2)}$ implies that the noise is multiplicative in character: constant diffusion coefficients represent additive noise whereas, for multiplicative noise, the diffusion coefficients are functions of the dynamical variables. We tested whether the deviation from additive behaviour is attributable to the finiteness of τ_M [27] by consideration [28] of a Taylor expansion of the drift coefficients. We conclude that the effect of the higher order terms in τ_M cannot explain the apparently multiplicative nature of the estimated second coefficient, which implies that the noise strengths are functions of the dynamical variables.

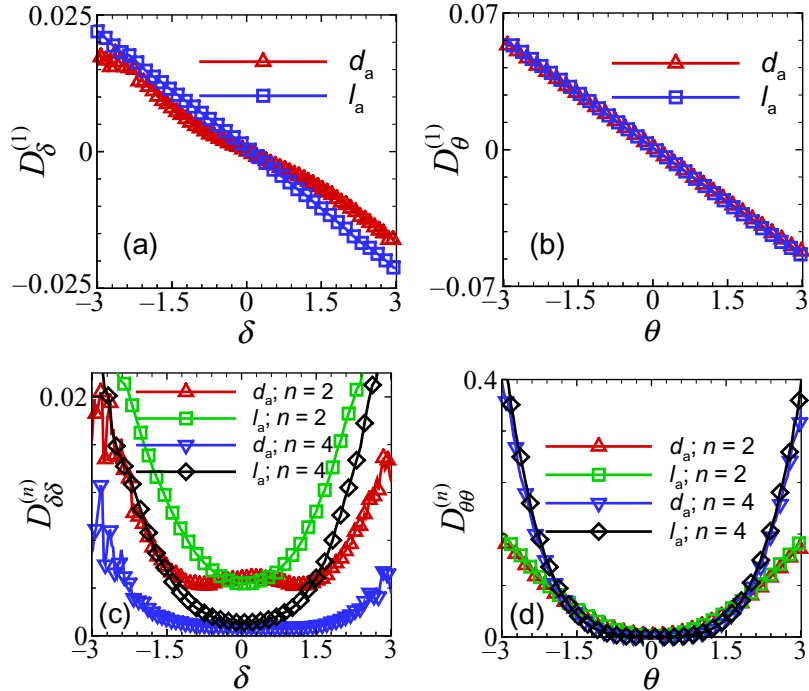


Figure 3. Plots of the derived drift, diffusion and fourth-order Kramers–Moyal coefficients for the EEG of a typical rat in the deeply and lightly anaesthetized states (indicated by d_a and l_a , respectively). (a) Drift coefficient for the EEG δ band. (b) Drift coefficient for the θ band. (c) Diffusion and fourth-order Kramers–Moyal coefficients related to the δ band. (d) Diffusion and fourth-order Kramers–Moyal coefficients related to the θ band. The results of (a) and (c) clearly demonstrate different functionality for both the drift and diffusion coefficients during deep as compared with light anaesthesia.

4. Application to δ and θ brain waves in anaesthesia

Figures 3(a) and (c) show that there are significant differences in the δ waves between deep and light anaesthesia, consistent with earlier work [22]. On the other hand, panels (b) and (d) show that little change occurs in the θ waves. The functionality of $D_{\delta\delta}^{(2)}$ changes markedly between the two states as can be seen in figure 3(c): in the light phase, a parabola fits this coefficient very well, while for deep anaesthesia we must use a fourth-order function to describe the central peak.

4.1. Stationary solution for retrieved drift and diffusion coefficients

We can also examine qualitatively the stationary solution of the Fokker–Planck equation around the different extrema in $D_2(\delta)$. The solution is $P_{\text{stationary}} = \frac{N_0}{D^2(\delta)} \exp(-\int d\delta \frac{D^{(1)}}{D^{(2)}})$, where the integration constant N_0 can be derived by normalization of $P_{\text{stationary}}$. For simplicity, we suppose that $D_\delta^{(1)}$ is well approximated by a line ($D_\delta^{(1)} = -b\delta$ where $b > 0$). In light anaesthesia, $D_{\delta\delta}^{(2)}$ has a minimum at $\delta = 0$, whereas in the deep state there is a local maximum there. Focusing on

the region around this point, $D_{\delta\delta}^{(2)}$ can be approximated as $D_{\delta\delta}^{(2)} \simeq D_{\delta\delta}^{(2)}(0) \mp \frac{1}{2}|D_{\delta\delta}^{(2)''}|\delta^2$, where ' \cdot ' denotes $d/d\delta$. It is evident that the contribution of $D_{\delta\delta}^{(2)}$ to the stationary solution of the Fokker–Planck equation changes between deep and light anaesthesia. Two additional extrema (minima) appear in $D_{\delta\delta}^{(2)}$ during deep anaesthesia (figure 3(c)), causing a double-humped PDF in deep anaesthesia (cf the single-humped PDF during light anaesthesia).

To test whether the behaviour of the system deviates from a Langevin description, we calculated the fourth-order coefficients $D^{(4)}(x) = \lim_{\tau_M \rightarrow 0} \frac{1}{24\tau_M} \langle (x(t+\tau) - x(t))^4 \rangle$ for $x = \delta$ and θ , allowing us to determine whether the driving noise process $\Gamma_j(t)$ exhibits deviations from a Gaussian distribution [16]. Only if $D^{(4)}$ vanishes is $\Gamma_j(t)$ white Gaussian. The probability density function (PDF) of the process then evolves according to a Fokker–Planck or, equivalently, Langevin equation [16]. Figure 3 shows that $D_\delta^{(4)}$ is slightly above zero, but the magnitude of this coefficient is less than one-fifth of the second coefficient $D_{\delta\delta}^{(2)}$, for both deep and light anaesthesia. The fluctuations for the case of light anaesthesia are larger than for the deep state. This can be seen from the observation that, in the domain of $[-3\sigma, 3\sigma]$ in figure 3(c), the $D_\delta^{(4)}$ terms are bigger in the light case, which indicates greater fluctuation amplitude. In contrast, for the θ band signals, $D_\theta^{(4)}$ compared with $D_{\theta\theta}^{(2)}$ was clearly above zero for both deep and light anaesthesia suggesting that a 1D Langevin description may be inadequate for modelling δ – θ activities.

In a 1D Langevin model, the effects of other components are integrated, e.g. the 2D drift and diffusion coefficients can be integrated to yield the 1D ones as $D_i^{(1)}(x'_i) = \int D_i^{(1)}(x_i, x_j) P(x_i|x'_i, x_j) dx_j$ and $D_{ii}^{(2)}(x'_i) = \int D_{ii}^{(2)}(x_i, x_j) P(x_i|x'_i, x_j) dx_j$. Obviously, the information about interactions and their directionality is lost. This is an important point: although we have clearly different functionality for $D_{\delta\delta}^{(2)}$ and a different pattern for $D_\delta^{(1)}$, the differences are unclear in the case of the θ component and we should not thoughtlessly integrate out the effects of the other variable. So, next, we derive the drift and diffusion coefficients as functions of both δ and θ . Figure 4 shows all the coefficients calculated for deep anaesthesia. Figures 4(a) and (b) plot $D_\delta^{(1)}(\delta, \theta)$ and $D_\theta^{(1)}(\delta, \theta)$. The θ -component of the drift vector shows an almost linear dependence on θ and only weak variations with δ . But interestingly, the δ -component of the drift vector has strong functionality in both δ and θ (see figure 4(a)). We used a 2D least-squares method to derive the functionality of the coefficients. In the case of θ , we have $D_\theta^{(1)}(\delta, \theta) = a + b\delta + c\theta$ with good precision and the value of b is small ($|c/b| \simeq 10$ for all rats), while in the case of δ the situation changes dramatically. The best fit available is a third-order polynomial with respect to δ and θ , $D_\delta^{(1)}(\delta, \theta) = \sum_{m,n} a_n^m \delta^m \theta^n$ ($m+n = 0, 1, 2, 3$). In figures 4(c) and (d), we plot the coefficients $D_{\delta\delta}^{(2)}$ and $D_{\theta\theta}^{(2)}$ of the diffusion matrix. It is evident that $D_{\theta\theta}^{(2)}$, like $D_\theta^{(1)}$, depends weakly on δ . In both cases, a second-order polynomial of δ and θ such as $\sum_{m,n} a_n^m \delta^m \theta^n$ ($m+n = 0, 1, 2$) can describe the functionality of the two diffusion components. In case of light anaesthesia, we find similar functionality albeit with different parameters for the diffusion coefficients; but we find different functionality for the δ -component of the drift coefficient, which has a much weaker dependence on θ . It was found that these same patterns were repeated for all ten rats. Thus, they can be used to characterize the dynamical behaviour of the δ and θ brain activities.

The fact that $D_\delta^{(1)}$ and $D_{\delta\delta}^{(2)}$ have strong dependence on both δ and θ , whereas the $D_\theta^{(1)}$ and $D_{\theta\theta}^{(2)}$ hardly vary at all with δ , shows that the EEG θ component influences the δ -component but not vice versa. This situation persists regardless of depth of anaesthesia.

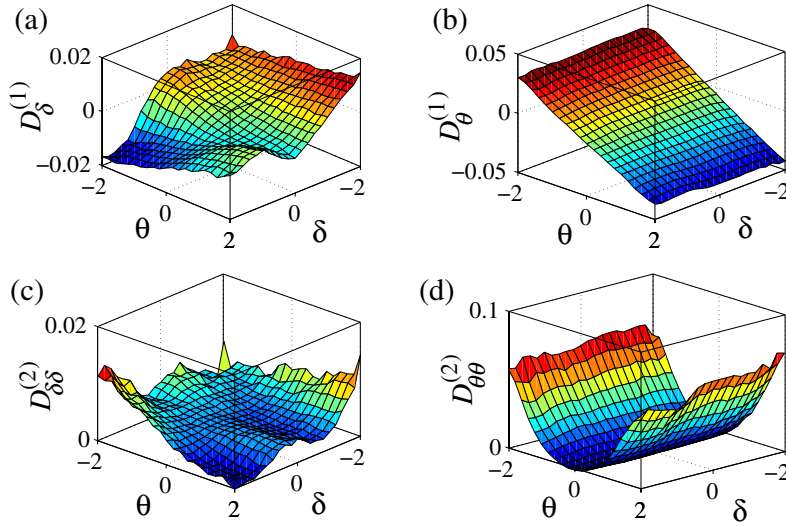


Figure 4. 2D drift, diffusion and fourth-order Kramers–Moyal coefficients for the deeply anaesthetized state of the same rat as in figure 3. (a) Drift coefficient for the EEG δ band and (b) for the θ band. (c) The $\delta\delta$ -component of the diffusion matrix and (d) its $\theta\theta$ -component. In all four figures, the amplitudes are increasing from dark blue to dark red. $D_\delta^{(1)}$ and $D_{\delta\delta}^{(2)}$ have strong dependences on both δ and θ , whereas the dependence of $D_\theta^{(1)}$ and $D_{\theta\theta}^{(2)}$ on δ is weak.

4.2. Dynamics and fixed points (FPs)

To complete the analysis we need to derive a more quantitative description of the patterns appearing in the drift and diffusion coefficients. The generated Langevin equations give the deterministic and stochastic parts of dynamics, which can be written as $\partial_t q_i = \partial_t^D q_i + \partial_t^S q_i$, of which $\partial_t^D q_i = D_i^{(1)}$ is the deterministic part of the dynamics and $\partial_t^S q_i = \sum_{j=1}^2 \sqrt{D_{ij}^{(2)}} \Gamma_j$. Because of the finite noise we do not have clear control of the stochastic term so, for simplicity, we just compare the dynamics arising from the deterministic terms: we can derive the FPs and the stability exponents in the phase diagram from the deterministic parts of the δ and θ trends. We note that another way to determine asymmetries in coupling is from measures based on the drift and diffusion coefficients [29].

In carrying out these analyses, we used all data we had for each rat [22], i.e. for a measurement of duration 30 min we had $30 \times 60 \times 1000 = 1.8 \times 10^6$ sample data for our sampling frequency of 1000 Hz. Thus the results related to $D^{(1)}$, $D^{(2)}$, and $D^{(4)}$ are all supported by a good level of statistics. However, we have also checked our results by using different portions of data. We found that 5 min worth of data (300 k data samples) was sufficient to give us a robust estimation of $D^{(1)}$, $D^{(2)}$ and $D^{(4)}$. In relation to the Markov length scale τ_M we found that, although the results were obtained for $\tau_M = 0.1$ (100 sample data), a range of 80–120 samples gave the same results. Diverging from this range, however, would drive us into a regime where modelling based on the Markov process is no longer valid.

To examine the FPs and flows in the δ – θ phase space, we have to solve together:

$$\begin{aligned} \partial_t^D q_\delta &= D_\delta^{(1)}(\delta, \theta), \\ \partial_t^D q_\theta &= D_\theta^{(1)}(\delta, \theta), \end{aligned} \tag{3}$$

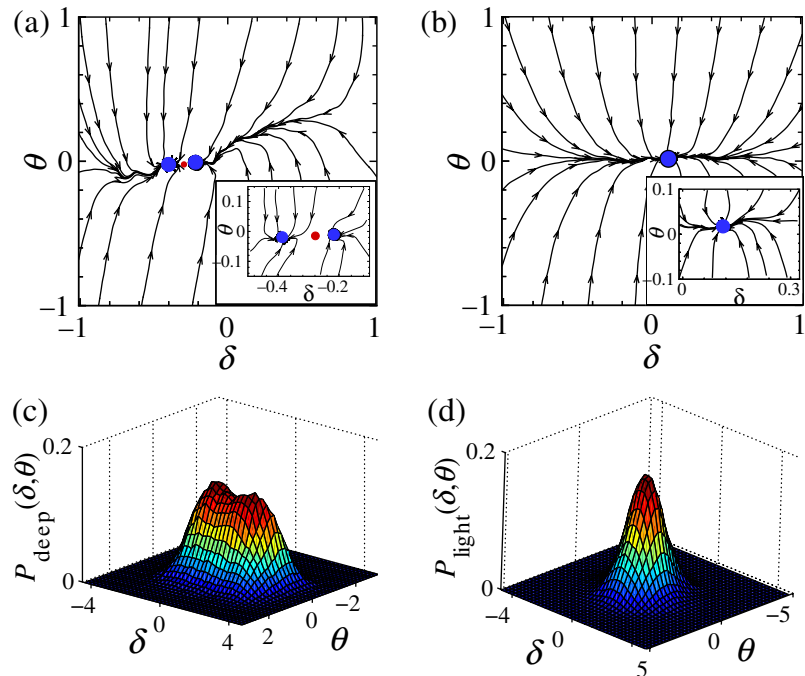


Figure 5. Comparison of the flow diagrams related to (a) deep and (b) light anaesthesia, derived from the deterministic part of the dynamics. Insets show in more detail the areas around the stable FPs (shown as blue dots) and unstable fixed point (red dot). The figure illustrates the different universality classes corresponding to deep and light anaesthesia. (c) and (d) show the joint PDF for deep and light regimes, $P_{\text{deep}}(\delta, \theta)$ and $P_{\text{light}}(\delta, \theta)$, respectively. The PDFs are evidently consistent with the results derived from the stability analyses shown in (a) and (b). The amplitudes of PDF plots are increasing from minimum in dark blue (zero) to maximum value at dark red.

for both deep and light anaesthesia. We find that there are two distinct regimes. Firstly, for eight out of ten rats during deep anaesthesia there are three nontrivial FPs. Two of them are stable in both the δ and θ directions, and the third one is unstable in the δ but stable in the θ direction. Figure 5(a) shows the flow diagrams related to equation (3) for a typical rat. There is a region outside the two stable FPs in δ - θ space in which the flows take any initial point to one of the stable FPs. However, when δ or θ are small enough that the initial point is close to the unstable fixed point, a small change in δ could take the flow to a different stable fixed point, hence implying that the joint PDF of the δ and θ , $P_{\text{deep}}(\delta, \theta)$, must have two distinctive peaks. Secondly, for all ten rats during light anaesthesia, we have only one attracting FP. Figure 5(b) shows that, for a typical rat, over the whole interval of δ and θ flows take any initial point to the stable fixed point. Hence, in this case, the system appears homogeneous at large timescales and we must have one peak for $P_{\text{light}}(\delta, \theta)$, unlike the previous case. To test this prediction, we plot in figures 5(c) and (d) the directly calculated PDFs $P_{\text{deep}}(\delta, \theta)$ and $P_{\text{light}}(\delta, \theta)$. They are in full agreement with the results of our stability analysis of drift coefficients. At least in the present experiments, therefore, we may conclude that the dynamics of δ - θ activity falls into different universality classes for the states of deep and light anaesthesia. However, this finding needs further investigation and will be a subject of our future work.

5. Tests of the validity of the results

We now describe some tests that we carried out to confirm that our results relate to the real dynamics of the system, and are not just artifacts of filtering. To do so, we processed a dummy signal consisting of Ornstein–Uhlenbeck noise [30] by filtration in the δ and θ bands and then repeated the whole analysis procedure. We used standard Ornstein–Uhlenbeck noise with an added sinusoidal interaction to simulate the external oscillatory components. The equation for the dynamical variable is

$$\dot{v} = -v(t) + A \sin(\omega t) + \sqrt{\xi} \eta(t) \quad (4)$$

where A corresponds to the coupling strength of the external oscillatory components, ξ is the noise strength, and η is the white Gaussian noise.

We always obtained one attracting FP, implying the damping structure of the system. Moreover, when analysing the empirical data with 5 min moving windows for the δ and θ bands of the real signals, we observed that the change of pattern between deep (3 FPs) to light (1 FP) anaesthesia occurs very sharply: we estimated the $D^{(1)}$, $D^{(2)}$ for one window of data, and then repeated the whole process explained in sections 4.1 and 4.2 by first deriving the functionality of $D^{(1)}$ and $D^{(2)}$ based on the dynamical variables, and then applying stability analysis to the deterministic parts of the processes (similar to the procedure explained in section 4.2). Interestingly we found that even with the short 5 min data windows, we could distinguish clearly between two different phases, having 3 and 1 FPs for deep and light anaesthesia, respectively, the transition from one to the other being related to the transition from deep to light anaesthesia, which occurs very sharply ($\sim 1\text{--}2$ min).

Finally, we investigated the question of whether or not the same results can be derived from the phase dynamics of the variables δ and θ . We used the Hilbert transform [31] to detect the corresponding phases; we calculated the time interval for each period of the phase; and we inverted these time series to derive new signals in frequency space. Note that the phases of δ and θ are defined only in a statistical sense because both waves are relatively broad in frequency. It is only δ waves in deep anaesthesia that are relatively localized in frequency. For further details see [22].

We then processed the δ and θ phases using the Fokker–Planck formalism. Reassuringly, but unsurprisingly, there were no significant differences between the drift and diffusion coefficients corresponding to the δ and θ phases in deep and light anaesthesia (not shown here).

6. Concluding remarks

In conclusion, our Fokker–Planck analysis of EEG signals has provided evidence of interactions between the EEG δ and θ wave activities in rats in deep and light anaesthesia. We have characterized the functionalities of δ and θ and shown that the functionality of δ alters with changes in depth of anaesthesia. It is commonly accepted that sleep or anaesthetic-induced unconsciousness arises through changes in the conduction of ion channels. Ketamine inhibits [32] NMDA⁴ and Muscarinic ACh-sensitive⁵ channels, which may occur through two

⁴ NMDA stands for N-methyl D-aspartate. Activation of NMDA receptors results in the opening of the ion channel.

⁵ ACh stands for acetylcholine. Activation of Muscarinic ACh-sensitive receptors results in the opening of the ion channel.

distinct mechanisms: (i) ketamine blocks open channels thereby reducing their mean open time; or (ii) it decreases the frequency of channel opening. Either mechanism would lead to neuronal hyperpolarization and reduce the activation of action potentials. The consequence of the hyperpolarization is that the function of neurons is blocked. Where exactly this occurs is currently unknown. Specific suppression of activity in the regional-thalamic and mid-brain reticular formation and hyperpolarization blockage of thalamocortical neurons has been discussed [33]. On the other hand, ketamine is considered as a drug that does not reduce cortical metabolism and glutamate release or depress sensory information flow through the thalamus [34]. Our observation that θ drives δ , regardless of depth of anaesthesia is consistent with this picture. It is an important result, suggesting that the changes in δ -activity during deep anaesthesia or sleep are mainly due to reduced sensory information from the spinal cord to the thalamus, rather than on account of reduced thalamocortical interactions. However, the physiological and neurological implications of this finding remain to be further investigated.

Acknowledgments

We thank B Musizza for making the signals available. We are grateful for useful discussions with him, MRR Tabar and A Hale. The research was supported by the FP6 NEST-Pathfinder project BRACCIA, the Wellcome Trust and the Engineering and Physical Sciences Research Council (UK). FG was supported by the Alexander von Humboldt Foundation (Germany).

References

- [1] Freeman W J, Kozma R and Werbos P J 2001 Biocomplexity: adaptive behavior in complex stochastic dynamical systems *Biosystems* **59** 109–23
- [2] Kantz H and Schreiber T 2003 *Nonlinear Time Series Analysis* (Cambridge: Cambridge University Press)
- [3] Boccara N 2004 *Modeling Complex Systems* (Berlin: Springer)
- [4] Caruso A, Gargano M E, Valenti D, Fiasconaro A and Spagnolo B 2005 Cyclic fluctuations, climatic changes and role of noise in planktonic foraminifera in the Mediterranean sea *Fluctuation Noise Lett.* **5** L349–55
- [5] Berger H 1929 Ueber das Elektroenkephalogramm des Menschen *Arch. Psychiatr. Nervenkr.* **87** 527–70
- [6] Stefanovska A and Bračič M 1999 Physics of the human cardiovascular system *Contemp. Phys.* **40** 31–55
- [7] Gans F, Schumann A Y, Kantelhardt J W, Penzel T and Fietze I 2009 Cross-modulated amplitudes and frequencies characterize interacting components in complex systems *Phys. Rev. Lett.* **102** 098701
- [8] Hlavackova-Schindler K, Paluš M, Vejmelka M and Bhattacharya J 2007 Causality detection based on information-theoretic approaches in time series analysis *Phys. Rep.* **441** 1–46
- [9] Cimponeriu L, Rosenblum M and Pikovsky A 2004 Estimation of delay in coupling from time series *Phys. Rev. E* **70** 046213
- [10] Jamšek J, Stefanovska A, McClintock P V E and Khovanov I A 2003 Time-phase bispectral analysis *Phys. Rev. E* **68** 016201
- [11] Smelyanskiy V N, Luchinsky D G, Stefanovska A and McClintock P V E 2005 Inference of a nonlinear stochastic model of the cardiorespiratory interaction *Phys. Rev. Lett.* **94** 098101
- [12] Arnhold J, Grassberger P, Lehnertz K and Elger C E 1999 A robust method for detecting interdependences: application to intracranially recorded EEG *Physica D* **134** 419–30
- [13] Romano M C, Thiel M, Kurths J and Grebogi C 2007 Estimation of the direction of the coupling by conditional probabilities of recurrence *Phys. Rev. E* **76** 036211
- [14] Schreiber T 2000 Measuring information transfer *Phys. Rev. Lett.* **85** 461–4

- [15] Paluš M and Stefanovska A 2003 Direction of coupling from phases of interacting oscillators: an information-theoretic approach *Phys. Rev. E* **67** 055201
- [16] Risken H 1984 *The Fokker–Planck equation* (Berlin: Springer)
- [17] Moss F and McClintock P V E (ed) 1989 *Noise in Nonlinear Dynamical Systems* vol 1–3 (Cambridge: Cambridge University Press)
- [18] Siegert S, Friedrich R and Peinke J 1998 Analysis of data sets of stochastic systems *Phys. Lett. A* **243** 275–80
- [19] Risken H 1993 *The Fokker–Plank Equation* 2nd edn (Berlin: Springer))
- [20] Friedrich R, Peinke J and Renner C 2000 How to quantify deterministic and random influences on the statistics of the foreign exchange market *Phys. Rev. Lett.* **84** 5224–7
- [21] Friedrich R, Siegert S, Peinke J, Luck S, Siefert M, Lindemann M, Raethjen J, Deuschl G and Pfister G 2000 Extracting model equations from experimental data *Phys. Lett. A* **271** 217–22
- [22] Musizza B, Stefanovska A, McClintock P V E, Paluš M, Petrovčič J, Ribarič S and Bajrović F F 2007 Interactions between cardiac, respiratory and EEG- δ oscillations in rats during anaesthesia *J. Physiol.* **580** 315–26
- [23] Bajrović F and Sketelj J 1998 Extent of nociceptive dermatomes in adult rats is not primarily maintained by axonal competition *Exp. Neurol.* **150** 115–21
- [24] John E R 2002 The neurophysics of consciousness *Brain Res. Rev.* **39** 1–28
- [25] Ghasemi F, Bahraminasab A, Movahed M S, Rahvar S, Sreenivasan K R and Tabar M R R 2006 Characteristic angular scales in cosmic microwave background radiation *J. Stat. Mech.* P11008
- [26] Prusseit J and Lehnertz K 2007 Stochastic qualifiers of epileptic brain dynamics *Phys. Rev. Lett.* **98** 138103
- [27] Ragwitz M and Kantz H 2001 Indispensable finite time corrections for Fokker–Planck equations from time series data *Phys. Rev. Lett.* **87** 254501
- [28] Friedrich R, Renner C, Siefert M and Peinke J 2002 Comment on ‘Indispensable finite time corrections for Fokker–Planck equations from time series data’ *Phys. Rev. Lett.* **89** 149401
- [29] Prusseit J and Lehnertz K 2008 Measuring interdependences in dissipative dynamical systems with estimated Fokker–Planck coefficients *Phys. Rev. E* **77** 041914
- [30] Gardiner C W 2004 *Handbook of Stochastic Methods* (New York: Springer)
- [31] Pikovsky A, Rosenblum M and Kurths J 2001 *Synchronization Universal—A Concept in Nonlinear Sciences* (Cambridge: Cambridge University Press)
- [32] Alkire M T 2008 Consciousness and anesthesia *Science* **322** 876–80
- [33] Alkire M T, Haier R J and Fallon J H 2000 Toward a unified theory of narcosis: brain imaging evidence for a thalamocortical switch as the neurophysiologic basis of anesthetic-induced unconsciousness *Conscious Cogn.* **9** 370–86
- [34] Rudolph U and Antkowiak B 2004 Molecular and neuronal substrates for general anaesthetics *Nat. Rev. Neurosci.* **5** 709–20

Nonstationary Langevin equation: Statistical properties and application to explain effects observed in cardiological time series

Jens Kirchner,* Wolfgang Meyer, Markus Elsholz, and Bernhard Hensel
*Max Schaldach-Stiftungsprofessur, Center for Medical Physics and Engineering,
 Friedrich-Alexander-Universität Erlangen-Nürnberg, Germany*

(Received 2 October 2006; revised manuscript received 15 May 2007; published 16 August 2007)

Using the Langevin equation we develop the model of a stochastic process subject to a given time-dependent regulatory mechanism. The effects of this nonstationarity on the statistical properties of the time series, i.e., on global and conditional probability densities and on the moments of the distribution, are derived. Application of these results on simple model trends allows one to approximate cardiological data and thus to explain effects recently observed in the reconstruction of the deterministic part of the Langevin equation for time series of heart rate.

DOI: 10.1103/PhysRevE.76.021110

PACS number(s): 05.40.-a, 05.10.Gg, 05.45.Tp, 87.19.Hh

I. INTRODUCTION

The human cardiovascular system as an open system is subject to varying environmental influences, which it has to adapt to in order to maintain the vital functions of the organism. Measured cardiological signals and time series of the RR intervals, i.e., of the distance between successive R peaks in the ECG, in particular are thus a superposition of deterministic reactions of the system to this changing input from the environment on a variety of time scales, as well as of noise sources within the body itself. Hence, in 24-h recordings of heart rate particularly circadian variation reflects different exposures of the body during day and night (see Figs. 1 and 2) [1,2]. Methods for extracting the parameters of such oscillatory behavior have been presented by Nelson *et al.* [3] and for more complex trends by Fernández and Hermida [4].

However, while the long-range behavior of the cardiovascular system, such as 24-h oscillations or phases of physical activity, can typically be related to the patient's specific activity, splitting heart rate into a deterministic and a stochastic part on small time scales is feasible only in rare cases such as respiratory oscillations. In order to model such time series, an equation of motion is hence needed comprising terms that represent deterministic regulations as well as noise sources. This purpose is served by the Langevin equation.

Conceived for describing the motion of a Brownian particle [5] the original equation more generally covers stochastic processes with linear damping [6,7]. In the so-called "Langevin approach" [8] the model is extended to include also the cases of nonlinear deterministic forces with additive noise. Using the definitions of a stochastic integral proposed by Itô [9] and Stratonovich [10] the Fokker-Planck equation of the process can be derived from the Langevin equation [8,11]. A further generalization of the model was achieved by admitting memory effects in the deterministic force [12–15]. Sometimes the name is even attributed to the whole class of processes including a stochastic force [7].

In this article we restrict ourselves to the case of a δ -correlated noise source. We will show that we are able to choose delay parameters in our model such that this simplification is applicable to the cardiovascular time series under examination. Furthermore, for this model, algorithms for reconstructing the drift and diffusion coefficients of the Fokker-Planck equation [16] as well as the coordinate-dependent functions in the Langevin equation [17] have been proposed and applied to a variety of synthetic and empirical data [18,19]. In particular, Kuusela *et al.* [20,21] as well as Ghasemi and co-workers [22] have recently used this method for the analysis of RR interval time series and have found characteristic differences in the shape of the reconstructed functions between healthy patients and those suffering from congestive heart failure.

Most publications basing on the Langevin equation limit their scope to stationary processes. From the considerations above, however, it is obvious that this assumption does not hold for time series of the cardiovascular system in general (see also Refs. [23–25]). Instead we have to model these signals as the result of a regulatory mechanism responding to changing stress or, relocating the nonstationarity into the adaptation mechanism itself and thus omitting to explicitly predefine an input signal, as the product of a time-varying regulation.

We therefore regard the signal under examination as following a time-dependent trend $\gamma(t)$. From the assumed antagonism between noise source and regulation on the target value γ , we derive the special form of the Langevin equation used for the subsequent analysis. The statistical properties of this model, i.e., the probability densities and the moments of the distribution are then calculated. In the second half of this article we use these results to demonstrate the effects on the algorithm mentioned above, if a process subject to time-varying regulation is treated as stationary: By analyzing the special case of a piecewise linear trend, we relate the two stable fixed points that were observed in cardiological data by Kuusela to distinct phases of constant physical stress, in particular during day and night.

*kirchner@biomed.uni-erlangen.de

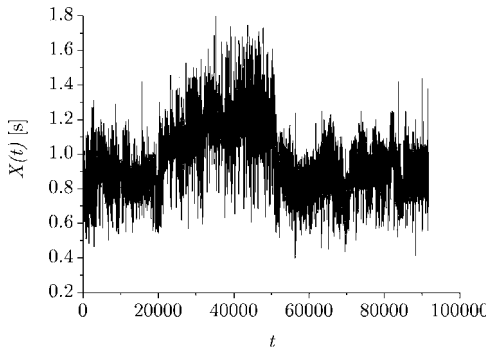


FIG. 1. 24-h time series of RR intervals $X(t)$ over beat number t .

II. MODEL

In order to develop the model used in this article we start from the Langevin equation as given by Risken [26],

$$\frac{dX(t)}{dt} = g[X(t), t] + h[X(t), t]\Gamma(t), \quad (1)$$

where the force g represents the deterministic mechanisms acting on $X(t)$. $\Gamma(t)$ is a stochastic process with zero correlation time, the amplitude of which is modulated by h .¹ Equation (1) is the most general form of a stochastic process with additive and δ -correlated noise $\Gamma(t)$; in comparison to Refs. [8,9,11,16–21] g and h additionally contain an explicit time dependency.

For the treatment of RR interval time series it has to be taken into account that $X(t)$ varies discretely with heart beat number. Hence, Eq. (1) has to be discretized by introducing a delay time τ [20,21]

$$X(t+\tau) - X(t) = g[X(t), t, \tau] + h[X(t), t]\Gamma(t, \tau), \quad (2)$$

where the form of the equation remains unchanged. For the application of our model to cardiological data it follows that both t and τ are positive integers, although the subsequent considerations will remain correct even for real-valued t and τ .

For the regulatory component represented by g we now assume a time-dependent set point $\gamma(t)$. In case of zero stochastic influences ($h \equiv 0$), $g[X(t), t, \tau]$ acts on X in such a way that $X(t+\tau)$ is set to the target value $\gamma(t+\tau)$, i.e. $X(t+\tau) = \gamma(t+\tau)$ for all $X(t)$. With Eq. (2) it follows that

$$g[X(t), t, \tau] = \gamma(t+\tau) - X(t). \quad (3)$$

Inserting g back into Eq. (2), now admitting stochastic influences, gives

¹The following considerations aim at processes with Gaussian probability density $\rho_\Gamma(x)$, as is often assumed for Langevin processes, but are applicable to more general ρ_Γ . Additional constraints will be given, if needed, at the respective positions in the text.

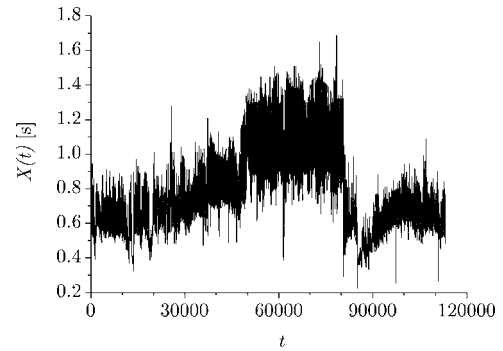


FIG. 2. 24-h time series of RR intervals $X(t)$ over beat number t .

$$X(t+\tau) = \gamma(t+\tau) + \Gamma(t, \tau), \quad (4)$$

where we have set $h \equiv 1$ for mathematical simplicity.² Then $X(t)$ is a linear combination of the two variables $\gamma(t)$ and $\Gamma(t, \tau)$, which are independent of each other. This fact will allow us to express the probability density of the process $X(t)$ in terms of the densities $\rho_\gamma(x)$ and $\rho_\Gamma(x)$ that are associated to the individual processes of the trend and the noise source.

Equation (4) will serve as model in the subsequent analysis. Thereby the following notation will be used: The signal $X(t)$ is observed during a time interval $I_t = [0, T]$. For $t \in I_t$, $\gamma(t)$ varies continuously within $I_\gamma = \gamma(I_t) = [\gamma_{\min}, \gamma_{\max}]$.

III. PROBABILITY DENSITIES

In order to derive the statistical properties of $X(t)$, both components $\gamma(t)$ and $\Gamma(t, \tau)$ of the signal are treated as stochastic processes with associated probability densities $\rho_\gamma(x)$ and $\rho_\Gamma(x)$.

A. Global probability density

With X regarded as the sum of the two independent random variables γ and Γ its probability density $\rho(x)$ directly follows [27]

$$\rho(x) = \rho[\gamma(t) + \Gamma(t-\tau, \tau)] = [\rho_\gamma * \rho_\Gamma](x), \quad (5)$$

where

$$[\rho_\gamma * \rho_\Gamma](x) = \int_{-\infty}^{\infty} \rho_\gamma(s)\rho_\Gamma(x-s)ds \quad (6)$$

denotes the convolution of the probability densities of the individual processes.

It is then easy to show (see Appendix A) that the moments of X

²In order to take into account the increase of heart rate variability with mean heart rate [1] due to the raised sympathetic tone [implying $h=h(\gamma)$], $X(t)$ has to be rescaled by dividing Eq. (4) by $h(\gamma)$. In this case $\frac{\partial h}{\partial x} < 0$ ensures $\frac{\partial}{\partial x} \frac{x}{h(x)} > 0$, so that the change of variables $x \rightarrow \frac{x}{h(x)}$ is bijective.

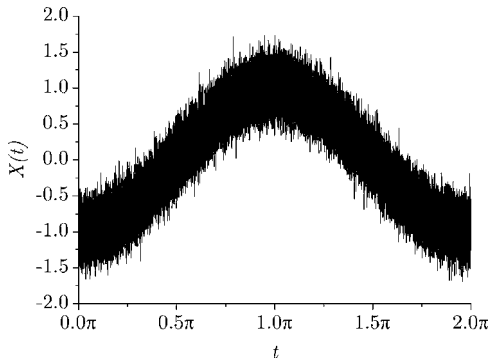


FIG. 3. Time series $X(t)$ of the cosine-shaped trend (13) ($A = -1$, $\omega = 1$) with superimposed white noise ($\sigma = 0.2$).

$$\langle X^n \rangle \equiv \int_{-\infty}^{\infty} x^n \rho(x) dx \quad (7)$$

can be related to the moments of $\gamma(t)$ and $\Gamma(t, \tau)$,

$$\langle \gamma^n \rangle \equiv \int_{-\infty}^{\infty} x^n \rho_\gamma(x) dx, \quad (8)$$

$$\langle \Gamma^n \rangle \equiv \int_{-\infty}^{\infty} x^n \rho_\Gamma(x) dx, \quad (9)$$

by the following equation:

$$\langle X^n \rangle = \sum_{k=0}^n \binom{n}{k} \langle \gamma^k \rangle \langle \Gamma^{n-k} \rangle. \quad (10)$$

In order to determine $\rho_\gamma(x)$ from an analytically given, continuous $\gamma(t)$, it is required that for every interval J the corresponding probability $P\{\gamma(t) \in J\}$ for $\gamma(t)$ to be found in J is given by the length of time, when $\gamma(t)$ varies within J . From this it is derived that

$$\rho_\gamma(x) = \frac{1}{\|I_t\|} \left| \left[\frac{d}{ds} \gamma^{-1}(s) \right]_{s=x} \right| \quad (11)$$

for monotone $\gamma(t)$ and

$$\rho_\gamma(x) = \frac{1}{\|I_t\|} \sum_{k: x \in I_\gamma^{(k)}} \left| \left[\frac{d}{ds} \gamma_k^{-1}(s) \right]_{s=x} \right| \quad (12)$$

in the general case (see Appendix B). Here $I_t = \bigcup_k I_t^{(k)}$ is the sampling interval, which is split up into disjoint subintervals such that $\gamma(t)$ is monotone on each $I_t^{(k)}$ with value set $I_\gamma^{(k)} = \gamma(I_t^{(k)})$. Then $\gamma_k^{-1}(x)$ is the inverse of the bijection $\gamma(t)$ on $I_t^{(k)}$. Equation (12) implies for piecewise defined $\gamma(t)$ on I_t that $\rho_\gamma(t)$ is constituted by the average of the densities on each subinterval.

B. Applications

As an example consider the cosine-shaped trend

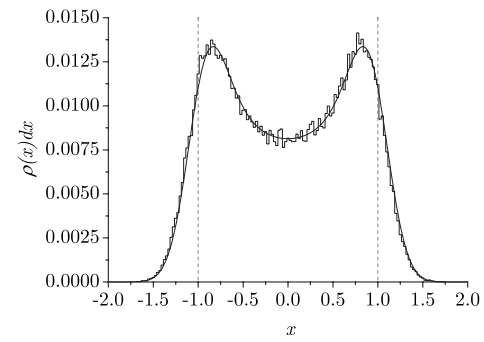


FIG. 4. Empirical probability distribution $\rho(x)dx$ determined from the time series in Fig. 3 (step function) and calculated by convolving ρ_γ and ρ_Γ (thick line). Note that the loci of the poles in $\rho_\gamma(x)$ (marked as dashed vertical lines) do not coincide with the maxima of $\rho(x)$.

$$\gamma(t) = A \cos(\omega t) \quad (13)$$

superimposed with white noise [Gaussian $\rho_\Gamma(x)$]. A realization of the time series $X(t)$ is shown in Fig. 3.

Using Eq. (12)

$$\rho_\gamma(x) = \frac{1}{\pi} \frac{1}{\sqrt{A^2 - x^2}} \quad (14)$$

is calculated by dividing $I_t = [0; 2\pi]$ into subintervals $I_t^{(1)} = [0; \pi]$ and $I_t^{(2)} = [\pi; 2\pi]$ with $\gamma(t)$ being monotone on each $I_t^{(k)}$. Numerical convolution of Eq. (14) and the Gaussian density $\rho_\Gamma(x)$ gives $\rho(x)$ plotted in Fig. 4. This theoretical prediction based on Eqs. (5) and (6) agrees with the probability distribution directly determined from the time series in Fig. 3.

It is evident from Eq. (14) that $\rho_\gamma(x)$ exhibits two singularities at $x = \pm A$ due to the vanishing first derivative at the extrema of $\gamma(t)$. More generally a flat tangent of the trend at some $\tilde{\gamma}$, e.g., caused by reversal points or phases of constant $\gamma(t)$, results in a singularity of $\rho_\gamma(x)$, which can be derived from Eq. (12). As a consequence the global probability density $\rho(x)$ will typically exhibit a local maximum at approximately $x = \tilde{\gamma}$ (see Fig. 4). However, if one wishes to extract information about $\gamma(t)$ from $\rho(x)$, it has to be noted that, as an effect of convolution, the maxima of ρ are not inevitably identical with $\tilde{\gamma}$: In Fig. 4 the maxima are shifted from $\tilde{\gamma} = \pm 1$ to smaller $|x|$, as $\rho_\gamma(x)$ is not symmetric about ± 1 .

For 24-h time series of RR intervals the effect of circadian variance can clearly be observed in the well-known bimodal probability distribution: As noted in the introduction the trend can in this case be approximated by a cosine-shaped function or, what will be shown later, by a $\gamma(t)$ being constant during day and night. In both cases $\rho_\gamma(x)$ exhibits two singularities which in turn cause a twice peaked probability distribution.

C. Conditional probability density

The conditional probability density $\rho(\hat{x}|x, \tau)$ for finding some $X(t+\tau) = \hat{x}$ given that its predecessor $X(t) = x$ is defined by

$$\rho(\hat{x}|x, \tau) d\hat{x} = P\{\hat{x} \leq X(t+\tau) \leq \hat{x} + d\hat{x} | X(t) = x\}. \quad (15)$$

Using the identity

$$\rho(\hat{x}|x, \tau) = \frac{\rho(\hat{x}, x|\tau)}{\rho(x)} \quad (16)$$

[27], where $\rho(x)$ is known from Eq. (5), the problem of calculating $\rho(\hat{x}|x, \tau)$ is shifted towards the question how to determine the joint density $\rho(\hat{x}, x|\tau)$ for finding t with $X(t)=x$ and $X(t+\tau)=\hat{x}$.

As $\Gamma(t, \tau)$ and $\Gamma(t+\tau, \tau)$ were assumed to be uncorrelated, the joint probability density $\rho(\hat{x}, x|\tau, t)$ for fixed t is written as the product of probabilities for two independent processes:

$$\begin{aligned} \rho(\hat{x}, x|\tau, t) d\hat{x} dx &= P\{X(t+\tau) \in [\hat{x}, \hat{x} + d\hat{x}]|t\} \\ &\times P\{X(t) \in [x, x + dx]|t\}. \end{aligned} \quad (17)$$

As γ is given by t and $t+\tau$ respectively, the probabilities only depend on the stochastic process Γ . Therefore

$$\rho(\hat{x}, x|\tau, t) = \rho_\Gamma[x - \gamma(t)] \rho_\Gamma[\hat{x} - \gamma(t+\tau)]. \quad (18)$$

The global conditional probability density is then calculated by integrating over the whole time series:

$$\rho(\hat{x}, x|\tau) = \frac{1}{T-\tau} \int_0^{T-\tau} \rho_\Gamma[x - \gamma(t)] \rho_\Gamma[\hat{x} - \gamma(t+\tau)] dt. \quad (19)$$

We consider the limiting case $\tau \approx 0$, which is valid for all τ with $\gamma(t) \approx \gamma(t+\tau)$. Using this approximation and changing the integration variable from t to γ

$$\begin{aligned} \rho(\hat{x}, x|0) &= \frac{1}{T} \int_{\gamma(0)}^{\gamma(T)} \rho_\Gamma[x - \gamma] \rho_\Gamma[\hat{x} - \gamma] \frac{dt}{d\gamma} d\gamma \\ &= \int_{I_\gamma} \rho_\Gamma[x - \gamma] \rho_\Gamma[\hat{x} - \gamma] \frac{1}{T} \left| \frac{1}{(d\gamma/dt)} \right| d\gamma \\ &\stackrel{(11)}{=} \int_{I_\gamma} \rho_\Gamma[x - \gamma] \rho_\Gamma[\hat{x} - \gamma] \rho_\gamma(\gamma) d\gamma. \end{aligned} \quad (20)$$

Here without loss of generality we assumed monotonically increasing $\gamma(t)$ and used the rule for differentiating the inverse of a function [28]. See Appendix C for the proof of Eq. (20) in the case of general $\gamma(t)$.

IV. STATIONARY TREATMENT OF THE MODEL: THE RECONSTRUCTION OF $g(x)$

Friedrich *et al.* have recently proposed a method for recovering the deterministic term $g(x)$ in Eq. (2) from experimental data [17], if the process under consideration is stationary. Observations based on this algorithm, e.g., number and stability of fixed points, however, are masked by a time dependency of the regulatory mechanism. In view of the wide field of applications indicated in the introduction it seems advisable to demonstrate how to determine the effects

of such trends on the shape of $g(x)$ and to calculate this function for some simple cases of $\gamma(t)$, which might serve as a first approximation of general time series.

A. Method of reconstruction

Assuming g and h to be functions of x only, Eq. (2) is averaged over time for all $X(t)=x$, yielding

$$g(x|\tau) = \langle X(t+\tau) - X(t) \rangle_{X(t)=x} = \langle X(t+\tau) \rangle_{X(t)=x} - x, \quad (21)$$

which is stated in Refs. [17,26] for the continuous case [Eq. (1)]. With the notation introduced above Eq. (21) is rewritten

$$g(x|\tau) = \int_{-\infty}^{+\infty} \hat{x} \rho(\hat{x}|x, \tau) d\hat{x} - x = \frac{1}{\rho(x)} \int_{-\infty}^{+\infty} \hat{x} \rho(\hat{x}, x|\tau) d\hat{x} - x. \quad (22)$$

In the limiting case $\tau \approx 0$

$$g(x) := g(x|0) = \frac{1}{\rho(x)} \int_{I_\gamma} s \rho_\Gamma(x-s) \rho_\gamma(s) ds + \int_{-\infty}^{+\infty} s \rho_\Gamma(s) ds - x \quad (23)$$

is obtained (see Appendix D for a proof).³ If $\rho_\Gamma(x)$ is symmetric around $x=0$ as in the case of Gaussian noise, the second term vanishes.

B. Special cases

The results derived above are applied on simple model trends, which allows one to approximate $\gamma(t)$ underlying empirical data.

1. Piecewise constant trend

A trend

$$\gamma(t) = \sum_k \xi_k \vartheta[I_t^{(k)}](t) \quad (24)$$

(with $\vartheta[J](t)=1$ for $t \in J$ and $=0$ otherwise), which is constant over subintervals $I_t^{(k)}$, gives an associated probability density

$$\rho_\gamma(x) = \sum_k \frac{\|I_t^{(k)}\|}{\|I_t\|} \delta(x - \xi_k). \quad (25)$$

By inserting this equation into Eq. (23)

³As we stated above, the approximation $\tau \approx 0$ is valid for all τ that are small compared to the time scale of the trend, i.e., if $\gamma(t) \approx \gamma(t+\tau) \forall t \in I_\gamma$. This allows one to apply the analysis of $g(x)$ to all $g(x|\tau)$ that are reconstructed by the use of Eq. (21) with an empirical τ that satisfies the given condition. Note that, in particular, $\tau \geq 1$ for discrete time series.

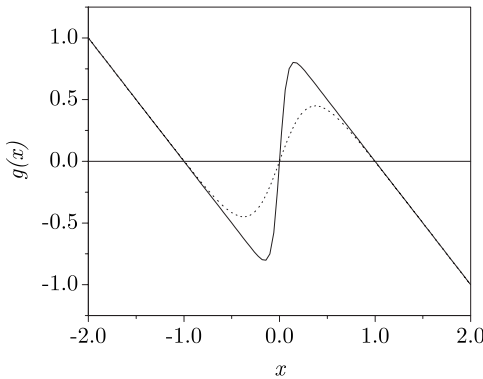


FIG. 5. $g(x)$ as given in Eq. (26) for white noise with $\xi_{1,2}=\pm 1$, $\|I_t^{(1)}\|=\|I_t^{(2)}\|$ and standard deviation $\sigma=0.4$ (continuous line) and $\sigma=0.8$ (dotted line), respectively.

$$g(x) = \frac{\sum_k \xi_k \|I_t^{(k)}\| \rho_\Gamma(x - \xi_k)}{\sum_k \|I_t^{(k)}\| \rho_\Gamma(x - \xi_k)} - x \quad (26)$$

is obtained under the assumption of symmetric $\rho_\Gamma(x)$. $g(x)$ is plotted in Fig. 5 for $k=2$, $\xi_{1,2}=\pm 1$, $\|I_t^{(1)}\|=\|I_t^{(2)}\|$ in the case of white noise with two different standard deviations σ . If the overlap of the $\rho_\gamma(x-\xi_k)$ can be neglected, $g(x)$ is approximated by a straight line with slope -1

$$g(x) = -x + \xi_k \vartheta[U(\xi_k)](x) \quad (27)$$

in some neighborhood $U(\xi_k)$ of ξ_k .

This analysis is confirmed by numerical simulations: By the use of Eq. (21) $g(x|1)$ is computed from a discrete time series subject to the trend

$$\gamma(t) = \begin{cases} -1 & t \in [0, 0.3T], \\ +1 & t \in [0.3T, T] \end{cases} \quad (28)$$

with additive white noise (Fig. 6). The two neighborhoods $U(\pm 1)$ can clearly be distinguished, while the relatively small value of σ leads to sharp edge at $x \approx 0$.

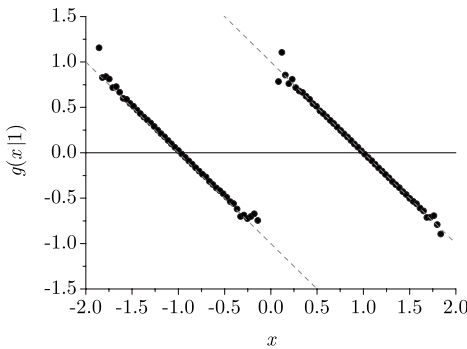


FIG. 6. $g(x|1)$ for the piecewise constant trend given in Eq. (28) superimposed with white noise ($\sigma=0.2$, $T=10^6$, $\tau=1$). According to Eq. (27) two neighborhoods $U(\xi_k)$ with zero crossings at $x=\xi_k$ are observed for $\xi_{1,2}=\pm 1$.

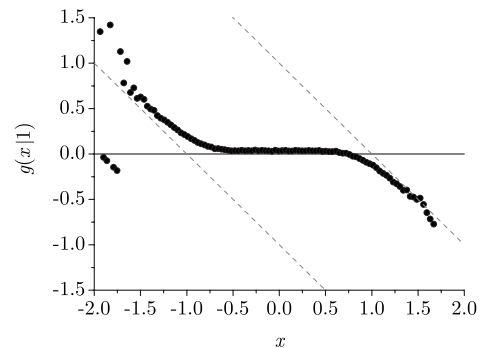


FIG. 7. $g(x|1)$ for the linearly increasing trend given in Eq. (29) superimposed with white noise ($\|I_\gamma\| = \frac{2}{\tau}$, $\gamma_{\min} = -1$, $\sigma = 0.2$, $T = 10^6$, $\tau = 1$). $g(x|1) \approx 0$ around $x=0$ and approaches linear behavior with slope -1 for large enough $|x|$.

2. Linear trend

A linearly increasing trend

$$\gamma(t) = \frac{\|I_\gamma\|}{\|I_t\|} t + \gamma_{\min} \quad (29)$$

has a constant probability density

$$\rho_\gamma(x) = \frac{\|I_t\|}{\|I_\gamma\|} \vartheta[I_\gamma](x). \quad (30)$$

Inserting this in Eq. (23) gives

$$g(x) = \frac{\int_{I_\gamma} \gamma \rho_\Gamma(x - \gamma) d\gamma}{\int_{I_\gamma} \rho_\Gamma(x - \gamma) d\gamma} - x \quad (31)$$

for symmetric $\rho_\Gamma(x)$.

If $\rho_\Gamma(x)$ is concentrated on some interval $I_\Gamma = [-\epsilon, \epsilon]$ and $x \in [\gamma_{\min} + \epsilon, \gamma_{\max} - \epsilon]$, then g vanishes, as can be seen in Fig.

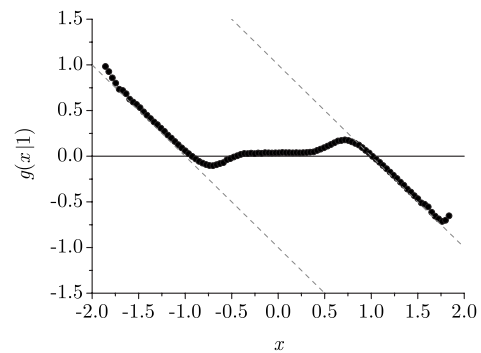


FIG. 8. $g(x|1)$ for the trend given in Eq. (32) superimposed with white noise ($\sigma=0.2$, $T=10^6$, $\tau=1$). x values at approximately 0 will mostly be found in the transitional phase of the time series, so that $g(x|1)$ coincides with g from Fig. 5 at $x \approx 0$. The linear phases with slope -1 and zero crossings at $x \approx \pm 1$, however, are due to the constant sections of $\gamma(t)$ with $\xi_{1,2}=\pm 1$.

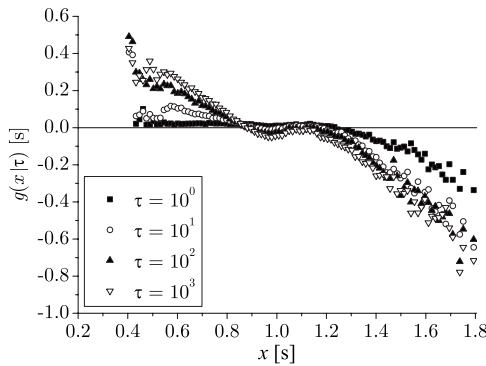


FIG. 9. $g(x|\tau)$ for the RR interval time series in Fig. 1. The two stability points at $x \approx 0.85$ and 1.1 s correspond to the averages of day and night phases, respectively. $g(x|\tau)$ flattens for decreasing τ due to correlations between successive heart beats.

7. For large enough $|x|$, g approaches linear behavior with slope -1 (see Appendix E for the proofs of the given results).

3. Piecewise constant trend with transitional phase

Empirical data is in a first approximation described as governed by a piecewise constant or linearly monotone $\gamma(t)$ as analyzed in the last two paragraphs. The combination of these two models describes constant phases as defined in Eq. (24), which are connected by a linear transition period analogous to Eq. (29). Figure 8 shows $g(x|1)$ for the trend

$$\gamma(t) = \begin{cases} -1, & t \in [0, 0.3T], \\ -1 + \frac{2t}{0.4T}, & t \in [0.3T, 0.7T], \\ +1, & t \in [0.7T, T] \end{cases} \quad (32)$$

with additive white noise. For $|x| > 1$ the same behavior as in Fig. 6 is observed: Decreasing g with slope -1 . For $x \approx 0$ in contrast the function is dominated by the transitional period: g is flattened between the two zero crossings. This effect is similar to the case, in which the standard deviation σ of the stochastic process $\Gamma(t, \tau)$ is increased (see Fig. 5).

C. Application to physiological data

Application of the method of reconstruction described above on 24-h time series of RR intervals has recently shown an n -stable deterministic force $g(x|\tau)$, where n typically equals to 2 [20,21]. Thereby a stable node was constituted by a zero crossing with negative slope. This observation is supported by our own data analysis, examples of which are displayed in Figs. 9 and 10.

For large enough time delay τ , $g(x|\tau)$ bears resemblance to our simulations in Figs. 5 and 8. This similarity is ascribed to the fact that the physiological data in Figs. 1 and 2 show significant differences in heart rate between day and night phases and therefore are in a first approximation modeled as being governed by a piecewise constant trend. Thus each phase of steady physical stress leads to a stable fixed point in g ; particularly a distinct circadian variation implies, beside a bimodal probability distribution as seen in the last section,

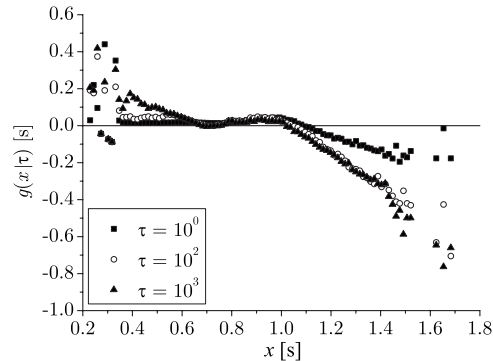


FIG. 10. $g(x|\tau)$ for the RR interval time series in Fig. 2. $g(x|\tau)$ exhibits a relatively flat region between the two stability nodes at $x \approx 0.7$ and 1.1 s due to the distinct transitional phase in the time series.

bistability in regard to the deterministic part of the Langevin equation.

The region of $g(x|\tau)$ in Figs. 9 and 10 between two stable fixed points is determined both by the standard deviation of the noise source and by the transition between the phases: As was shown above, g is flattened by increasing σ (Fig. 5) and by a long interval of strictly monotone $\gamma(t)$ (Figs. 6–8). Kuusela [21] indicates that such a plateau phase in the reconstructed g is characteristic for patients suffering of congestive heart failure. For this observation potential explanations are offered by the two effects mentioned: The deteriorated performance of the cardiovascular system might result in decelerated adaptation mechanisms and thus longer transitional phases. Simultaneously the two fixed points will draw nearer due to the reduced activity of the patient, which will raise, in spite of the decreased absolute heart rate variability [29–31], the relative value of σ . A decision on which explanation accounts for the differences between CHF patients and reference group is to be based on a careful analysis of the respective time series.

In the discussion above we have used the results that we derived from our model under the assumption of $\tau \approx 0$. Indeed the time delays used in Figs. 9 and 10 are small compared to the lengths of phases with constant $\gamma(t)$, which last $> 10^4$ beats. However, $g(x|\tau)$ exhibits a τ dependency, where the predictions from our model are best met at delays $> 10^2$ beats, while g flattens for decreasing τ . This results from correlations between successive heart beats including respiration and adaptation to environmental influences varying on time scales of seconds and minutes. Only if the parts of the signal that are modeled to be stochastic [Eq. (4)] are decorrelated, the assumption for Eq. (18) holds and the derived predictions are valid. Note that our predictions also fail, when τ is too large and $\gamma(t+\tau) \approx \gamma(t)$ does not hold any more: A time delay comparable to the lengths of the constant phases conceals circadian variation and instead suggests a stationary regulatory mechanism towards mean heart rate.

Our hypothesis, that bistability in g is caused by circadian variation, can be tested by applying the reconstruction algorithm to day and night phases of the time series separately: The sequence of RR intervals of Fig. 1 is split up into three parts as shown in Fig. 11. The associated $g(x|\tau)$ graphs are

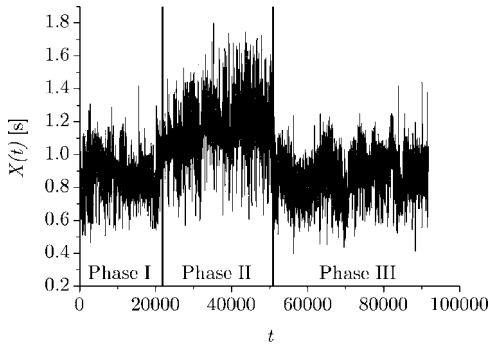


FIG. 11. 24-h time series of RR intervals $X(t)$ over beat number t as seen in Fig. 1. Day and night phases are separated by vertical lines.

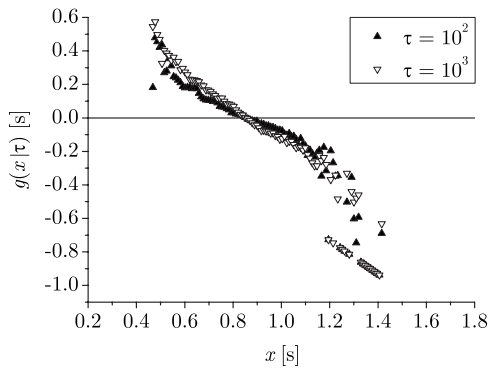


FIG. 12. $g(x|\tau)$ for phase I as given in Fig. 11 with $\tau=10^2$ and 10^3 . A single stable fixed point at $x\approx 0.85$ s is detected, corresponding to the leftmost zero crossing in Fig. 9.

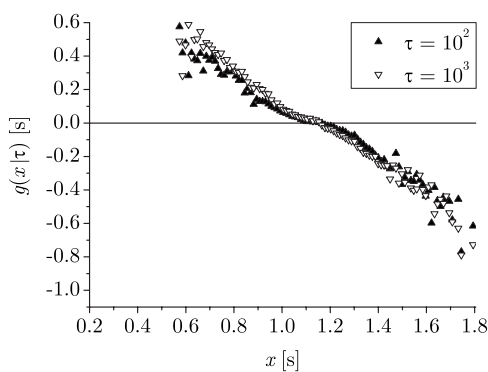


FIG. 13. $g(x|\tau)$ for phase II as given in Fig. 11 ($\tau=10^2$ and 10^3), exhibiting a single stable fixed point at $x\approx 1.15$ s.

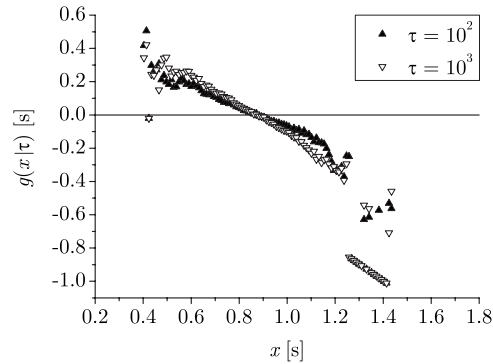


FIG. 14. $g(x|\tau)$ for phase III as given in Fig. 11 ($\tau=10^2$ and 10^3), exhibiting a single stable fixed point at $x\approx 0.85$ s.

given in Figs. 12–14 for $\tau=10^2$ and 10^3 . All of them are characterized by monostable behavior with a fixed point at $x\approx 0.85$ s (phases I and III) and 1.15 s (phase II), respectively. These values perfectly agree with those of the bistable $g(x|\tau)$ in Fig. 9, the shape of which is thus the result of the concatenation of the three stationary phases I–III to one single time series with a nonconstant trend.

Figures 12–14 match the observations of Ghasemi *et al.* [22], who also found linear $g(x|1)$ in 6-h time series, at least in the case of healthy patients. For persons suffering from congestive heart failure, however, a flat cubic dependence on x was suggested for the deterministic force. We suppose that these observations, which differ from the predictions derived from our model, are to be ascribed to the correlations present in the time series: As discussed above for Figs. 9 and 10, $g(x|\tau)$ flattens for decreasing τ , i.e., if the delay parameter approaches the correlation time. As Ghasemi and co-workers set $\tau=1$, their calculations are performed within the range of correlations, which they indicate themselves by determining the Markov time scale. The latter is significantly increased in CHF patients, which explains the deviations from our model, which comprises δ -correlated noise only.

The Langevin equation under study hence describes processes, for which values of the empirical delay parameter τ can be found, which are much larger than the correlation time of the data and yet negligible in comparison to the time scale of the trend. In the range of such adequate τ , however, the stable nodes of $g(x|\tau)$ become independent of the time delay and indicate ξ_i in case of a piecewise constant trend. As an application in cardiology, this offers the possibility to calculate mean heart rate of day and night phases, respectively, and thus to determine the range of these two stationary phases independently of potentially erroneous information such as diaries and markers.

V. SUMMARY

In this article the statistical properties of a stochastic process subject to a nonstationary regulatory mechanism have been analyzed: Global and conditional probability densities, as well as the moments of the distribution were derived and applied on several simple model systems. These results were used to explain observations recently made for RR interval

time series: Both a polymodal probability distribution and polystability displayed in the deterministic term of the Langevin equation were in a mathematically stringent way traced back to a common cause, phases of different physical stress, especially circadian variation. Moreover we offered explanations for the differences in the shape of g between CHF patients and the reference group of healthy subjects.

ACKNOWLEDGMENTS

We thank Jörg O. Schwab from University of Bonn, Department of Medicine (Cardiology), for providing the 24-h time series of ECG data that we used for demonstration.

APPENDIX A: DERIVATION OF EQ. (10)

Equation (7) defines the moments of X

$$\langle X^n \rangle = \int_{-\infty}^{\infty} x^n \rho(x) dx \stackrel{(5),(6)}{=} \int_{-\infty}^{\infty} x^n \int_{-\infty}^{\infty} \rho_{\gamma}(s) \rho_{\Gamma}(x-s) ds dx \\ \stackrel{u:=x-s}{=} \int_{-\infty}^{\infty} \rho_{\gamma}(s) \int_{-\infty}^{\infty} (u+s)^n \rho_{\Gamma}(u) du ds.$$

Expanding the term $(u+s)^n$ [28] gives

$$\langle X^n \rangle = \sum_{k=0}^n \binom{n}{k} \int_{-\infty}^{\infty} s^k \rho_{\gamma}(s) ds \int_{-\infty}^{\infty} u^{n-k} \rho_{\Gamma}(u) du \\ \stackrel{(8),(9)}{=} \sum_{k=0}^n \binom{n}{k} \langle \gamma^k \rangle \langle \Gamma^{n-k} \rangle$$

in accordance with Eq. (10). ■

APPENDIX B: DERIVATION OF EQS. (11) AND (12)

In the first instance $\gamma(t)$ is confined to be strictly increasing. For an infinitesimally small interval $[x, x+dx]$

$$\rho_{\gamma}(x) dx = P\{x \leq \gamma(t) \leq x+dx\} \\ = P\{\gamma^{-1}(x) \leq t \leq \gamma^{-1}(x+dx)\}.$$

The probability is thus given by the length of the interval $[\gamma^{-1}(x), \gamma^{-1}(x+dx)]$ relative to the whole duration $\|I_t\|$ of the measurement.

$$\rho_{\gamma}(x) dx = \frac{|\gamma^{-1}(x+dx) - \gamma^{-1}(x)|}{\|I_t\|}. \quad (\text{B1})$$

Expanding $\gamma^{-1}(x+dx)$ around x

$$\gamma^{-1}(x+dx) = \gamma^{-1}(x) + \left[\frac{d}{ds} \gamma^{-1}(s) \right]_{s=x} dx$$

gives

$$\rho_{\gamma}(x) dx = \frac{1}{\|I_t\|} \left| \left[\frac{d}{ds} \gamma^{-1}(s) \right]_{s=x} \right| dx,$$

which is Eq. (11). ■

For general $\gamma(t)$ the sampling interval I_t is split up into K subintervals $I_t^{(k)}$ such that $\gamma(t)$ is monotone on each $I_t^{(k)}$; hence the inverse exists and is denoted as $\gamma_k^{-1}(x)$ for every $I_t^{(k)}$. Equation (B1) is then substituted by

$$\rho_{\gamma}(x) dx = \sum_{k:x \in I_t^{(k)}} \frac{|\gamma_k^{-1}(x+dx) - \gamma_k^{-1}(x)|}{\|I_t\|}.$$

Accordingly Eq. (12) is obtained. ■

APPENDIX C: PROOF OF EQ. (20)

The conditional probability density $\rho(\hat{x}, x | \tau)$ is considered in the limiting case $\tau \approx 0$.

$$\rho(\hat{x}, x | 0) \stackrel{(19)}{=} \frac{1}{\|I_t\|} \int_{I_t} \rho_{\Gamma}[x - \gamma(t)] \rho_{\Gamma}[\hat{x} - \gamma(t)] dt.$$

In the same way as in Appendix B the interval I_t is decomposed into K subintervals $I_t^{(k)} = [t_{k-1}, t_k]$ with time steps $t_0 < t_1 < \dots < t_{K-1} < t_K$ such that $\gamma(t)$ is monotone on each $I_t^{(k)}$. Thus

$$\rho(\hat{x}, x | 0) = \frac{1}{\|I_t\|} \sum_{k=1}^K \int_{t_{k-1}}^{t_k} \rho_{\Gamma}[x - \gamma(t)] \rho_{\Gamma}[\hat{x} - \gamma(t)] dt.$$

With $\gamma(t)$ being piecewise surjective the integration variable is changed from t to γ

$$\rho(\hat{x}, x | 0) = \sum_{k=1}^K \int_{\gamma(t_{k-1})}^{\gamma(t_k)} \rho_{\Gamma}(x - \gamma) \rho_{\Gamma}(\hat{x} - \gamma) \frac{1}{\|I_t\|} \frac{dt}{d\gamma} d\gamma \\ = \sum_{k=1}^K \int_{\gamma(I_t^{(k)})} \rho_{\Gamma}(x - \gamma) \rho_{\Gamma}(\hat{x} - \gamma) \frac{1}{\|I_t\|} \left| \frac{dt}{d\gamma} \right| d\gamma \\ = \int_{\gamma(I_t)} \rho_{\Gamma}(x - \gamma) \rho_{\Gamma}(\hat{x} - \gamma) \frac{1}{\|I_t\|} \sum_{k:\gamma \in I_t^{(k)}} \left| \frac{1}{(d\gamma/dt)} \right| d\gamma \\ = \int_{I_{\gamma}} \rho_{\Gamma}(x - \gamma) \rho_{\Gamma}(\hat{x} - \gamma) \\ \times \frac{1}{\|I_t\|} \sum_{k:\gamma \in I_t^{(k)}} \left| \left[\frac{d}{ds} \gamma_k^{-1}(s) \right]_{s=\gamma} \right| d\gamma \\ \stackrel{(12)}{=} \int_{I_{\gamma}} \rho_{\Gamma}(\hat{x} - \gamma) \rho_{\Gamma}(x - \gamma) \rho_{\gamma}(\gamma) d\gamma.$$

As above $\gamma_k^{-1}(x)$ denotes the inverse of $\gamma(t)$ on the subinterval $I_t^{(k)}$. ■

APPENDIX D: PROOF OF EQ. (23)

Assuming $\tau \approx 0$

$$\begin{aligned}
g(x) + x &= \frac{1}{\rho(x)} \int_{-\infty}^{+\infty} \hat{x} \rho(\hat{x}, x|0) d\hat{x} \\
&\stackrel{(20)}{=} \frac{1}{\rho(x)} \int_{-\infty}^{+\infty} \hat{x} \int_{I_\gamma} \rho_\Gamma(x - \gamma) \rho_\Gamma(\hat{x} - \gamma) \rho_\gamma(\gamma) d\gamma d\hat{x} \\
&= \frac{1}{\rho(x)} \int_{I_\gamma} \rho_\Gamma(x - \gamma) \rho_\gamma(\gamma) \int_{-\infty}^{+\infty} \hat{x} \rho_\Gamma(\hat{x} - \gamma) d\hat{x} d\gamma \\
&\stackrel{s := \hat{x} - \gamma}{=} \frac{1}{\rho(x)} \int_{I_\gamma} \rho_\Gamma(x - \gamma) \rho_\gamma(\gamma) \\
&\quad \times \left[\int_{-\infty}^{+\infty} s \rho_\Gamma(s) ds + \gamma \int_{-\infty}^{+\infty} \rho_\Gamma(s) ds \right] d\gamma \\
&\stackrel{(5)}{=} \int_{-\infty}^{+\infty} s \rho_\Gamma(s) ds + \frac{1}{\rho(x)} \int_{I_\gamma} \rho_\Gamma(x - \gamma) \rho_\gamma(\gamma) \gamma d\gamma,
\end{aligned}$$

which is Eq. (23). ■

APPENDIX E: $g(x)$ IN CASE OF A LINEAR TREND

The function $g(x)$ is calculated for $\gamma(t)$ as given in Eq. (29). Assuming symmetric $\rho_\Gamma(x)$

$$g(x) + x = \frac{1}{\rho(x)} \int_{I_\gamma} s \rho_\Gamma(x - s) \rho_\gamma(s) ds.$$

The denominator is

$$\begin{aligned}
\rho(x) &\stackrel{(5),(6)}{=} \int_{-\infty}^{\infty} \rho_\gamma(s) \rho_\Gamma(x - s) ds \\
&\stackrel{(30)}{=} \int_{-\infty}^{\infty} \frac{\|I_t\|}{\|I_\gamma\|} \delta[I_\gamma](x) \rho_\Gamma(x - s) ds \\
&= \frac{\|I_t\|}{\|I_\gamma\|} \int_{I_\gamma} \rho_\Gamma(x - s) ds.
\end{aligned}$$

The numerator is calculated as

$$\begin{aligned}
\int_{I_\gamma} s \rho_\Gamma(x - s) \rho_\gamma(s) ds &\stackrel{(30)}{=} \int_{I_\gamma} s \rho_\Gamma(x - s) \frac{\|I_t\|}{\|I_\gamma\|} \delta[I_\gamma](s) ds \\
&= \frac{\|I_t\|}{\|I_\gamma\|} \int_{I_\gamma} s \rho_\Gamma(x - s) ds.
\end{aligned}$$

Thus

$$g(x) = \frac{\int_{I_\gamma} s \rho_\Gamma(x - s) ds}{\int_{I_\gamma} \rho_\Gamma(x - s) ds} - x$$

as suggested in Eq. (31). ■

Substituting u for $x - s$ gives

$$g(x) = \frac{x \int_{I_u} \rho_\Gamma(u) du - \int_{I_u} u \rho_\Gamma(u) du}{\int_{I_u} \rho_\Gamma(u) du} - x = - \frac{\int_{I_u} u \rho_\Gamma(u) du}{\int_{I_u} \rho_\Gamma(u) du}$$

with $I_u = [x - \gamma_{\min}, x - \gamma_{\max}]$.

We now consider the special case, in which $\rho_\Gamma(x)$ is concentrated on some interval I_Γ in such way that $\rho_\Gamma(x) \approx 0$ if $x \notin I_\Gamma$. Then two limiting cases can be analyzed: First, if $I_\Gamma \subseteq I_u$,

$$g(x) \approx - \frac{\int_{I_\Gamma} u \rho_\Gamma(u) du}{\int_{I_\Gamma} \rho_\Gamma(u) du} = - \int_{I_\Gamma} u \rho_\Gamma(u) du$$

and vanishes due to the symmetry of $\rho_\Gamma(u)$. ■

Second, if $I_\Gamma \cap I_u = \emptyset$, l'Hospital's rule is used to approximate $g(x)$.

$$\begin{aligned}
g(x) &= - \frac{\frac{\partial}{\partial x} \int_{x - \gamma_{\max}}^{x - \gamma_{\min}} u \rho_\Gamma(u) du}{\frac{\partial}{\partial x} \int_{x - \gamma_{\max}}^{x - \gamma_{\min}} \rho_\Gamma(u) du} \\
&= - \frac{[u \rho_\Gamma(u)]_{u=x-\gamma_{\min}} - [u \rho_\Gamma(u)]_{u=x-\gamma_{\max}}}{[\rho_\Gamma(u)]_{u=x-\gamma_{\min}} - [\rho_\Gamma(u)]_{u=x-\gamma_{\max}}},
\end{aligned}$$

where the rule for differentiating a parameter integral [28] has been applied.

If $\rho_\Gamma(x - \gamma_{\min}) \gg \rho_\Gamma(x - \gamma_{\max})$ (e.g., for white noise and $x < \gamma_{\min}$), $g(x)$ is written as

$$g(x) = - \frac{(x - \gamma_{\min}) \rho_\Gamma(x - \gamma_{\min})}{\rho_\Gamma(x - \gamma_{\min})} = -x + \gamma_{\min}$$

and for $\rho_\Gamma(x - \gamma_{\min}) \ll \rho_\Gamma(x - \gamma_{\max})$

$$g(x) = -x + \gamma_{\max}.$$

Hence, if x is sufficiently far from I_γ , i.e., if $x \notin I_\gamma$ is such that the given requirements are fulfilled, then $g(x)$ converges to linear decrease with slope -1 . ■

- [1] H. Huikuri, K. Kessler, E. Terracall, A. Castellanos, M. Lin-naluoto, and R. Myerburg, Am. J. Cardiol. **65**, 391 (1990).
- [2] G. Panina, U. N. Khot, E. Nunziata, R. J. Cody, and P. F. Binkley, Am. Heart J. **129**, 748 (1995).
- [3] W. Nelson, Y. L. Tong, J. Lee, and F. Halberg, Chronobiologia **6**, 305 (1979).
- [4] J. Fernández and R. Hermida, Chronobiol Int. **15**, 191 (1998).
- [5] P. Langevin, C. R. Acad. Sci. **146**, 530 (1908).
- [6] K. Lindenberg and B. J. West, *The Nonequilibrium Statistical Mechanics of Open and Closed Systems* (VCH, New York, 1990).
- [7] R. Kubo, M. Toda, and N. Hashitsume, *Statistical Physics II. Nonequilibrium Statistical Mechanics*, Springer Series in Solid-State Sciences (Springer, Berlin, 1991).
- [8] N. G. van Kampen, *Stochastic Processes in Physics and Chemistry* (North-Holland, Amsterdam, 1992).
- [9] K. Itô, Nagoya Math. J. **1**, 35 (1950).
- [10] R. L. Stratonovich, SIAM J. Control **4**, 362 (1966).
- [11] M. Lax, Rev. Mod. Phys. **38**, 541 (1966).
- [12] R. Zwanzig, Phys. Rev. **124**, 983 (1961).
- [13] H. Mori, Prog. Theor. Phys. **33**, 423 (1965).
- [14] R. Kubo, Rep. Prog. Phys. **29**, 255 (1966).
- [15] R. F. Fox, J. Stat. Phys. **16**, 259 (1977).
- [16] S. Siegert, R. Friedrich, and J. Peinke, Phys. Lett. A **243**, 275 (1998).
- [17] R. Friedrich, S. Siegert, J. Peinke, S. Lück, M. Siefert, M. Lindemann, J. Raethjen, G. Deuschl, and G. Pfister, Phys. Lett. A **271**, 217 (2000).
- [18] J. Gradišek, I. Grabec, S. Siegert, and R. Friedrich, J. Sound Vib. **252**, 545 (2002).
- [19] J. Gradišek, E. Govekar, and I. Grabec, J. Sound Vib. **252**, 563 (2002).
- [20] T. Kuusela, T. Shepherd, and J. Hietarinta, Phys. Rev. E **67**, 061904 (2003).
- [21] T. Kuusela, Phys. Rev. E **69**, 031916 (2004).
- [22] F. Ghasemi, J. Peinke, M. Sahimi, and M. R. Rahimi Tabar, Eur. Phys. J. B **47**, 411 (2005).
- [23] C.-K. Peng, S. Havlin, H. E. Stanley, and A. L. Goldberger, Chaos **5**, 82 (1995).
- [24] P. Bernaola-Galván, P. C. Ivanov, L. A. Nunes Amaral, and H. E. Stanley, Phys. Rev. Lett. **87**, 168105 (2001).
- [25] F. Ghasemi, M. Sahimi, J. Peinke, and M. R. R. Tabar, J. Biol. Phys. **32**, 117 (2006).
- [26] H. Risken, *The Fokker-Planck Equation* (Springer, Berlin, 1989).
- [27] P. G. Hoel, S. C. Port, and C. J. Stone, *Introduction to Probability Theory* (Houghton Mifflin Company, Boston, 1971).
- [28] I. N. Bronshtein and Semendyayew, *Handbook of Mathematics* (Springer, Berlin, 1998).
- [29] R. Kleiger, J. Miller, J. Bigger, and A. Moss, Am. J. Cardiol. **59**, 256 (1987).
- [30] J. Nolan *et al.*, Circulation **98**, 1510 (1998).
- [31] P. Ponikowski *et al.*, Am. J. Cardiol. **79**, 1645 (1997).

See discussions, stats, and author profiles for this publication at: <https://www.researchgate.net/publication/6331402>

Stochastic Qualifiers of Epileptic Brain Dynamics

Article in *Physical Review Letters* · April 2007

DOI: 10.1103/PhysRevLett.98.138103 · Source: PubMed

CITATIONS

60

READS

103

2 authors, including:



Klaus Lehnertz

University of Bonn

346 PUBLICATIONS 16,907 CITATIONS

[SEE PROFILE](#)

Some of the authors of this publication are also working on these related projects:



seizure prediction [View project](#)



nonlinear time series analysis [View project](#)

Stochastic Qualifiers of Epileptic Brain Dynamics

Jens Prusseit^{1,2,*} and Klaus Lehnertz^{1,2,3,†}

¹Department of Epileptology, Neurophysics Group, University of Bonn, Sigmund-Freud-Strasse 25, D-53105 Bonn, Germany

²Helmholtz-Institute for Radiation and Nuclear Physics, University of Bonn, Nussallee 14-16, 53115 Bonn, Germany

³Interdisciplinary Center for Complex Systems, University of Bonn, Römerstrasse 164, 53117 Bonn, Germany

(Received 14 December 2006; published 28 March 2007)

We evaluate the capability of reconstructing Fokker-Planck equations for an improved characterization of electroencephalographic (EEG) recordings from epilepsy patients. We derive stochastic qualifiers of brain dynamics that are based on specific characteristics of the Kramers-Moyal coefficients estimated from the EEG. Analyzing long-lasting multichannel EEG recordings from eight patients suffering from focal epilepsies we show that particularly the stochastic part of the dynamics can yield valuable information for diagnostic purposes.

DOI: 10.1103/PhysRevLett.98.138103

PACS numbers: 87.19.La, 05.10.Gg

The dynamics of many natural and man-made complex systems exhibits deterministic and stochastic features. In situations where the underlying equations of motion are not known, a detailed quantitative description can nevertheless be achieved by applying time series analysis techniques to experimentally acquired observables. When the dynamics involves only a few degrees of freedom the framework of nonlinear time series analysis [1,2] provides quite powerful tools to characterize complex behavior, which allows one to estimate the underlying equations of motion from time series data. Over the past decades analyses of electroencephalographic (EEG) time series have provided valuable insight into the complex spatiotemporal dynamics of physiological and pathophysiological brain functions [3]. In epileptology, particularly nonlinear approaches were shown to allow an improved understanding of intermittent dysfunctioning of the brain between epileptic seizures and to provide potentially useful diagnostic information [4]. Moreover, these techniques provided first evidence for the existence of seizure precursors whose unequivocal detection might lead to the development of seizure prediction and prevention techniques [5]. Despite the many promising findings there are a number of problems for which there are currently no satisfactory solutions. This can be attributed to the fact that in many cases crucial aspects of pathological brain dynamics must be regarded as stochastic (high-dimensional) and thus, may not be captured when applying time series analysis techniques that preferentially focus on the low-dimensional deterministic part of the dynamics.

Dissipative dynamical systems under the influence of noise can often be successfully modeled by a Fokker-Planck or, equivalently, an associated Langevin equation [6,7], which reads $\dot{x} = D^{(1)}(x(t)) + \sqrt{D^{(2)}(x(t))}\Gamma(t)$ in the one-dimensional case. $x(t)$ denotes the state of the system and $\Gamma(t)$ is a Gaussian white noise process which is assumed to be uncorrelated, $\langle \Gamma(t)\Gamma(t') \rangle = \delta(t-t')$, with vanishing mean, $\langle \Gamma(t) \rangle = 0$. The drift coefficient $D^{(1)}$ de-

scribes the deterministic part of the dynamics and the diffusion coefficient $D^{(2)}$ determines the strength of the driving noise force. If $D^{(2)}$ depends on the state x the stochastic part is referred to as multiplicative dynamical noise, otherwise as additive dynamical noise. The Fokker-Planck equation is a special case of a more general evolution equation for continuous Markov processes, namely, the Kramers-Moyal expansion, and the coefficients $D^{(n)}$ can be defined in a statistical sense using the conditional moments of the stochastic variable $X(t)$ [8]:

$$D^{(n)}(x, t) = \frac{1}{n!} \lim_{\tau \rightarrow 0} \frac{1}{\tau} \langle [X(t + \tau) - X(t)]^n \rangle|_{X(t)=x}. \quad (1)$$

In Refs. [9–11] an analysis technique has been introduced that allows one to estimate drift and diffusion coefficients from time series data by evaluating the conditional moments in Eq. (1) for finite time steps τ and then extrapolate to $\tau = 0$. This technique has been successfully applied in a variety of disciplines ranging from physics [12–18] to the biomedical domain [19–21].

In this Letter we show that, by using this approach, an improved characterization of pathological brain dynamics can be achieved by explicitly taking into account stochastic parts of the dynamics. We retrospectively analyzed multichannel (20–60 recording sites), multiday (5–12 days) EEG recordings from eight patients with pharmacoresistant focal epilepsy who underwent evaluation for resective therapy. EEG data were recorded from the cortex and from within relevant structures of the brain, hence with a high signal-to-noise ratio. Signals were sampled at 200 Hz using a 16 bit analog-to-digital converter and filtered within a frequency band of 0.53 to 85 Hz. After surgery all patients achieved complete seizure control so the brain structure responsible for seizure generation (epileptic focus) can be assumed to be contained within the resected brain volume.

The method proposed in Refs. [9–11] requires the brain dynamics to be Markovian (a process without memory), which we checked by evaluating the Chapman-

Kolmogorov equation for the conditional probabilities $p(x(t+2\tau)|x(t))$ [8]:

$$\begin{aligned} p(x(t+2\tau)|x(t)) = & \int dx(t+\tau)p(x(t+2\tau)|x(t+\tau)) \\ & + p(x(t+\tau)|x(t)). \end{aligned} \quad (2)$$

We analyzed exemplary EEG time series recorded from within the epileptic focus and from a distant brain region during the seizure-free interval of one patient. For epoch lengths ranging from about 2 to 8 min we observed that Eq. (2) is approximately fulfilled for a minimum possible time shift $\tau = 1$ (in units of the sampling interval) [22]. In Fig. 1 we show typical examples of drift and diffusion coefficients estimated from EEG time series. Both coefficients can be well approximated by low order polynomials. As expected for this one-dimensional model $D^{(1)}$ indicates an overall linear damping behavior. For EEG time series recorded from within the epileptic focus we observed small nonlinearities toward higher amplitude values, which is in line with findings from studies using nonlinear time series analysis techniques [4]. The behavior of $D^{(2)}$ indicates a multiplicative influence of the noise. To test whether the deviation from an additive behavior (i.e., $D^{(2)} = \text{const.}$) was caused by the finiteness of the time shift τ [23] we followed Refs. [24,25] and considered a Taylor expansion of the second conditional moment. Using the estimated values of $D^{(1)}$ and different constant diffusion coefficients

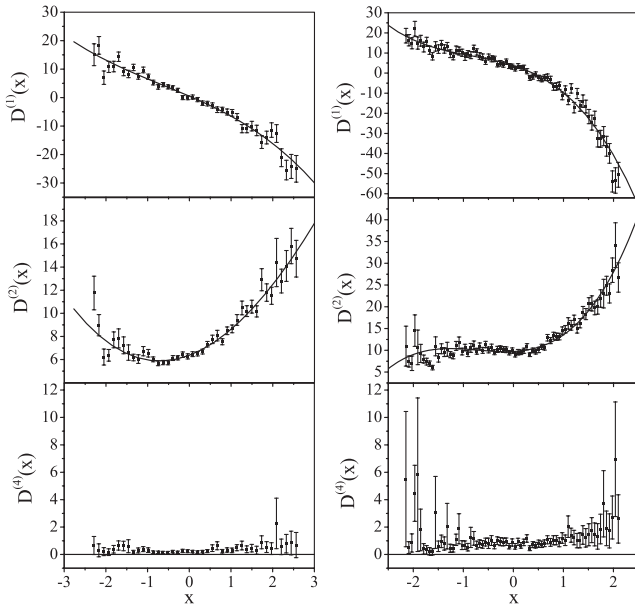


FIG. 1. Estimated coefficients $D^{(1)}$, $D^{(2)}$, and $D^{(4)}$ for exemplary EEG time series (left: from a distant brain region; right: from within the epileptic focus). Shown are estimates for time series consisting of 100 000 data points (squares) as well as fits with low order polynomials (black lines). Error bars indicate the statistical error of the estimation of the averages according to Eq. (1) for each value of x .

we observed that the influence of higher order terms in τ cannot explain the multiplicativity of the estimated second coefficients.

We also estimated the fourth-order coefficient $D^{(4)}$, which allows one to determine whether the driving noise process $\Gamma(t)$ exhibits deviations from a Gaussian distribution [26]. Only if $D^{(4)}$ vanishes, $\Gamma(t)$ is Gaussian and the probability density function (PDF) of the process under consideration evolves according to a Fokker-Planck equation [27]. For the EEG recorded from a distant brain region

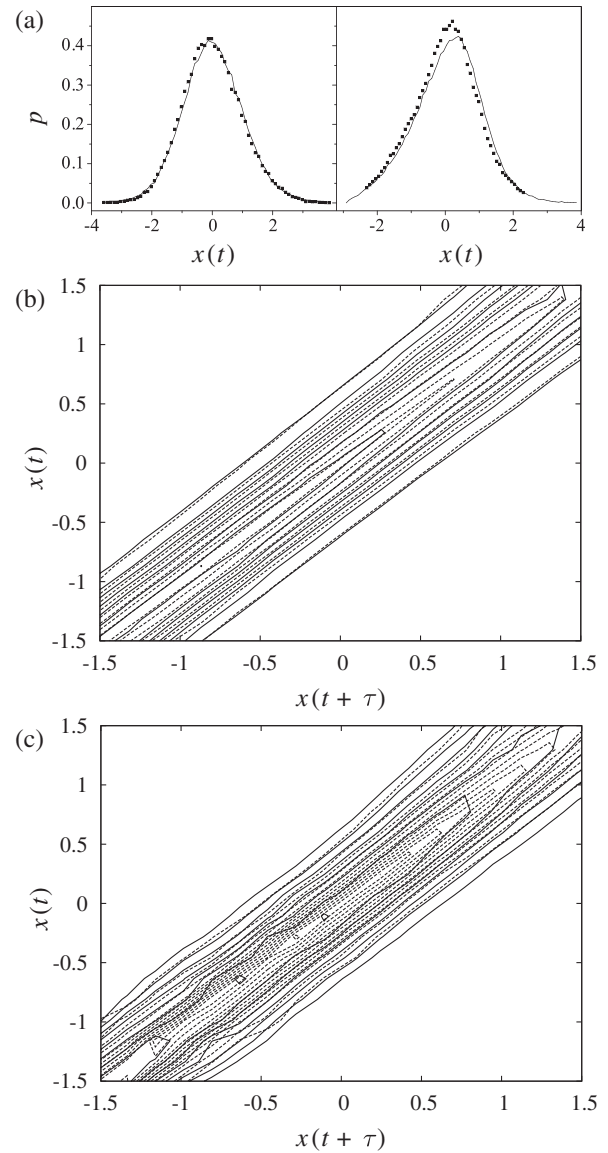


FIG. 2. Comparison of the stationary PDF's (a) and contour plots of conditional PDF's for $\tau = 1$ (b) and (c) for the EEG time series [squares in (a), dashed lines in (b) and (c)] and time series generated by integrating the associated Langevin equations (straight lines). (a) left plot and (b): from a distant brain region; (a) right plot and (c): from within the epileptic focus. Contour plots were generated using an increment between contour lines of 0.02 in (b) and 0.012 in (c).

$D^{(4)}$ took on values slightly above zero but the magnitude of this coefficient was less than one-twentieth in comparison to the second coefficient $D^{(2)}$. In contrast, for the EEG recorded from within the epileptic focus $D^{(4)}$ took on values clearly above zero. These findings indicate that a description of pathological brain dynamics by a one-dimensional Fokker-Planck model may be inadequate. This is further corroborated by our results obtained from integrating the Langevin equation [29,30] using the estimated functions $D^{(1)}$ and $D^{(2)}$ for both EEG time series (Fig. 2). While both the stationary and the conditional PDF's of the integrated model and of the EEG time series coincided quite well for the recording from a distant brain region, we observed more pronounced deviations for the recording from within the epileptic focus.

These findings clearly indicate that specific characteristics of the estimated drift and diffusion coefficients allow one to differentiate between physiological and pathophysiological activities. For this purpose we derived different quantities from the estimated coefficients that serve as *stochastic qualifiers* of epileptic brain dynamics [22]. As an example, we here consider the range covered by the values of the estimated coefficients $R_{1,2} := |\max(D^{(1,2)}(x)) - \min(D^{(1,2)}(x))|$. We here only took into account values of $D^{(1,2)}$ for which at least 100 data points were available for the estimation procedure. For the multichannel, multiday EEG recordings from all patients we performed a time resolved estimation of $R_{1,2}$ using a

moving-window technique. Data windows were of size $N = 50\,000$ data points, and windows overlapped by 50%. This choice represents a compromise between sufficient statistics for a reliable estimation of $D^{(1,2)}$ and temporal resolution, which might be of interest for further EEG analyses. We stress that the determination of $R_{1,2}$ was done fully automatically and without human interference.

In Fig. 3(a) we show a typical spatiotemporal distribution of R_2 calculated for a multichannel EEG (52 contacts) recorded during the seizure-free interval from a patient with an epileptic focus located in the right hemisphere. When comparing findings from the left and right brain hemisphere we observed highest values of R_2 confined to regions close to or within the epileptic focus. We thus expected that pathophysiological activities are reflected by increased values of our measures.

Since these values showed only little variance over time we calculated, for each contact, their temporal average, $\langle R_{1,2} \rangle_t$, and eventually averaged over all contacts c from each hemisphere ($\tilde{R}_{1,2} := \langle \langle R_{1,2} \rangle_t \rangle_c$). This allowed us to further condense the information contained in the spatiotemporal distribution of our stochastic qualifiers and to investigate retrospectively whether they can provide diagnostically relevant information. In the following we refer to the brain hemisphere containing the epileptogenic focus (determined by the presurgical workup and by the postoperative complete seizure control) as the *focal side*, whereas the opposite hemisphere is denoted as the *non-focal side*. In six out of eight patients \tilde{R}_1 was higher on the

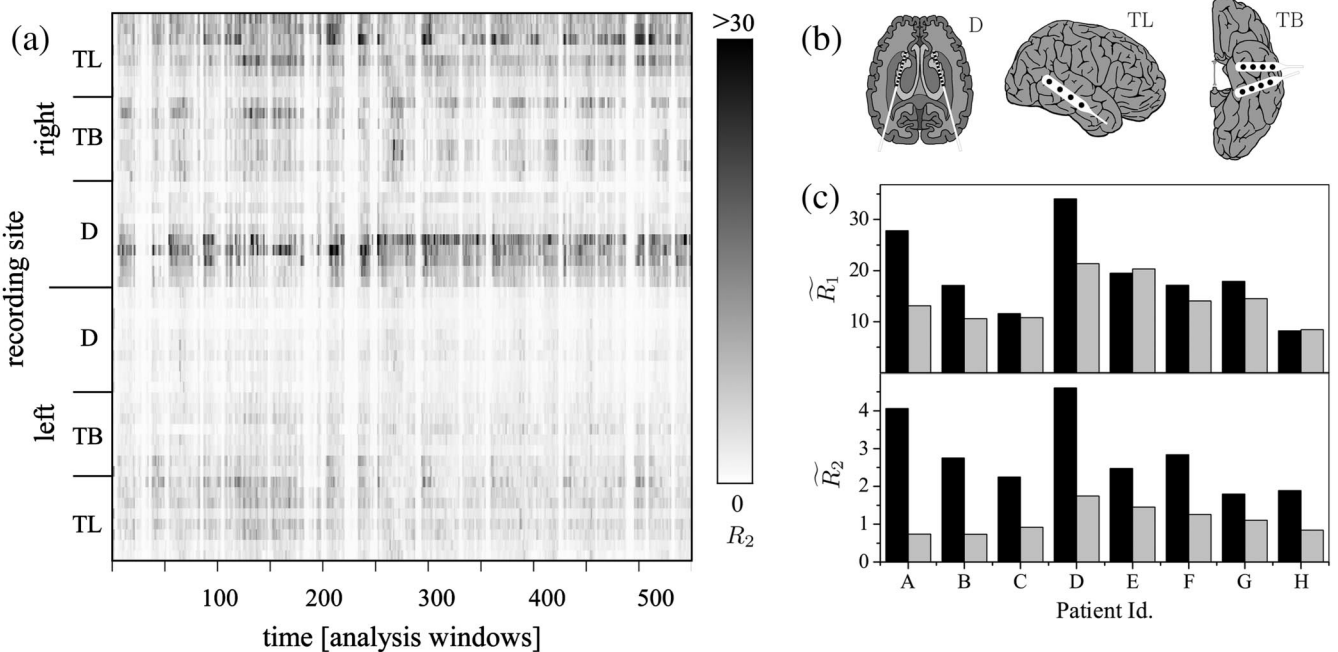


FIG. 3. (a) Time resolved estimates of R_2 calculated from a multichannel EEG recording (approximately 19 h) of a patient suffering from a right-sided focal epilepsy (patient F). (b) Implantation scheme of intracranial electrodes: hippocampal depth electrodes (10 contacts each, D), lateral (4–16 contacts, TL), and basal (4 contacts each, TB) strip electrodes. (c) Spatiotemporal means of R_1 and R_2 for all investigated patients. Black bars denote values from the focal and gray bars from the nonfocal hemisphere.

focal side. Interestingly, we observed that \tilde{R}_2 allowed correct identification of the focal side in *all* patients [Fig. 3(c)].

To conclude, we have investigated the applicability of a time series analysis method that is based on the reconstruction of a Fokker-Planck equation from empirical data for an improved characterization of epileptic brain dynamics. For this purpose we studied long-lasting, multichannel EEG time series that covered physiological and pathophysiological activities from the seizure-free interval of eight patients suffering from focal epilepsies. Despite limitations that can be attributed to the fact that EEG time series may not entirely meet the prerequisites of the underlying theoretical framework, a one-dimensional Fokker-Planck model appeared to be appropriate for a description of physiological activities. It may not be possible, however, to capture all aspects of pathophysiological activities in such a model. Nevertheless, we were able to derive stochastic qualifiers that allowed a more comprehensive characterization of the epileptic process particularly when focusing on the stochastic part of the dynamics. Thus, even in cases where the dynamics is not generated by a Langevin process but by a more complex process for which the Markovian property is not fulfilled in a strict sense, drift and diffusion coefficients appear to be quite useful characterizing quantities [31]. We expect that our approach along with further improvements can yield valuable information for diagnostic purposes and can advance our understanding of the complicated dynamical system epileptic brain.

We are grateful to Joachim Peinke and Christian E. Elger for useful discussions and valuable comments. K. L. acknowledges support from the Deutsche Forschungsgemeinschaft (Grant No. SFB-TR3 subproject A2).

*Electronic address: jprusseit@gmx.de

[†]Electronic address: klaus.lehnertz@ukb.uni-bonn.de

- [1] H. Kantz and T. Schreiber, *Nonlinear Time Series Analysis* (Cambridge University Press, Cambridge, U.K., 2003).
- [2] H. D. I. Abarbanel, *Analysis of Observed Chaotic Data* (Springer-Verlag, New York, Berlin, Heidelberg, 1996).
- [3] C. J. Stam, Clin. Neurophysiol. **116**, 2266 (2005).
- [4] R. G. Andrzejak, F. Mormann, G. Widman, T. Kreuz, C. E. Elger, and K. Lehnertz, Epilepsy Res. **69**, 30 (2006).
- [5] F. Mormann, R. G. Andrzejak, C. E. Elger, and K. Lehnertz, Brain **130**, 314 (2007).
- [6] P. Hänggi and H. Thomas, Phys. Rep. **88**, 207 (1982).
- [7] N. G. van Kampen, *Stochastic Processes in Physics and Chemistry* (North-Holland Publishing Company, Amsterdam, 1981).
- [8] H. Risken, *The Fokker-Planck Equation* (Springer, Berlin, 1989), 2nd ed.
- [9] R. Friedrich and J. Peinke, Phys. Rev. Lett. **78**, 863 (1997).
- [10] S. Siegert, R. Friedrich, and J. Peinke, Phys. Lett. A **243**, 275 (1998).
- [11] R. Friedrich, S. Siegert, J. Peinke, S. Lück, M. Siefert, M. Lindemann, J. Raethjen, G. Deuschl, and G. Pfister, Phys. Lett. A **271**, 217 (2000).
- [12] St. Lück, J. Peinke, and R. Friedrich, Phys. Rev. Lett. **83**, 5495 (1999).
- [13] C. Renner, J. Peinke, and R. Friedrich, J. Fluid Mech. **433**, 383 (2001).
- [14] H. U. Bödeker, M. C. Röttger, A. W. Liehr, T. D. Frank, R. Friedrich, and H.-G. Purwins, Phys. Rev. E **67**, 056220 (2003).
- [15] M. Waechter, F. Riess, H. Kantz, and J. Peinke, Europhys. Lett. **64**, 579 (2003).
- [16] G. R. Jafari, S. M. Fazeli, F. Ghasemi, S. M. Vaez Allaei, M. Reza Rahimi Tabar, A. Iraji zad, and G. Kavei, Phys. Rev. Lett. **91**, 226101 (2003).
- [17] T. D. Frank, P. J. Beek, and R. Friedrich, Phys. Lett. A **328**, 219 (2004).
- [18] J. Gradisek, S. Siegert, R. Friedrich, and I. Grabec, Phys. Rev. E **62**, 3146 (2000).
- [19] T. Kuusela, T. Shepherd, and J. Hietarinta, Phys. Rev. E **67**, 061904 (2003).
- [20] T. Kuusela, Phys. Rev. E **69**, 031916 (2004).
- [21] A. M. van Mourik, A. Daffertshofer, and P. J. Beek, Biol. Cybern. **94**, 233 (2006).
- [22] J. Prusseit and K. Lehnertz (to be published).
- [23] M. Ragwitz and H. Kantz, Phys. Rev. Lett. **87**, 254501 (2001).
- [24] R. Friedrich, C. Renner, M. Siefert, and J. Peinke, Phys. Rev. Lett. **89**, 149401 (2002).
- [25] P. Sura and J. Barsugli, Phys. Lett. A **305**, 304 (2002).
- [26] R. F. Pawula, Phys. Rev. **162**, 186 (1967).
- [27] A Langevin equation driven by a Gaussian noise force can generate a process with non-Gaussian PDFs [8]. Apart from the Fokker-Planck equation (see, e.g., [13]) there are other approaches for a description of such processes (see, e.g., [28], and references therein).
- [28] S. Jung and H. L. Swinney, Phys. Rev. E **72**, 026304 (2005).
- [29] P. E. Kloeden and E. Platen, *Numerical Solution of Stochastic Differential Equations* (Springer, Berlin, 1999).
- [30] R. L. Stratonovich, J. SIAM Control **4**, 362 (1966).
- [31] T. Stemler, J. P. Werner, H. Benner, and W. Just, Phys. Rev. Lett. **98**, 044102 (2007).

2

Methodological Aspects of Heart Rate Variability Analysis

Tom Kuusela

CONTENTS

| | | |
|---------|--|----|
| 2.1 | Introduction | 10 |
| 2.2 | ECG Recording and Generation of RR Interval | 11 |
| 2.2.1 | RR Interval Time Series | 11 |
| 2.2.2 | Time and Amplitude Resolution of ECG Recording | 11 |
| 2.2.3 | Duration of the Recording | 11 |
| 2.2.4 | Stationarity of the Recording | 12 |
| 2.2.5 | Removing Trends | 12 |
| 2.2.6 | Ectopic Beats, Arrhythmias and Noise | 13 |
| 2.3 | Time Domain Analysis | 13 |
| 2.4 | Frequency Domain Analysis | 14 |
| 2.4.1 | Fourier Transform | 14 |
| 2.4.1.1 | Data Windowing | 15 |
| 2.4.1.2 | FFT Algorithm | 16 |
| 2.4.2 | Autoregressive Modeling | 16 |
| 2.4.2.1 | Model Order | 17 |
| 2.4.3 | Resampling | 17 |
| 2.4.4 | Spectral Powers | 18 |
| 2.4.6 | Effects of Respiration | 20 |
| 2.4.7 | Time–Frequency Analysis | 21 |
| 2.4.7.1 | Windowed Fourier Transform | 21 |
| 2.4.7.2 | Wigner–Ville Distribution | 23 |
| 2.4.7.3 | Complex Demodulation | 23 |
| 2.4.7.4 | Other Methods | 25 |
| 2.5 | Non-Linear Analysis | 26 |
| 2.5.1 | Approximate Entropy and Sample Entropy | 26 |
| 2.5.2 | Scaling Exponents | 30 |
| 2.5.2.1 | Detrended Fluctuation Analysis | 30 |
| 2.5.2.2 | Spectrum Power Law Exponent | 32 |
| 2.5.3 | Fractal Dimensions | 32 |
| 2.5.3.1 | Correlation Dimension | 32 |
| 2.5.3.2 | Pointwise Correlation Dimension | 33 |
| 2.5.3.3 | Dispersion Analysis | 33 |

| | | |
|---------|----------------------------|----|
| 2.5.4 | Return Map..... | 34 |
| 2.5.5 | Other Approaches..... | 36 |
| 2.5.5.1 | Stationarity Test..... | 36 |
| 2.5.5.2 | Symbolic Dynamics | 36 |
| 2.5.5.3 | Multifractal Analysis..... | 37 |
| 2.5.5.4 | Stochastic Modeling | 38 |
| 2.6 | Conclusions..... | 38 |
| | Abbreviations | 39 |
| | References..... | 40 |

2.1 Introduction

There are numerous methods and approaches available for time-series analysis. This chapter presents selected methods, which are or at least could be useful when analyzing biosignals, especially heart rate variability (HRV). The methods described here differ greatly, and some of them are commonly used characterization methods. One must always select the method to use, case by case.

The analysis methods are often divided into *linear* and *non-linear* methods. The term “non-linear methods” is in fact not quite appropriate and is actually even misleading, because those methods themselves are no more non-linear than common spectrum analysis using fast Fourier transform (FFT) algorithm. The idea behind the naming convention is merely related to the fact that the system producing the time series is non-linear, which in the case of biological systems might well be true. Sometimes these methods are described using the term *chaos-theoretical approach*. This is true only of some of the methods in which the assumption that the system’s trajectory in a phase space is actually a chaotic small-dimensional attractor. There is very little proof for the existence of this in biological systems. In particular, if we are studying the cardiovascular blood pressure regulatory system and typical time series such as the sequence of RR intervals, we can find in the literature a growing number of results that indicate this system to be stochastic rather than chaotic.

Biosignal time series, in general, are very difficult to analyze, in many ways. Many methods demand that the time series has thousands of data points, which may be impossible or difficult to achieve, depending on the measurement method used. When the time series is long, notable changes in the biological system will occur almost inevitably and the time series will start to drift in the parameter space of the system due to either internal or external influences. Such instability has a negative effect on all analysis methods in which a specific characteristic of the whole time series is to be compressed into a single statistic. Of course, calculations will produce some result, but what is the meaning of the statistic? Other disturbing factors in these signals are notable noise levels, strong discreteness of the signals due to a limited amplitude resolution of the digitization and regular strong periodic signals, for example, breathing modulation on top of the otherwise possibly chaotic or stochastic signal. It should be remembered that most of the methods described in this chapter were originally developed in physics for analyzing very different, and often practically ideal systems.

Despite warnings stated earlier, an analysis of biosignals using such methods may still yield useful information. Even though the calculated statistic might not exactly

describe the characteristic it was originally designed to represent, it could still play an important role when searching for a correlation with other clinically interesting parameters. However, basic assumptions and limitations accompanying each method should be clearly understood when interpreting results and searching different explanatory models.

2.2 ECG Recording and Generation of RR Interval

2.2.1 RR Interval Time Series

HRV analysis is based on the RR interval time series, the sequence of intervals between successive fiducial points of R peaks of QRS complexes in the electrocardiogram (ECG). It should be noted that the RR interval time series are actually an event series and not an equally sampled continuous signal. This fact is important, especially when performing frequency domain analysis. It should also be noted that HRV analysis does not measure the rhythms of the sinoatrial node, which is the pacemaker of the heart, since it is not based on P-P intervals. Therefore, HRV reflects fluctuations in the atrioventricular conduction superimposed on the P-P interval. Nevertheless, it has been shown that beat-to-beat changes in RR intervals reflect the variability of the sinoatrial node quite accurately. In theory, it would be better to use P-P intervals for HRV analysis, but in practice, the amplitude of the P wave is small, which makes the accurate determination of P wave peak difficult, especially in the presence of noise. In turn, this would affect the accuracy of P-P interval measurement.

2.2.2 Time and Amplitude Resolution of ECG Recording

The sampling frequency and amplitude resolution of ECG recording are important parameters in HRV analysis. The sampling frequency determines the temporal resolution of R peak recognition of QRS complexes, and, therefore, it determines directly the accuracy of the measurement of RR intervals. Too low a sampling rate produces digitization noise and introduces errors in all HRV measures, whether in time and frequency domains or in non-linear analyses. In most cases, a sampling rate of 200 Hz corresponding to a temporal resolution of 5 ms is high enough, and higher sampling rates do not give any better results. If the overall variability of RR interval is very low, as it can be, for example, with some heart failure patients, HRV analysis requires a higher sampling rate, since changes in the length of RR intervals cannot be captured below that resolution.

The amplitude resolution of the analog–digital conversion of ECG signal is rarely a limiting factor. The commonly used resolution of 12 bits is normally sufficient. However, the effective amplitude resolution is always less than the resolution of the conversion because the full dynamic range of input signal in the converter is rarely utilized in order to avoid signal clipping or saturation in the case of a large ECG signal or a wandering baseline.

2.2.3 Duration of the Recording

The duration of the recording is determined by the method used for HRV analysis, the aim of the study, and stationarity issues. Typically, frequency domain methods are preferred

for short-term measurements and time domain methods for long-term measurements of HRV. Some non-linear methods are likewise suitable for short-term analyses and others for long-term analyses. It is important to note that although the same mathematical method is used for the analysis of both short-term and long-term ECG recordings, the physiological interpretation can be different, that is, they cannot necessarily be considered as the surrogates for each other just with a different duration. There are also non-linear methods where results depend directly on the number of data points, and thus, it is inappropriate to compare the HRV measures obtained from recordings of different durations, with each other. This is also true of most linear methods.

2.2.4 Stationarity of the Recording

The stationarity of the signal is of great importance. There are many methods available for evaluating the stationarity of a signal, depending on how we define stationarity. Stationarity can mean, for instance, that there is no shifting in the base level of the signal or that the amplitude distribution, spectrum and autocorrelation function of the signal do not change, as a function of time. More generally, we can say that a signal is truly stationary if parameters that define the working point of the system remain constant in time. This evaluation is extremely difficult to undertake in the case of physiological systems, since we have a limited knowledge of the background dynamics and most physiological parameters are unknown.

Stationarity is strongly linked to the duration of the recording. The longer a recording is, the less stationary it is, because inevitably there are changes in the physiological state of the subject. Whatever method is used for the analysis of long recordings, the result is always a complicated and often a non-intuitive average over physiological states. Unless the method is designed for such a situation (e.g., see DFA), this kind of analysis should be avoided. Hence, the best approach is to divide the recording into shorter segments and perform separate analyses on them. This confers several advantages: shorter segments are often more stationary and results more reliable; the temporal change of results is a measure of stationarity (or lack thereof), which can be used to investigate the time evolution of the system; and finally, changes over segments can be utilized when estimating the statistical relevance of the results. The last advantage is most useful because normally we get a single statistical estimate as a result, but have no possibilities to quantify the statistical significance of this number.

2.2.5 Removing Trends

Most non-stationarities of the signal are not evident until they are revealed by a more advanced analysis. The trend in RR interval time series is easily seen, and it is often interpreted as a sign of non-stationarity, which can be removed by subtracting the trend from the data. However, *a priori* there is no way to separate the “real” signal and its trend; the signal is *never* a sum of them. In theory, even large trends can be an essential part of the dynamical behavior of a stationary system. But in practice, many HRV analysis methods are useful only if there is no significant trend in the data irrespective of its origin and in these circumstances, the trend should be removed from the data. Normally, only the linear trend is removed, since the removal of non-linear trends may create a significant bias. From the point of view of spectral analysis, the trend removal decreases the contribution of the

lowest frequencies; thus, further analysis is focused on faster oscillations. And finally, it must be remembered that the removal of a trend does not restore the stationarity of data. The only way to overcome the problem of non-stationarity is to minimize all internal and external disturbances during the study.

2.2.6 Ectopic Beats, Arrhythmias and Noise

The ECG signal can contain technical artifacts or QRS complexes originating outside the sinoatrial node, which introduce errors, since HRV analysis is based on assessment of the variability of sinus rhythm. Artifacts can seriously affect HRV analysis and thus cannot be ignored.

Technical artifacts, such as missed beats (due to problems in the R peak detection) or electrical noise (bad contact in the electrode, movement artifacts), can be easily edited by cleaning the data by a proper interpolation based on the preceding and successive QRS intervals. When interpolating the RR interval time series, it is important that the cumulative time is not altered; RR interval is an event series where the time stamp of each beat is the sum of all preceding beats. For example, the respiratory modulation on RR interval encounters a small phase shift if the time line changes after an interpolated segment. Similarly, time synchronization with other signals should be preserved.

The editing of ectopic beats is more problematic. Ectopic beats are usually premature beats and they produce a very short RR interval followed by a compensatory delay and a prolonged RR interval. Such a short-long pair can be edited without affecting the cumulative time of the beats by lengthening the first interval and shortening the second interval, so that they have equal intervals. However, ectopic beats and most arrhythmias result in reduced stroke volume and cardiac output, leading to transient drops in the blood pressure. This activates autonomic reflexes and induces changes in the efferent autonomic activity. Since these true physiological responses can last 10–30 beats, editing of just the two intervals on either side of ectopic beats does not remove all of the changes in HRV produced by them.

The raw recorded ECG signal should always be inspected. QRS complex identification should be carefully verified. If there are any artifacts or ectopic beats present, the best option is to select a signal segment free of them. If an artifact-free recording is not available, editing can be considered. If an excessive editing of ectopic beats is needed, it should be recognized that HRV analysis can then lead to erroneous results. Very few analysis methods are so insensitive to ectopic beats that the ECG needs no editing at all.

2.3 Time Domain Analysis

The most common time domain estimate of HRV is the standard deviation of RR intervals (SDNN; normal-to-normal deviation of intervals measured between consecutive sinus beats). SDNN can be calculated, for instance, over 5 min segments (called SDANN) or over 24 h. These two estimates should not be compared because HRV is not a stationary process, that is, a process in which the mean and the variance are independent of the record

length. In long-term recordings, the low-frequency (LF) variations contribute a major proportion of the overall HRV power and also to the SDNN. Since HRV normally decreases at higher levels of the heart rate, SDNN can be normalized against this effect by dividing it by the mean RR interval.

Some commonly used HRV measures are based on the differences between RR intervals, such as the root mean square of successive differences of RR intervals (RMSSD), the number of pairs of adjacent RR intervals differing by more than 50 ms (NN50 count) and the ratio of NN50 count to the count of all RR intervals expressed as a percentage (pNN50). Since all of these measures use RR interval differences, they reflect mainly high-frequency (HF) variations of heart rate and are almost independent of long-term trends. Furthermore, these measures are highly correlated with each other and can thus be considered as surrogates of each other.

All time domain HRV estimates are easily calculated; they do not need time-consuming computation. Also, they do not require stationarity in the same manner as most frequency domain and non-linear analyses do. The main limitation of time domain methods is their lack of discrimination between effects of sympathetic and parasympathetic autonomic branches.

2.4 Frequency Domain Analysis

The main idea behind the frequency domain analysis of HRV is the observation that HRV is composed of certain well-defined rhythms, which are related to different regulatory mechanisms of cardiovascular control. Time domain HRV measures are mainly markers of overall HRV, although some of them can contain information about heart rate oscillations in certain frequency bands (e.g., RMSSD mainly quantifies fast changes in RR intervals). In order to get more detailed information on the dynamics and frequency components of HRV, more advanced analysis methods, such as power spectral density (PSD) analysis, have to be applied. PSD analysis decomposes the signal into its frequency components and quantifies their relative (and also absolute) intensity, named *power*. In other words, it provides estimates of the PSD function of the heart rate, namely, the distribution of frequency components. There are two commonly used methods to compute the PSD function: Fourier transform and autoregressive (AR) modeling.

2.4.1 Fourier Transform

The Fourier transform can be used to convert the time domain data into the frequency domain data and back. The Fourier transform is a one-to-one transform, that is, no information is lost or added; the data just has two different *representations* (Marple, 1987). The normal Fourier transform is defined for continuous functions over the whole real axis. In the case of RR interval time series, the original Fourier transform must be replaced with the discrete version of the transform. The discrete Fourier transform has some unique features which one should be mindful of when using it.

For the equally sampled time series $x(t_k)$, where $t_k = k\Delta$ is the time moment of the data sample, Δ is the sampling interval (the inverse of the sampling rate; see comments below

on the resampling of time series) and $k = 0, 1, 2, \dots, N-1$, the discrete Fourier transform $X(f_n)$ is

$$X(f_n) = \Delta \sum_{k=0}^{N-1} x(t_k) e^{-2\pi i f_n t_k} = \Delta \sum_{k=0}^{N-1} x(t_k) e^{-2\pi i k n / N}, \text{ where } f_n = \frac{n}{N\Delta}. \quad (2.1)$$

When the time series $x(t_k)$ consists of real values, as it is in our case, $n = 0, \dots, N/2$. The discrete Fourier transform (Equation 2.1) gives us $N/2$ *complex numbers* (real and imaginary parts*), thus there is an equal number of data points in $x(t_k)$, and $X(f_n)$ since the first and last $X(f_n)$ has only the real part. The power spectral density is $\text{PSD}(f_n) = |X(f_n)|^2$ corresponding to the *squared amplitude* of the frequency component f_n .

The discrete Fourier transform (Equation 2.1) has several important features. First, the frequency scale is discrete, since only f_n components are possible. The *resolution* of frequency scale depends inversely on the number of data samples N and the sampling interval Δ . The highest-frequency component ($n = N/2$), called the Nyquist critical frequency, is $f_c = 1/(2\Delta)$. If the time series $x(t_k)$ is a pure sine wave of a frequency exactly equal to one of the frequencies f_n , only $X(f_n)$ is non-zero, as we can expect. However, if the frequency f of the oscillation is between two adjacent f_n 's, there are many non-zero spectral components $X(f_n)$ around f . This is called leakage from one frequency to another in the power spectral estimate, and it is characteristic only of the discrete Fourier transform. This problem can be partially overcome by using *data windowing*.

2.4.1.1 Data Windowing

The discrete Fourier transform (Equation 2.1) can be interpreted as a Fourier transform of the product of the infinitely long time series with a square window function, which turns on at $t = 0$ and off at $t = (N-1)\Delta$. Because of this rapid switching, its Fourier transform has substantial components at higher frequencies, causing the leakage from one frequency to another. To remedy this situation, we can multiply the time series by a window function that changes more gradually from zero to maximum (in the middle of the time series) and then back to zero. There are numerous window functions (named *Welch*, *Parzen*, *Hanning* and so on), but for the purpose of HRV analysis, there is effectively little or no difference between any of them.[†]

Smoothing

The statistical reliability of the PSD is very low. In fact, the standard deviation (SD) of the PSD estimate is always 100% of the value, and it is independent of N , that is, we cannot get more precise estimates by increasing the number of data points; we just get more discrete frequencies f_n . This means that the amplitude of each spectral component is always unreliable from a statistical point of view. Luckily, in HRV analysis, we are not interested in the amplitude of some specific frequency component but in the spectral power over a certain frequency range. If we want to look at the details of the PSD, the

* Complex number $X(f_n)$ can be interpreted as a two-dimensional vector. Each $X(f_n)$ carries information on the amplitude of the spectral component (the length of the vector) and the phase of the corresponding oscillation (the angle of the vector).

[†] The difference of the window functions lies in subtle trade-offs among the various figures of merit that can be used to describe the narrowness of the spectral leakage functions.

statistical reliability can be increased by smoothing the data using certain methods, for example, the triangular weighting function, but unfortunately, one pays the price of a lower effective frequency resolution. For a 5 min recording, the smoothing range should not be more than 0.01 Hz.

2.4.1.2 FFT Algorithm

The discrete Fourier transform can be computed directly using Equation 2.1, but such an operation would be very time consuming. The FFT is a very effective *algorithm* to evaluate the discrete Fourier transform (Marple, 1987; Kay and Marple, 1981). It has one limitation: the number of data point N must be an integer power of 2. Since normally the length of the time series is not a power of 2, the data can be padded with zeros up to the next power of 2. This operation corresponds to the interpolation of the original data. Since the actual N used in the FFT calculation is different from the original one, the f_n s are also slightly different.

2.4.2 Autoregressive Modeling

The AR model is based on the idea that the future values of a time series depend linearly on the previous values (Akaike, 1969). This kind of approach is totally generic, and it can be used to model large sets of different systems. The AR model is determined from the following equation:

$$x_k = \sum_{j=1}^p a_j x_{k-j} + u_k, \quad (2.2)$$

where x_k is the sample of the time series, a_j is the model parameter, p is the model order and u_k represents the noise, the part of the signal that cannot be explained by the previous values of the signal. The computational task is to find optimal model order p such that parameters a_j of the model describes the system as well as possible. When we have such a model, it is possible to compute the corresponding PSD in the form

$$\text{PSD}(f) = \frac{a_0}{\left| 1 + \sum_{j=1}^p a_j z^j \right|^2}, \quad z = e^{-2\pi i f \Delta}, \quad (2.3)$$

where f is the frequency and Δ is the sampling interval, as usual. The PSD (Equation 2.3) is capable of modeling sharp peaks since all free parameters are in the *denominator*, which can be made arbitrarily small.* The PSD approximation (Equation 2.3) is also called an *all-poles model* and *maximum entropy method*. There are many algorithms to find the best choices for the parameters a_j , but Burg's method is commonly used. Because the AR spectrum is based on a modeling approach, there are no restrictions for the maximal number of frequency components, that is, PSD can be evaluated using as high a frequency

* In fact, the denominator can be, at least in theory, even zero at certain frequencies. These zeros (also called the *poles* of Equation 2.3) correspond to the spectral peaks.

resolution as one desires (f in Equation 2.3 is actually a continuous variable), in contrast to the Fourier spectrum where the frequency resolution is determined by the number of data samples. Furthermore, the AR model makes it possible to resolve the central frequencies (the frequency location of each peak) analytically. In clinical setups, this feature is rarely useful, but in research work, it could be interesting.

2.4.2.1 Model Order

The model parameters can be estimated if the model order p is fixed. It could be imagined that the model would be best when using as high a model order as possible. However, in practice, time-series data always include some noise (the term u_k in Equation 2.2), so an excessively high model order leads to the model capturing the noise, producing a spectrum with spurious peaks. Too high a model order can also split peaks. Again, too low a model order will strongly smooth spectral peaks, their positions can be shifted and some peaks can even be missing. Some methods have been developed based on information theory for estimating the optimal model order, such as Akaike information criteria (AIC), final prediction error (FPE) or minimum description length (MDL) (Akaike, 1969; Rissanen, 1983; Partzen, 1974). The analytical assumptions underlying these methods are hardly ever fulfilled when analyzing the RR interval time series. Thus, they provide only limited assistance in determining the model order. Therefore, it is recommended that the AR method be used in conjunction with the Fourier transform method (or some other direct method) to help choose the correct model order and to avoid getting spurious spectral features.

2.4.3 Resampling

The RR interval time series is an event series, as stated previously, and each interval has a time stamp, which is the cumulative sum of all preceding intervals. The data can be interpreted as a hypothetical continuous function that has been sampled *unevenly* in time at the moments of R peaks. In spectral analysis, either in Fourier transform or in AR modeling, the input data ($x(t_k)$ in Equation 2.1 or x_k in Equation 2.2) are assumed to be the data sampled evenly in time. Hence, the original RR interval data must be converted to such a form by interpolating each interval and resampling this apparently continuous function.* Interpolation can be linear (each interval is interpolated by a straight line) or based on splines.[†] The method of interpolation makes no essential difference in HRV analysis.

The resampling frequency must clearly be higher than the *effective sampling rate* of the RR interval data, but it is not critical. The effective sampling rate is equal to the mean heart rate, typically around 1 Hz (= 60 bpm). In practice, a resampling rate of 2–5 Hz is adequate, and there is no need to use a higher rate. In Fourier transform analysis, the highest-frequency component is $f_c = 1/2\Delta$, and it increases by a resampling of the data. However, resampling cannot increase the information content of the data, and thus, the highest relevant frequency component is still half of the (effective) sampling rate according to the general sampling theorem (Nyquist criteria); with 60 bpm mean

* The spectrum of event series can be computed correctly without any interpolation and resampling by using the Lomb–Scargle (also called Lomb periodogram) method. This method makes it possible to calculate the spectrum up to frequencies *above* the Nyquist frequency (= half of the sampling rate or mean heart rate).

[†] Splines are second-order or higher-order polynomials. If the order is 2, then the spline curve is a parabola with three free parameters, two of them are fixed by demanding that it goes through the data points of the interval and the last one is fixed by demanding that the derivative of the curve is continuous at the data points.

heart rate, $f_c = 0.5$ Hz. This is also true in the case of AR modeling, although the PSD estimate can be evaluated up to any frequency. One should notice that when increasing the resampling rate, the order of the AR spectrum must be increased correspondingly.

Sometimes the resampled data are low-pass filtered using a cutoff frequency of 1 Hz (or half of the resampling frequency). Although this operation can, in theory, improve the statistical reliability of the data, it has no real significance in HRV analysis.

2.4.4 Spectral Powers

The total power (TP) of the RR interval data is represented by the area under the PSD curve from zero to the highest relevant frequency f_c , and it is equivalent to the variance of the signal. In a typical short-time (≥ 5 min) spectral analysis, the spectral power is divided into three frequency bands: *high frequency* (HF; 0.15–0.40 Hz), *low frequency* (LF; 0.04–0.15 Hz) and *very low frequency* (VLF; 0–0.04 Hz). In long-term recordings, an *ultralow frequency* (ULF; 0–0.003 Hz) component can be calculated. The HF component corresponds to heart rate variations related to the respiratory sinus arrhythmia and HF fluctuations are mediated almost exclusively by fluctuations of efferent parasympathetic activity. The central role of sympathetic nervous system on the LF component is well known, but fluctuations in the LF band are also markedly influenced by parasympathetic nervous system. The LF band is important when characterizing baroreflex sensitivity using spectral methods (see Chapter 3). Oscillations at frequencies in the VLF band are often related to the vasomotor tone of thermoregulation or to the dynamics of hormonal systems, but a precise origin of oscillations in this band is still unknown.

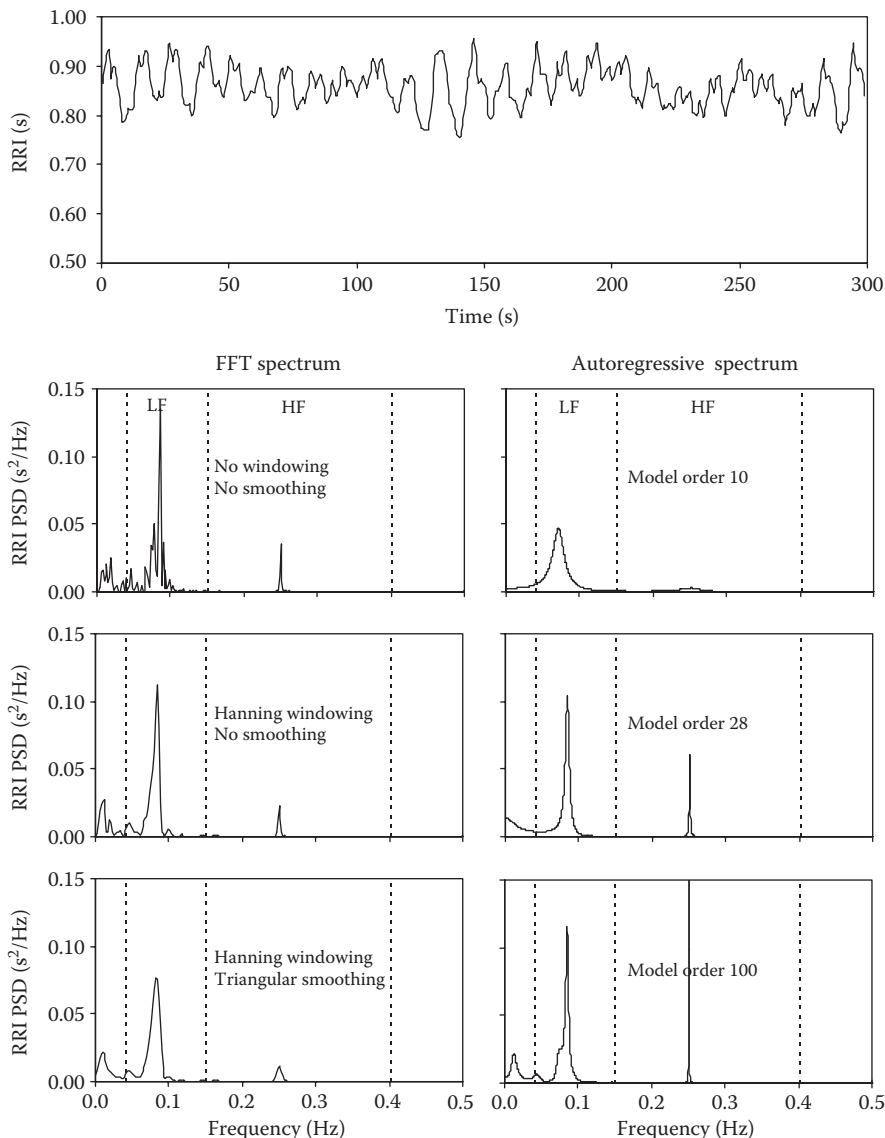
The magnitude of HRV in each frequency band is expressed as power. Since the unit of PSD function is either ms^2/Hz or s^2/Hz depending on the unit of RR interval time series, the unit of HRV power is ms^2 or s^2 . Because the TP and power in each frequency band vary considerably even among healthy subjects of equal age, direct comparisons of power between two subjects can be misleading. For this reason, powers are usually expressed in normalized units, by dividing each power by TP less VLF power. Therefore, normalized powers are not absolute measures either, since they partially reflect the relative powers of LF and HF components.*

The confidence we can have in the accuracy of the power in VLF, LF and HF bands varies, since it is related to the number of full periods of oscillations in each band. If we have a 5 min recording, there are roughly 0–12 periods of the oscillation in the VLF band, 12–45 periods in the LF band and 45–120 periods in the HF band. Although the recommended minimum length of recording for a short-term spectral analysis is 5 min, sometimes it is necessary to use shorter segments due to artifacts, ectopic beats and so on. As a rule of thumb, one can use the criterion that the minimum number of periods be six.[†] In order to have a reliable power estimate, for instance, in the whole LF band, we need at least 2.5 min worth of usable recording. Similarly for ULF power, the minimum recording length is about 1 h.

A typical example of spectral HRV analysis performed with FFT and AR modeling is presented in Figure 2.1. The length of the RR interval time series was 5 min, and it consisted of 349 intervals. The mean RR interval was 856 ms, corresponding to a heart rate of 70.2 bpm. The spectral analysis was done over the whole time series. Before any analysis,

* If we have two cases with equal absolute LF powers but different HF powers, the normalized LF powers are not equal.

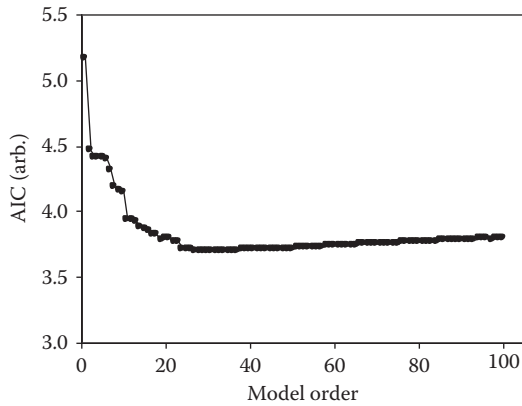
[†] This is actually an arbitrary number of periods, but in practice, it has proven to be a useful minimum number.

**FIGURE 2.1**

RR interval time series and corresponding FFT and autoregressive spectrum.

the linear trend was removed. The time series was linearly interpolated and resampled using a sampling frequency of 2 Hz. According to the mean heart rate, the highest relevant frequency f_c was $70.2 \text{ (beats/min)} / 60 \text{ (s/min)} / 2 = 0.585 \text{ Hz}$, well above the upper end of the HF band. The frequency resolution of the FFT spectrum is 0.00195 Hz^* . There are clear peaks in both the LF and the HF bands in all versions of the FFT spectrum (left panels). The HF component is very sharp since metronome-controlled breathing was used.

* After resampling at the sampling rate of 2 Hz (the sampling interval $\Delta = 0.5 \text{ s}$), the 5 min time series has 600 data points. This has been zero padded to the next power of 2; here, it is 1024. The frequency resolution is $1/N\Delta = 1/(1024 \times 0.5 \text{ s}) = 0.00195 \text{ Hz}$.

**FIGURE 2.2**

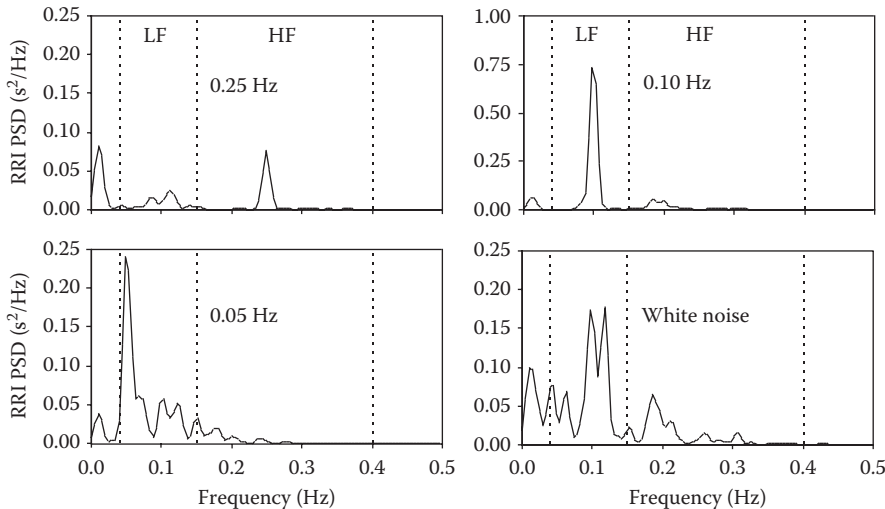
The Akaike information criteria (AIC) of the time series of Figure 2.1 as a function of the model order. The minimum of AIC is reached at the model order of 28.

Without windowing or smoothing, the FFT spectrum clearly includes HF components, which disappear after using the Hanning window function. By also applying triangular smoothing (range 0.01 Hz), the spectrum has even less detail, but the statistical reliability of the spectral features has increased. The AR spectrum (right panels) with the model order of 10 cannot capture all essential features. If the model order is increased to 28 (the optimal model order according to AIC, that is, the order at which AIC is at its minimum value, see Figure 2.2), the spectrum resembles the FFT spectrum. If the model order is further increased up to 100, more spectral details can be seen, especially in the lowest frequencies. It is remarkable how similar the spectral details below 0.05 Hz are in both FFT (windowed and smoothed) and AR spectra (model order 100). Although AIC has a minimum value at 28, it increases very slowly with increasing model order. Thus, it is not always obvious which model order should be selected.

2.4.6 Effects of Respiration

The respiratory component of HRV depends strongly on the breathing volume and its frequency. The HF component decreases markedly as breathing volume decreases. In addition, the power of respiratory peak increases as its frequency decreases. If the breathing frequency is below 0.15 Hz, it becomes measured not as the HF component but as a part of the LF component. The effect of the breathing frequency on HRV is presented in Figure 2.3. The breathing volume was fixed in all cases. When the breathing frequency was fixed at 0.10 Hz (the upper right panel in Figure 2.3), the amplitude of the respiratory peak was approximately 0.25, ten times higher than at the breathing frequency of 0.25 Hz (the upper left panel; note the different scale in the *y*-axis). At a breathing frequency of 0.05 Hz, the peak was still three times higher (the lower left panel).

In practice, the HF component can be used as a measure of parasympathetic tone and vagal activity only in situations in which the breathing frequency and volume are carefully controlled. Controlled respiration at a constant rate, however, can induce some stress, which might affect the function of the autonomic nervous system and therefore interfere with HRV. Using a respiratory frequency that is as close as possible to the natural breathing rate of the subject, one can minimize the stress. This can be accomplished by first measuring the

**FIGURE 2.3**

RR interval FFT spectra at three different breathing frequencies of 0.25, 0.10 and 0.05 Hz and using white noise breathing. Note that the y -scale is different in the case of 0.10 Hz.

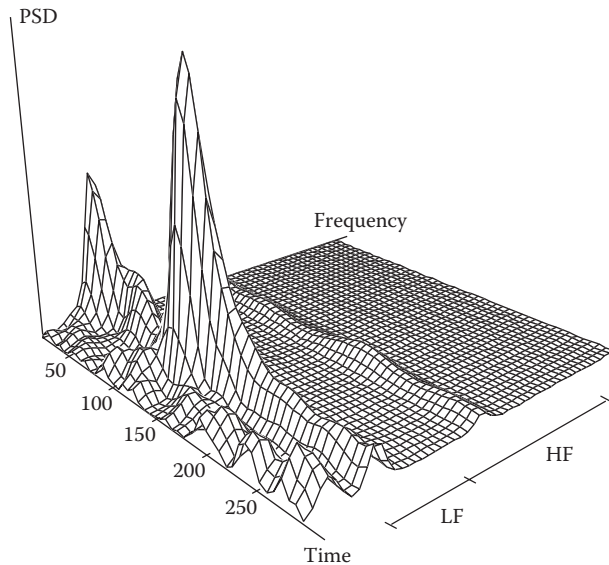
breathing rate and then adjusting the frequency of metronome accordingly. Another possibility is to use white noise breathing, that is, a metronome guides the subject to breathe at variable rates with constant distribution (see the right bottom panel in Figure 2.3).

2.4.7 Time–Frequency Analysis

When considering perturbation of the autonomic nervous system, usual steady-state spectral analysis methods are no longer useful, since they cannot determine exactly when critical frequency components change in amplitude or frequency. Conversely, if information about temporal variations of frequency components were available, spectral features of slowly changing system could be analyzed in more detail, for instance, to estimate the stationarity of a time series. There are many different approaches to perform a time–frequency analysis, and most of them are based on various integral transforms of the original data. The main limitation on all of them is the trade-off between temporal resolution and statistical reliability of spectral components. It is not possible to determine the amplitude of a certain frequency locally because we always need a time window to measure it. A shorter time window can capture more rapid changes within the power spectra in time, but a longer time window can give a more reliable estimate of the amplitude or spectral power.

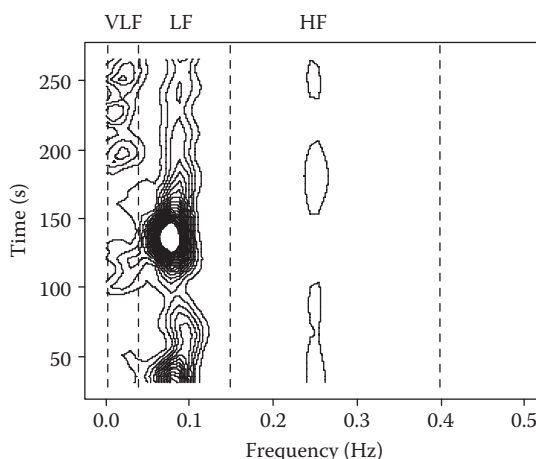
2.4.7.1 Windowed Fourier Transform

The most simple and straightforward time–frequency analysis is called the *windowed Fourier transform* (WFT, also called short-time Fourier transform or STFT). In this approach, the time series is covered by a reasonably short time window that slides over the data in small steps. In each window, the PSD is calculated as described above (e.g., using data windowing, zero padding, trend removing and resampling). As a result, one gets a set of PSDs. In Figure 2.4, we present the results of a WFT performed on the same RR interval data shown in Figure 2.1 as a three-dimensional plot. The width of the window was 60 s

**FIGURE 2.4**

Time-frequency analysis of the RR interval time series using windowed Fourier transform method.

and the step 5 s. The RR interval has prominent low-frequency oscillations around 140 s (see the upper panel in Figure 2.1), and this can be also seen as a large peak in Figure 2.4. Furthermore, the respiratory modulation (the shallow peak in the HF band) seems to be almost constant in time. Although the window step is 5 s, the real-time resolution of the analysis is still approximately 60 s. If there had been an abrupt change in the spectral features of the signal, it would be seen in all the windows covering that moment in time. The same analysis is presented as a contour map in Figure 2.5. This representation reveals that there are a lot of variations in the VLF and LF bands.

**FIGURE 2.5**

Same as Figure 2.4 but displayed as a contour map.

Since the number of periods within the window of WFT depends on the frequency, the statistical reliability is different for each frequency component as discussed in Section 2.4.4. If the width of the window is set for the lower frequency components, it becomes unnecessarily wide for higher frequencies. This feature can be avoided if the duration of the window is inversely proportional to the analyzed frequency. This kind of analysis is called *selective discrete Fourier transform algorithm* (SDA) and can be implemented by normal discrete Fourier transform, but it is computationally intensive (Keselbrener and Akselrod, 1996).

2.4.7.2 Wigner–Ville Distribution

The Wigner–Ville bilinear distribution (WVD) of the continuous function $x(t)$ is defined by

$$\text{WVD}(t, f) = \int_{-\infty}^{\infty} x\left(\frac{t+\tau}{2}\right) x^*\left(\frac{t-\tau}{2}\right) e^{-2i\pi f\tau} d\tau. \quad (2.4)$$

The WVD maps a one-dimensional function of time into a two-dimensional function of time and frequency (Claassen and Mecklenbräuker, 1980a,b; Hyung-Ill and Williams, 1989; Novak and Novak, 1993). For a discrete time series $x(n)$, the distribution (Equation 2.4) can be written in the form

$$\text{WVD}(n, k) = \sum_{\tau=-\infty}^{\infty} W_N(\tau) e^{2\pi i k \tau / N} \left[\sum_{\mu=-\infty}^{\infty} W_M(\mu) K(\mu, \tau) x(n + \mu + \tau) x^*(n + \mu - \tau) \right], \quad (2.5)$$

if the kernel function K and W is equal to 1. This distribution is also called a *smoothed windowed* WVD because of the window functions W_M and W_N . The function W_M is a rectangular window that has a value of 1 for the range of $-M/2 < \mu < M/2$, and W_N is a symmetrical window (often also rectangular), which has non-zero values for the range $-N/2 < \tau < N/2$. The parameter N determines the frequency resolution of the WVD, while the parameter M determines the level of temporal smoothing.

The frequency resolution of the spectrum calculated by the WVD is two times the resolution of the FFT spectrum when using the same length of time window, therefore making WVD more suitable than FFT for shorter time series. However, WVD has another problem: if there are two frequency peaks f_1 and f_2 close to each other, the WVD spectrum also contains small but significant erroneous components at the frequencies $f_1 - f_2$ and $f_1 + f_2$. In the case of multiple dominant frequency peaks, the background of WVD spectrum can be contaminated by many spurious frequency peaks of low amplitude. This feature of the WVD method forces us to be careful when interpreting the finer details of the spectrum. The cross-terms can be suppressed by introducing a suitable non-trivial kernel function K in Equation 2.5, but unfortunately at the price of lower frequency resolution. One example of such a kernel function is the so-called *exponential distribution*.

2.4.7.3 Complex Demodulation

The complex demodulation (CDM) method is a common non-linear method used to define the amplitude of a time series at a specified frequency or frequency band as a function of time (Kim and Euler, 1997). In other words, for a given frequency ω , we assume the signal is of the form

$$x(t) = A(t) \cos(\omega t + \phi(t)) + z(t), \quad (2.6)$$

for which we need to determine the amplitude $A(t)$ and the phase $\phi(t)$. The term $z(t)$ contains all other oscillating components (having a frequency different from ω) and possible noise. In the CDM method, the original real value signal $x(t)$ is rewritten into complex format

$$x(t) = 0.5A(t) \left\{ e^{i(\omega t + \phi(t))} + e^{-i(\omega t + \phi(t))} \right\} + z(t), \quad (2.7)$$

where i is the imaginary unit. In the next step, all frequency components are shifted by $-\omega$. This operation is equivalent to multiplying $x(t)$ by the term

$$y(t) = 2e^{-i\omega t}, \quad (2.8)$$

which gives us

$$x'(t) = A(t)e^{i\phi(t)} + A(t)e^{-i(2\omega t + \phi(t))} + 2z(t)e^{-i\omega t}. \quad (2.9)$$

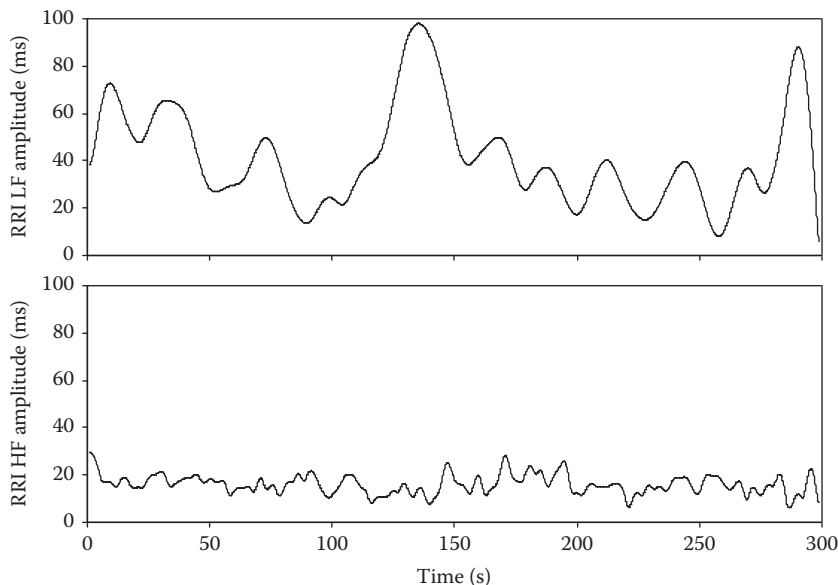
Here, we see that the frequency of the first term is zero and the frequency of the second term is twice that of the component under study. The last term does not contain frequencies around zero, because the component $z(t)$ did not originally contain the frequency ω . If the signal $x'(t)$ is fed into a low-pass filter with a cutoff frequency at zero, we get the signal

$$x''(t) = A(t)e^{i\phi(t)}, \quad (2.10)$$

from which we can easily calculate the slowly and time-dependently changing amplitude $A(t)$ since $A(t) = |x''(t)|$. Likewise, we can get the amplitude of any desired frequency signal as a function of time (by varying ω). If the cutoff frequency is $\Delta\omega$ and not exactly zero, the CDM method picks from the signal only the amplitude of those components with a frequency between $\omega - \Delta\omega$ and $\omega + \Delta\omega$. In this way, it is possible to pick the part of the signal that belongs, for example, to the LF or HF band.

Therefore, theoretically, the CDM method can give the amplitude at every moment of time, but in reality, the temporal resolution depends upon the characteristics of the low-pass filter. If the desired frequency band is to be limited as steeply as possible, one needs to use a higher-order filter, but in that case, one needs more data points to perform filtering, and the time resolution will be lower. In practice, time resolution of the CDM method applied to the RR interval time series is approximately 15 s when analyzing oscillations in the LF band. Any faster changes in the amplitude of oscillations cannot be clearly distinguished. This temporal resolution is, however, clearly better than the resolution obtained with other methods.

The CDM amplitudes of the RR interval data (the same time series as in Figure 2.1) in the LF and HF bands are shown in Figure 2.6. Again we see that there are significant changes in the LF component, but the HF component is almost constant.

**FIGURE 2.6**

The amplitude of the LF and HF components of the RR interval time series (the same data as in Figure 2.1) as a function of time based on CDM method.

2.4.7.4 Other Methods

In the method of sliding window analysis, the Fourier transform can be replaced with AR modeling. If there are significant changes in the structure of HRV data as a function of time, the optimal model order should be obtained individually in each window. A similar approach called *time-variant autoregressive modeling* is suitable for online monitoring (Bianchi et al., 1997). In this method, a new set of AR parameters is computed whenever a new sample value is available, and the weight of the previous samples is controlled by means of a forgetting factor.

The *Wavelet transform* is a general tool for analyzing the temporal changes in time series (Figliola and Serrano, 1997). The continuous wavelet transform (CWT) of the time series $x(t)$ is defined as

$$\text{CWT}(a, \tau) = \frac{1}{\sqrt{a}} \int x(t) \Psi\left(\frac{t-\tau}{a}\right) dt, \quad (2.11)$$

where $\Psi(t)$ is the basic (or mother) wavelet. The wavelet transform, similar to STFT, maps a time function into a two-dimensional function of a and τ . The parameter a is called the scale^{*}; it scales the wavelet function by compressing or stretching it. τ is the translation of the wavelet function along the time axis. There are an infinite number of valid wavelet functions, but all of them are well localized.[†] By contrast, the STFT uses truncated sine waves, which are not well localized. The shape of the wavelet function must be selected according to the application. Furthermore, by increasing the window width in STFT, the

^{*} Inverse of the scale can be interpreted as a frequency.

[†] The wavelet is well localized since it goes rapidly to zero in infinity.

number of periods increases, but in the wavelet transform, basic shape of the wavelet is same; it is only compressed or stretched. All of these features of wavelets make them ideal for capturing rapid temporal changes. Although wavelet analysis has been applied to the HRV signal, results are not superior to those obtained using more traditional approaches (Wiklund et al., 1997).

2.5 Non-Linear Analysis

2.5.1 Approximate Entropy and Sample Entropy

All frequency domain analyses are based on the recognition of certain predetermined patterns. For instance, in Fourier transforms, the pattern is a sinusoidal wave, and in wavelet analysis, the pattern is a certain wavelet function. Another alternative for characterizing the variability of heart rate is to measure the regularity or complexity of the fluctuations without specifying the form of repeating patterns. Entropy is a general approach for quantifying the regularity or information content of the data (Pincus and Goldberger, 1994; Pincus, 1995; Bettermann and van Leeuwen, 1998; Cysarz et al., 2000). There are many ways to determine the entropy of a time series, but most of them require noise-free data and very long recordings. *Approximate entropy* (ApEn) has been developed for measuring the complexity of relatively short time series and it is most useful for HRV analysis where long noise-free recordings are difficult to obtain (Pincus and Goldberger, 1994). Furthermore, ApEn calculations are not based on specific assumptions regarding the internal structure or dynamics of the system.

ApEn is computed as follows. First we construct the so-called pseudo phase space vectors from the initial time series $x(i)$, in which $i = 1 \dots N$, N being the number of data points

$$u(i) = [x(i), x(i+1), x(i+2), \dots, x(i+m-1)], \quad (2.12)$$

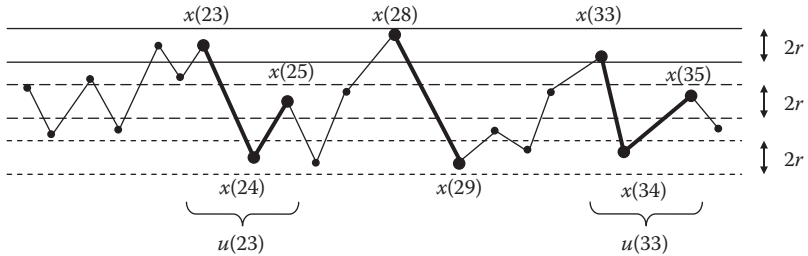
m being the so-called *embedding dimension*.* Vectors $u(i)$ can be interpreted as m -point patterns. First, we select one m -point pattern and search for similar m -point patterns. Two patterns are similar when the maximum distance d between the corresponding components is less than the *tolerance* r (Figure 2.7):

$$d[u(i), u(j)] = \max \left\{ |u(i+k) - u(j+k)| : 0 \leq k \leq m-1 \right\} \leq r. \quad (2.13)$$

The (normalized) number of similar vectors $u(j)$, which are at a distance r from $u(i)$, is

$$C_i^{(m)}(r) = \left\{ \text{the number of index } j \text{ for which, } j \leq N-m+1, d[u(i), u(j)] \leq r \right\} / (N-m+1). \quad (2.14)$$

* The use of pseudo phase vectors is a starting point of many non-linear analysis methods. The idea of these vectors is that they can be used as a *replacement* for the set of true dynamical variables, all of which we cannot measure either for technical reasons or since we actually do not know them. Under certain assumptions, the dynamics of the pseudo phase vectors is similar to the real dynamical variables.

**FIGURE 2.7**

Approximate entropy. An example showing for embedding dimension $m = 2$, a search for similar pseudo phase space vectors. For vector $[x(23), x(24)]$, two nearby vectors, $[x(28), x(29)]$ and $[x(33), x(34)]$, are found to be similar, that is, the distance between $x(28)$ and $x(33)$ and the distance between $x(29)$ and $x(34)$ are both $<$ tolerance value r . Therefore, both $u(28)$ and $u(33)$ increase the quantity $C_{23}^{(2)}(r)$. However, when m is increased to 3, only vector $[x(33), x(34), x(35)]$ is similar to $[x(23), x(24), x(25)]$ and increases $C_{23}^{(3)}(r)$.

Due to normalization, the maximum value of C is 1, and C can be regarded as the probability of finding similar m -point patterns. The same analysis can be performed for all m -patterns. The logarithmic average of probabilities over all m -patterns is

$$\Phi^m(r) = (N - m + 1)^{-1} \sum_{i=1}^{N-m+1} \ln C_i^m(r). \quad (2.15)$$

Approximate entropy is defined as

$$\text{ApEn}(m, r, N) = \Phi^m(r) - \Phi^{m+1}(r). \quad (2.16)$$

One sees that ApEn measures the (logarithmic) conditional probability that similar m -patterns are similar also when looking for $(m + 1)$ -patterns. In other words, ApEn is the averaged probability of finding m -patterns minus the averaged probability of finding $(m + 1)$ -patterns (see Figure 2.7). If the last probability is equal to the first one, $\text{ApEn} = 0$, i.e., the time series is absolutely regular in this sense. However, if the last probability is zero, ApEn gets its maximum value, i.e., the time series is totally irregular.

$\text{ApEn}(m, r, N)$ is dependent on three parameters: the length m of the vectors being compared, the tolerance parameter r , and the number N of data points. This means that direct comparisons always require fixing of parameters. For HRV analysis, $m = 2$ is the value normally used. When the number of data points is increased, ApEn approaches its final value asymptotically. In practice, $N > 800$ and $m = 2$ give a reliable result. ApEn depends strongly on the tolerance parameter r . If r is chosen such that it is a fraction of the SD of the data, ApEn does not depend on absolute variability.* The most frequently used value of r is 15 or 20% of SD.

ApEn is sensitive to smallest trends in the data, because comparison of patterns is based on the absolute values of data. The trend can be removed before ApEn analysis but with

* If r is a fraction of SD, ApEn does not depend on the unit of data, and therefore, it is also possible to compare the ApEn values of different signals, such as RR interval and systolic pressure time series.

cautions as described in Section 2.2.5. One alternative is to use the differentiated data (the difference of successive RR intervals) that eliminate all slow trends, but this operation behaves like a special high-pass filter in the frequency domain. ApEn is not sensitive to changes in single data values if the tolerance parameter is fixed, but if the tolerance parameter is bound to the SD as recommended, the situation could well be different. Ectopic beats especially, if not edited, can alter the SD significantly.

When calculating the number of similar vectors to get ApEn, the similarity of the vector to itself is included in the calculation. This ensures that $C_i^{(m)}(r)$ is non-zero, which is essential for calculating the logarithm. This causes ApEn to give a result most of the time, which implies greater regularity of the signal than may be present.

Sample entropy (SampEn) is calculated in a way that removes the previously described bias (Richman and Moorman, 2000). When calculating the number of nearby vectors, a comparison to the vector itself is prevented:

$$C_i^{(m)}(r) = \left\{ \text{the number of index } j \text{ for which, } j \neq i, j \leq N - m + 1, d[u(i), u(j)] \leq r \right\} / (N - m + 1). \quad (2.17)$$

The average of the probabilities Φ is also defined without logarithms

$$\Phi^{(m)}(r) = (N - m + 1)^{-1} \sum_{i=1}^{N-m+1} C_i^{(m)}(r). \quad (2.18)$$

Now SampEn is defined as

$$\text{SampEn}(m, r, N) = \ln(\Phi^{(m)}(r) / \Phi^{(m+1)}(r)). \quad (2.19)$$

The interpretation and use of SampEn remain exactly the same as for ApEn. However, the dependence on the tolerance parameter r and the number of data points N is different. ApEn reaches its maximum with a certain value of r , but SampEn decreases monotonically as r increases. SampEn is, in principle, also independent of the number of data points N , but with small values of N , its statistical reliability is naturally poor. When r and N are large enough, SampEn and ApEn yield the same result. SampEn provides a more reliable estimate of the complexity of a signal compared to ApEn. It may be used for considerably shorter time series than the ApEn, (<200 points).

Regularity and complexity are often interpreted as being contrary to each other: increased regularity means lower complexity and vice versa, but this is not always true. The degree of regularity can be quantified by evaluating the appearance of repetitive patterns and characterized by entropy measures. Complexity is, however, intuitively associated with *meaningful* structural richness, which can exhibit relatively high regularity. Entropy-based measures grow monotonically with the degree of randomness and they reach highest values from totally uncorrelated random data or white noise. Such data are unpredictable but not actually complex. Thus, entropy measures may lead to misleading results when they are applied to physiological time series such as the heart rate signal. For example, atrial fibrillation (AF) is associated with highly erratic fluctuations with statistical properties resembling uncorrelated noise. The entropy value of such

a signal is high. By contrast, healthy cardiac rhythms that are regulated by multiple interacting feedback mechanisms will yield lower entropy values. This inconsistency is obviously related to the fact that entropy measures are based on single-scale analysis, but many biological systems operate across multiple spatial and temporal scales and hence their complexity is also multiscaled.

To overcome the aforementioned difficulties in interpreting entropy measures, *multiscale entropy* (MSE) analysis has been introduced (Costa et al., 2002, 2005). In this method, the coarse-grained time series determined by the scale factor τ is defined as

$$y^{(\tau)}(j) = \frac{1}{\tau} \sum_{i=(j-1)\tau+1}^{j\tau} x(i), \quad (2.20)$$

where $x(i)$ is the original time series and $1 \leq j \leq N/\tau$. For a scale of 1, the time series $y(j)$ is simply the original time series. The length of $y(j)$ is equal to the length of the original time series divided by the scale factor. In the next step, the entropy of the coarse-grained time series is calculated as a function of the scale factor. In principle, the entropy can be calculated using any method that is reliable for a time series of variable length, and SampEn is a good choice when analyzing the RR interval time series. In order to have good statistical reliability at higher scales, the number of data points must be greater than 10,000. This limits the use of MSE in many clinical studies.

As an example, the MSE method has been applied to three different subjects: one healthy, one with congestive heart failure (CHF) and one with AF (see Figure 2.8). At the scale of 1, the healthy and CHF cases cannot be separated, but if the scale is 5 or 6, large separation can be obtained. Entropy of AF time series is highest at a scale of 1, but it decreases monotonically as the time scale increases, similar to white noise. At a very large time scale, CHF and AF time series cannot be separated any more. We conclude that MSE can distinguish these cases, but it needs computation of the entropy as a function of scale; no single entropy value at a fixed scale is enough.

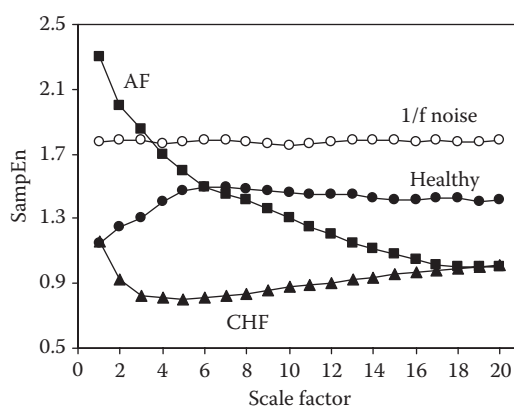


FIGURE 2.8

Multiscale entropy analysis of an RR interval time series derived from healthy subjects, congestive heart failure (CHF) subjects and subjects with atrial fibrillation (AF). As reference, the results of simulated $1/f$ noise are presented.

2.5.2 Scaling Exponents

2.5.2.1 Detrended Fluctuation Analysis

When analyzing a longer time series lasting several hours, identification of oscillatory components or repeated patterns are not the best approach for examining the HRV data. One method is to characterize the internal correlations of the signal. These correlations are expressed by scaling properties and fractal structures. Detrended fluctuation analysis (DFA) presents a possibility for characterizing this as a function of correlation distance (Peng et al., 1993, 1995; Iyengar et al., 1996).

To calculate DFA, we must first form an integrated version of the original time series $x(i)$, where $i = 1 \dots N$, which gives us

$$y(k) = \sum_{i=1}^k (x(i) - \langle x \rangle), \quad (2.21)$$

where $\langle x \rangle$ is the mean of the original time series and $k = 1 \dots N$. Next, we divide the time series $y(k)$ into equally spaced segments with length n as shown in Figure 2.9. For each segment, we calculate separately the local trend by fitting a regression line $y_n(k)$ to the segment. The RMS (root-mean-square) fluctuation of the integrated time series is calculated by removing the linear trend of each segment. Thus,

$$\text{DFA}(n) = \sqrt{\frac{1}{N} \sum_{k=1}^N [y(k) - y_n(k)]^2}. \quad (2.22)$$

In the summation, we must take into account that when the index k is stepped, $y_n(k)$ must be updated when moving into the next segment. DFA is calculated for several different segment lengths, that is, n values. Typically, DFA increases when the segment length increases. If $\log(\text{DFA})$ increases linearly as a function of $\log(n)$, the time series follows (fractal) scaling law, and in this case, the slope α of the linear change, the *scaling exponent*,

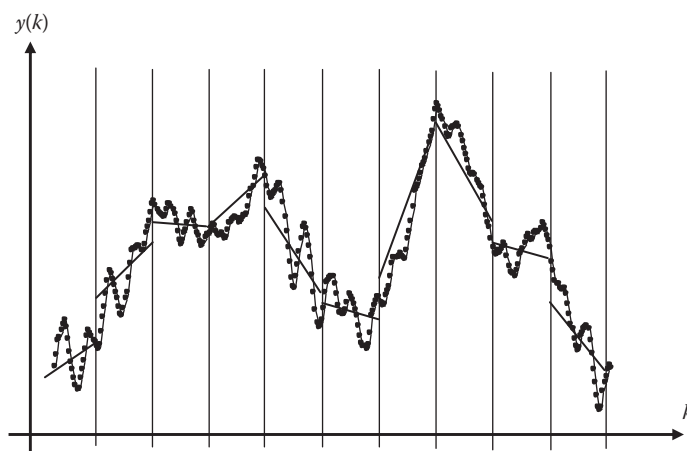


FIGURE 2.9

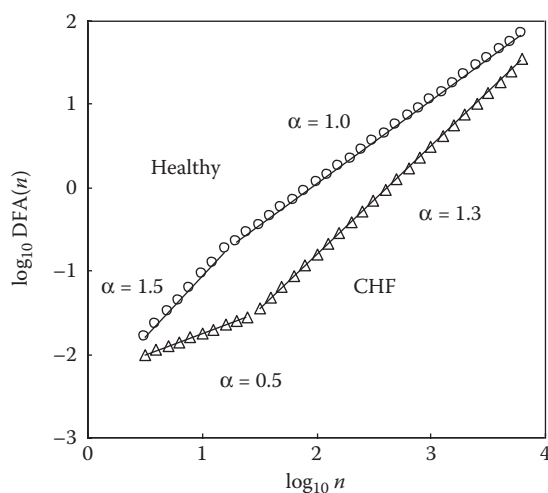
The integrated time series and the local trends.

TABLE 2.1Scaling Exponent α of Certain Type of Time Series

| Scaling Exponent | Description of the Signal |
|----------------------|--|
| $0 < \alpha < 0.5$ | Small value followed most probably by a larger value and vice versa |
| $\alpha = 0.5$ | Completely uncorrelated time series, that is, white noise |
| $0.5 < \alpha < 1.0$ | Small value followed most likely by a small value and large value followed most likely by a large value (correlated) |
| $\alpha = 1.0$ | $1/f$ type noise |
| $1.0 < \alpha < 1.5$ | Noise of variable type |
| $\alpha = 1.5$ | Brownian $1/f^2$ noise (integral of white noise) |

defines the type of scaling. Different values of α correspond to specific types of time series as presented in Table 2.1.

A typical DFA of long RRI time series is shown in Figure 2.10. A heartbeat has short-range correlations reflecting the baroreflex mechanism, as well as long-range correlations, which are related to the efforts to keep the variation of the beat cycle within certain limits. The measurement of the long range correlations requires that the time series under investigation be preferably at least a few hours long so that the statistical reliability would be at least reasonable. The limit for short- and long-range correlations is set typically to 10 or 11 beats (corresponding to 2.4 on the logarithmic scale). The long-range scaling exponent α_L for a healthy patient is ≈ 1 , which corresponds to $1/f$ behavior. The short-range scaling exponent α_S may vary, but it is usually between 0.5 and 1.5. Many factors affect it, such as the functioning of the baroreflex mechanism, breathing modulation and so on. With a longer time series, there always exists the possibility that the measured correlations are not at all a characteristic of the system but rather reflect environmental effects.

**FIGURE 2.10**

DFA as a function of the number of segments for healthy and CHF subjects.

2.5.2.2 Spectrum Power Law Exponent

Long-range correlations of a time series may also be analyzed using the spectrum of the signal. In this case, we can study the lowest-frequency components of the spectrum and try to characterize its shape using simple exponential law. If we presume that for a certain frequency spectrum we have $1/f^\beta$, the scaling exponent β can be calculated by presenting the spectrum on a log-log scale and by fitting a line over the desired frequency range (Iyengar et al., 1996; Bigger et al., 1996). The slope of the line gives the spectrum power law exponent. The value of the exponent varies between 0 and 2. The border line case 0 corresponds to a flat spectrum, that is, white noise, and the value 2 corresponds to Brownian noise. Usually, the frequency range 0.0001–0.01 Hz of the spectrum is studied, and this corresponds to an oscillation period of 1 min to several hours. For the above definition to make sense, the HRV time series must be several hours long. The spectrum is calculated almost without exception using the FFT algorithm. Because the spectrum has a rather irregular form, especially at the lowest frequencies, the use of some smoothing method is desirable. Replacing the regression line with a less sensitive fitting method may also improve the reliability of the result.

2.5.3 Fractal Dimensions

2.5.3.1 Correlation Dimension

The dynamics of a system can be described by measuring its attractor (the path toward which the system converges) *dimension*. Especially for chaotic systems, the attractor can be fractal, in which case its dimension is not an integer. Knowing the dimension of the attractor may also help getting useful information about the characteristics of underlying systems. The correlation dimension (CD) is one of the simplest methods for estimating the attractor dimension (Grassberger and Procaccia, 1983; Kantz and Schreiber, 1995; Yum et al., 1999). The CD is sometimes referred to with the designation D_2 .

The basis for the calculations once again is in the reconstruction of time series in the multidimensional phase space $x(i)$, where $i = 1 \dots N$, by using the vectors of the pseudo phase space $u(i) = [x(i), x(i+1), x(i+2), \dots, x(i+m-1)]$, where m is the embedding dimension. Next, we calculate for each vector $u(i)$, how many attractor points are at a distance r as measured from the observation point

$$C_i^m(r) = \left\{ \text{the number of index } j \text{ for which, } j \leq N - m + 1, d[u(i), u(j)] \leq r \right\} / (N - m + 1), \quad (2.23)$$

where the distance d is defined (i.e., differing from the ApEn method) as the normal Euclidian distance

$$d[u(i), u(j)] = \left(\sum_{k=1}^m |u(i;k) - u(j;k)|^2 \right)^{1/2}. \quad (2.24)$$

Next, we calculate the mean of the quantities $C_i^m(r)$ over all vectors, from which we compute the so-called correlation integral

$$C^m(r) = \frac{1}{N - m + 1} \sum_{i=1}^{N-m+1} C_i^m(r). \quad (2.25)$$

CD is defined as a limit

$$\text{CD}(m) = \lim_{r \rightarrow 0} \lim_{N \rightarrow \infty} \frac{\log C^m(r)}{\log r}. \quad (2.26)$$

In practice, with limited data sets, these limits cannot be calculated with certainty and therefore the CD is defined as the slope of the regression line calculated from a log–log representation and over a range with the required linearity.

When calculating CD, the embedding dimension m must be selected so that it is at least $2D$, where D is the dimension of the system under study, that is, the number of real dynamical variables. In order for the correlation integral to describe the attractor accurately, the number of data points should exceed 10^m . For example, when studying the blood pressure regulation system, we may assume that the number of dynamical variables is >4 , which means that the time series must be very long. In addition, it is nearly impossible to find such a range of the distance r , in which $\log C^m(r)$ changes linearly as a function of $\log r$, because of the noise contained in the data and non-stationarity of the data. Due to these limitations, the calculation of the correct CD for biosignals is computationally not easily achieved. Despite this fact, computation of the correlation dimension may still be useful. Promising results have been achieved by using $m = 20$ and by searching for the mean slope within $0.01 < C^m(r) < 0.1$. The quantity calculated in the above fashion without forgetting the aforementioned limitations is called the *modified correlation dimension*. This quantity cannot accurately define the real dimension of the system, but nevertheless, it does give a measure of the complexity of the system, that is, when CD increases, the system becomes more complex.

2.5.3.2 Pointwise Correlation Dimension

Pointwise correlation dimension (CDi) is defined in a very similar way compared to CD, but instead of labeling the time series with a single value, it is calculated as a function of time (Farmer et al., 1983; Mayer-Kress et al., 1988). This gives us the possibility of evaluating changes in the system characteristics as a function of time, which is very important in non-stationary cases. CDi is sometimes referred to as D2i.

When searching for the regression line, we must once again select the range in which the relation is linear and use a high enough embedding dimension value. When calculating the CDi, we can set $m = 20$ (similar to computing the CD above) and select the area $0.01 < \text{CDi}(r) < 0.1$. In addition, we must note that even though CDi is calculated at each point and it can therefore in principle follow changes in data, the calculation of CDi at any point requires its calculation at all other points. For this reason, CDi is not applicable to non-stationary time series. Thus, in practice, it is advisable to use an additional condition that states that when calculating the regression line at each point in a log–log representation, the correlation factor of the achieved line must exceed a certain limit (e.g., 0.8), and if this criterion is not fulfilled, the CDi value at the point in question is not reliable.

2.5.3.3 Dispersion Analysis

Dimension analysis of a time series may also be performed by studying the curve describing the time series itself rather than the dynamical system behind the signal. This approach

toward analyzing RR intervals is similar to image analysis. Because complex behavior of the dynamical system manifests itself in complicated patterns in the measured time series, a study of the curve's fractal structure will also give information regarding the system itself.

In dispersion-based analysis, we first calculate from the time series, the standard deviation

$$SD(1) = \frac{1}{N} \sqrt{N \sum_{i=1}^N x^2(i) - \left(\sum_{i=1}^N x(i) \right)^2}, \quad (2.27)$$

where $x(i)$ is the time series having N data points. Next, we compute the mean of two consecutive data points, (for the entire time series) resulting in a new time series of $N/2$ data points. For this new time series, we again calculate the standard deviation $SD(2)$. This is continued with group sizes 4, 16, 32 and so on until there are less than 4 data points left in the time series. By repeating the above process, we have a series of standard deviation values $SD(m)$. When we plot $\log SD(m)$ as a function of $\log m$, a line can be plotted through the points if the original time series curve was fractal. For this fractal object, the dimension is $FD-DA = 1 - \text{slope of the line}$ (Bassingthwaite and Raymond, 1995; Yum et al., 1999). Fractal dimension defined in this way can have values between 1 and 1.5, where 1 represents the case of a steady-state signal and 1.5 represents maximal fractal characteristics.

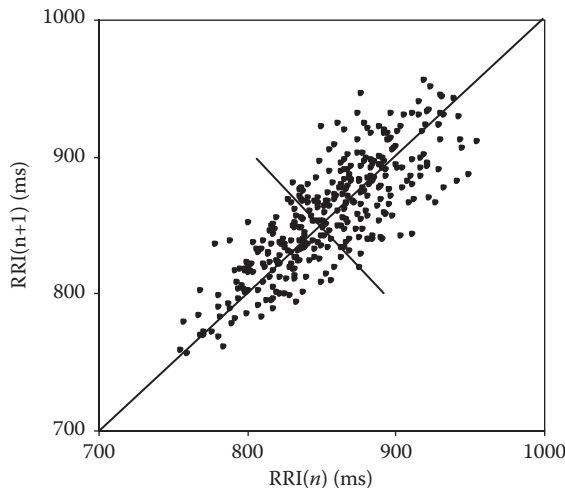
If the curve under study is not purely fractal, that is, it contains a sizeable amount of noise, the $SD(m)$ values do not exactly fit a line in log-log representation. For automated analysis when this line is not visually verified, one can set a minimal correlation of 0.8 as a measure of linearity.

2.5.4 Return Map

Dynamical systems are usually described by a group of differential equations. If the variables get values only at specific discrete moments in time, as is the case with the RR interval time series, the differential equations can be replaced with discrete equations, for example,

$$\begin{aligned} x_{i+1} &= F(x_i, y_i, z_i, \dots) \\ y_{i+1} &= G(x_i, y_i, z_i, \dots), \\ z_{i+1} &= H(x_i, y_i, z_i, \dots) \\ &\vdots \end{aligned} \quad (2.28)$$

where x, y, z and so on are dynamical variables of the system and F, G, H, \dots are functions that define the dynamics. Usually, these functions are not known, but we may try to solve for them by examining the measured time series. If there is only a single variable, the equation is expressed in a simpler form:

**FIGURE 2.11**

A return map made from an RR interval time series. Standard deviation along the diagonal (SD_2) = 5 ms, standard deviation perpendicular to the diagonal (SD_1) = 18 ms.

$$x_{i+1} = F(x_i). \quad (2.29)$$

Because this expression binds the new value x_{i+1} of the variable to its predecessor value x_i , we can solve function F in principle, by pairing successive values of the time series, (x_i, x_{i+1}) for $i = 1$ to $N - 1$, and plotting them on a two-dimensional graph. This kind of a graph is called a return map.* If the dynamics of x is wholly determined by function F and there are enough data points, the method should reveal the shape of the function F .

If the dynamical system behind the time series is not one dimensional, suggesting that more than one variable has an impact on the system, a return map formed on the basis of a single measured variable naturally cannot solve functions F , G and so on. Even in such cases, a single variable return map may prove to be useful, although it is a certain type of projection of the multidimensional system into a single dimension. Figure 2.11 shows the return map of an RR interval time series. The points are typically scattered to form an ellipsoid but can also form complex structures. When the return map is an ellipsoid, it can be characterized by two quantities: the SD in the direction of the diagonal SD_2 and the SD in a direction perpendicular to SD_2 , i.e., SD_1^{\dagger} (Huikuri et al., 1996; Woo et al., 1994). These deviations are, by nature, measures of variability, since they quantify the movement of the system in a phase space. However, when the return map has a complex shape, above parameters do not describe the variability very well.

* This is also called Poincaré or Lorenz plot or map.

[†] For RR interval, SD_1 is the same as RMSSD $\sqrt{2}$.

2.5.5 Other Approaches

2.5.5.1 Stationarity Test

An example of a simple stationarity test that mainly measures changes in the baseline signal is as follows: the signal is divided into segments of suitable length and for each segment, the signal average is calculated. When SD of these averages is divided by the SD of complete signal, we get a measure of stationarity (Palazzolo et al., 1998). This measure is small if the signal is stationary. The length of the segment should be chosen so that it is not too long in order for the local changes to be detectable, but it cannot be too short either in order to prevent the averages of the segments from varying too much. For an RR interval time series, a good choice is to use 20 beats/segment. If the measure is < 0.3 , the signal can be considered to be reasonably stationary.

2.5.5.2 Symbolic Dynamics

The basic idea of this method is to characterize the original time series with a much simpler and coarser symbolic notation which, however, retains the essential dynamic characteristics of the original time series. This is done by converting the time series into a string of symbols. By this, we reduce the study of dynamics into handling of a symbol string. Naturally we lose most of the information contained in the original time series, but nevertheless, we retain key dynamical features, in a *coarse-grained form* (Voss et al., 1995, 1996; Palazzolo et al., 1998).

The conversion of a time series into a symbol string may be done using several methods. One of them is described in Figure 2.12. The signal is divided into two or more value ranges, depending on how many symbols we wish to utilize. Value ranges may be absolute bands or based on signal averages or SD. For example, if we have four different symbols, we may use the following bands:

- A signal \leq average – SD
- B average – SD $<$ signal \leq average
- C average $<$ signal \leq average + SD
- D signal $>$ average + SD

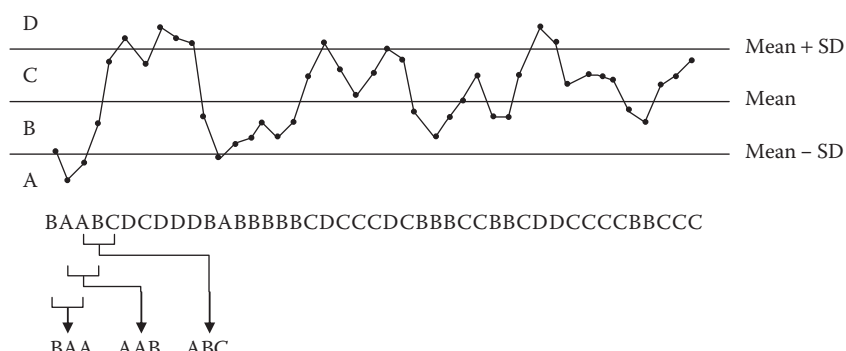


FIGURE 2.12

Conversion of the time series into a symbol row and grouping of the symbol row into words.

After the bands have been selected, the time series can be converted into a symbol string. The next step involves grouping the symbols in the string into *words*. A word is always formed by stepping forward one step in the symbol string. If we choose a word length of 3 and we have 4 different symbols, we get altogether $4 \times 4 \times 4 = 64$ different words. Each word corresponds to a specific graphical representation, which has at least a rough connection to the original dynamics. Different words do not have same probability because HRV dynamics favors certain words. The distribution of the words can thus be interpreted as a probability distribution. The shape of the distribution may itself act as a basis of further analysis, but it is also possible to measure the order related to the distribution in the terms of entropy. The simplest such measure is Shannon's entropy.

2.5.5.3 Multifractal Analysis

A monofractal signal can be described using just one scaling exponent α or Hurst exponent $h = \alpha - 1$, and in these situations, DFA, for example, is a valid method. If a signal is *multifractal*, a set or continuum of Hurst exponents is needed corresponding to a generalized fractal dimension $D(h)$ (Ivanov et al., 1999; Amaral et al., 2001). Multifractal analysis is based on the wavelet transform (Equation 2.11) and the scaling properties of its local maximums (see computational details in Muzy et al., 1991). As a result, we get the fractal dimension as a function of the Hurst exponent.

A typical multifractal analysis of an RR interval time series of 25,000 data points of a healthy subject and a CHF subject is shown in Figure 2.13. In the healthy subject, $D(h)$ has a peak at $h = 0.1$ ($\alpha = 1.1$), and in the CHF subject, $D(h)$ has a peak at $h = 0.2$ ($\alpha = 1.1$). Thus, there is only a minor difference, and both cases resemble a $1/f$ type of dynamics (see Table 2.1). However, $D(h)$ of the CHF subject has a very narrow span in h , corresponding almost to monofractal behavior, but the healthy subject has very wide $D(h)$, indicating true multifractal dynamics. This result clearly reflects the common belief that the complexity of the system decreases as heart rate control degenerates.

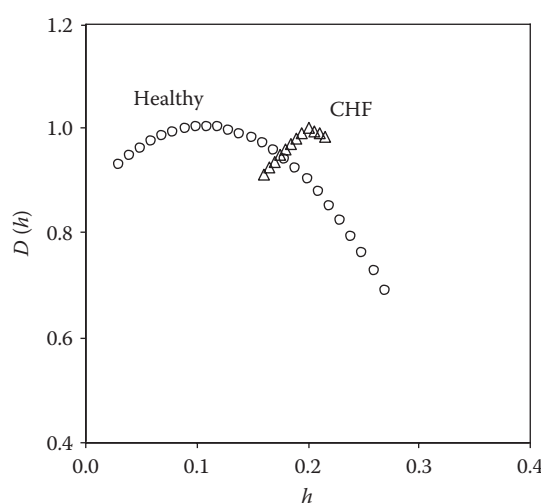


FIGURE 2.13
Fractal dimension $D(h)$ as a function of Hurst exponent h .

2.5.5.4 Stochastic Modeling

The unpredictable portion of the heart rate fluctuation can be due to chaotic dynamics, but there is an alternative explanation: the system includes a real stochastic component. The basic idea behind stochastic modeling is that the unpredictable component is not a perturbation but an essential part of the dynamical behavior of the system. The source of this true noise can be physiological, or it may be a reflection of external disturbances. If the system is truly stochastic, it cannot be described by a deterministic model; rather a stochastic one is needed. Many stochastic systems can be described by the *Langevin* equation

$$\frac{dX(t)}{dt} = g(X(t)) + h(X(t))\Gamma(t), \quad (2.30)$$

where $X(t)$ is the state of the system at moment t , and functions g and h represent the deterministic and stochastic parts of the time evolution. $\Gamma(t)$ is the uncorrelated white noise with zero mean and Gaussian distribution. It has been shown that the *difference version* of Equation 2.30,

$$X(t+\tau) = X(t) + g(X(t)) + h(X(t))\Gamma(t), \quad (2.31)$$

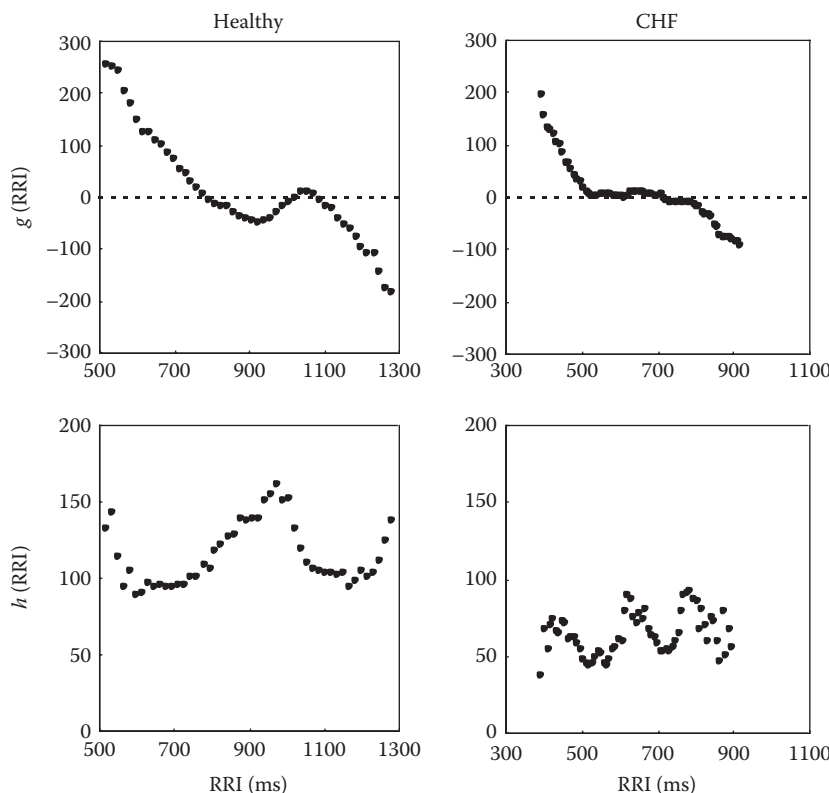
where τ is a finite delay parameter (2–20 min), can model the long-term RR interval time series (Kuusela, 2004; Kuusela et al., 2003). The control functions g and h can be extracted from the data by computing conditional probability distributions. In practice, 50,000–100,000 data points, that is, 12–24 h of RR intervals, are needed in order to determine these distributions reliably. Results from an analysis of 24 h recordings of RR interval are shown in Figure 2.14. At small (large) RR interval values, the deterministic part g is clearly positive (negative); this guarantees that the RR interval is kept within certain limits.* In the case of the healthy subject, typical g function has three zero-crossings (two stable fixed points and one unstable fixed point†) in the middle, but with the CHF subject, g function is flat, indicating a less complex dynamical control. The stochastic parts h have a complicated structure in both cases, but the mean level of the h function is smaller in the CHF subject, which can be interpreted as a lower stochasticity of the system.

2.6 Conclusions

Heart rate fluctuations can be analyzed using many different methods and approaches. No single method described here is clearly superior to other techniques, and therefore, it

* When the RR interval is small, the g function and also the derivative in Equation 2.30 are positive; thus, the RR interval increases. Similarly, when the RR interval is large, the g function and the derivative are negative; thus, the RR interval decreases.

† If we omit the stochastic part in Equation 2.30, the zeros of the g function correspond to the fixed points of the system. At the fixed points, the derivative is zero and the system has no tendency to change. Fixed points can be either stable and attract all nearby states or unstable and repel nearby states.

**FIGURE 2.14**

The deterministic control function g and the stochastic control function h for healthy and CHF subjects.

is recommended that researchers use several techniques in combination. The physiological interpretation of results is often difficult, especially in the case of non-linear methods and further investigation is needed. However, the time series analysis of RR interval data has proven to be useful and it has already gained significant clinical relevance. It would be very useful to agree on common rules or guidelines about when to use each method, the length of the time series needed, normative values and the kind of editing or filtering operations, so that the results from different laboratories can be compared.

Abbreviations

| | |
|------|---------------------------------|
| AF | Atrial fibrillation |
| AIC | Akaike information criteria |
| ApEn | Approximate entropy |
| AR | Autoregressive |
| CD | Correlation dimension |
| CDi | Pointwise correlation dimension |
| CDM | Complex demodulation |

| | |
|--------|---|
| CHF | Congestive heart failure |
| CWT | Continuous wavelet transform |
| DFA | Detrended fluctuation analysis |
| FFT | Fast fourier transform |
| FPE | Final prediction error |
| HF | High frequency |
| HRV | Heart rate variability |
| LF | Low frequency |
| MDL | Minimum description length |
| MSE | Multiscale entropy |
| NN50 | Number of pairs of adjacent RR intervals differing by more than 50 ms |
| pNN50 | Ratio of NN50 count to the count of all RR intervals expressed as a percentage |
| PSD | Power spectral density |
| RMSSD | Root mean square of successive differences of RR intervals |
| SampEn | Sample entropy |
| SD | Standard deviation |
| SDA | Selective discrete Fourier transform algorithm |
| SDANN | Normal-to-normal standard deviation of all 5 minute segments averaged over 24 hours |
| SDNN | Normal-to-normal standard deviation |
| STFT | Short-time Fourier transform |
| TP | Total power |
| ULF | Ultralow frequency |
| VLF | Very low frequency |
| WFT | Windowed fourier transform |
| WVD | Wigner–Ville distribution |

References

- Akaike H. (1969) Power spectrum estimation through autoregressive model fitting. *Ana. Inst. Stat. Math.* 21:407–419.
- Amaral LAN, Ivanov Ch, Aoyagi N, Hidaka I, Tomono S, Goldberger AL, Stanley HE, Yamamoto Y. (2001) Behavioral-independent features of complex heartbeat dynamics. *Phys. Rev. Lett.* 86:6026–6029.
- Bassingthwaite JB, Raymond GM. (1995) Evaluation of the dispersional analysis method for fractal time series. *Ann. Biomed. Eng.* 23:491–505.
- Bettermann H, van Leeuwen P. (1998) Evidence of phase transitions in heart period dynamics. *Biol. Cybern.* 78:63–70.
- Bianchi AM, Mainardi L, Petrucci E, Signorini MG, Mainardi M, Cerutti S. (1997) Time-variant power spectrum analysis for the detection of transient episodes in HRV signal. *IEEE Trans. Biomed. Eng.* 40:135–144.
- Bigger JT, Steinman RC, Rolnitzky LM, Fleiss JL, Albrecht P, Cohen RJ. (1996) Power law behaviour of RR-interval variability on healthy middle-aged persons, patients with recent acute myocardial infarction, and patients with heart transplants. *Circulation.* 93:2142–2151.

- Claasen TACM, Mecklenbräuker WFG. (1980a) The Wigner distribution—A tool for time-frequency signal analysis. Part I: Continuous-time signals. *Philips J. Res.* 35:217–250.
- Claasen TACM, Mecklenbräuker WFG. (1980b) The Wigner distribution a tool for time-frequency signal analysis. Part II: Discrete-time signals. *Philips J. Res.* 35:276–300.
- Costa M, Goldberger AL, Peng C-K. (2002) Multiscale entropy analysis of complex physiologic time series. *Phys. Rev. Lett.* 89:068102 1–4.
- Costa M, Goldberger AL, Peng C-K. (2005) Multiscale entropy analysis of biological signals. *Phys. Rev. E* 71:021906 1–18.
- Cysarz D, Bettermann H, Van Leeuwen P. (2000) Entropies of short binary sequences in heart period dynamics. *Am. J. Physiol.* 278(6):H2163–H2172.
- Farmer JD, Ott E, Yorke JA. (1983) Dimension of chaotic attractors. *Physica*. D7:153–180.
- Figliola A, Serrano E. (1997) Analysis of physiological time series using wavelet transforms. *IEEE Eng. Med. Biol.* 16:74–79.
- Grassberger P, Procaccia I. (1983) Characterization of strange attractors. *Phys. Rev. Lett.* 31:346–349.
- Huikuri HV, Seppänen T, Koistinen MJ, Airaksinen KEJ, Ikäheimo MJ, Castellanos A, Myerburg RJ. (1996) Abnormalities in beat-to-beat dynamics of heart rate before the spontaneous onset of life-threatening ventricular tachyarrhythmias in patients with prior myocardial infarction. *Circulation*. 93:1836–1844.
- Hyung-Ill C, Williams WJ. (1989) Improved time-frequency representation of multicomponent signals using exponential kernels. *IEEE Trans. Acoust. Speech. Signal Process.* 37:862–871.
- Ivanov Ch, Amaral LAN, Goldberger AL, Havlin S, Rosenblum MG, Struzik ZR, Stanley HE. (1999) Multifractality in human heartbeat dynamics. *Nature*. 399:461–465.
- Iyengar N, Peng C-K, Morin R, Goldberger AL, Lipsitz LA. (1996) Age-related alterations in the fractal scaling of cardiac interbeat interval dynamics. *Am. J. Physiol. Regul. Integr. Comp. Physiol.* 271:R1078–R1084.
- Kantz H, Schreiber T. (1995) Dimension estimates and physiological data. *Chaos*. 5:143–154.
- Kay SM, Marple SL. (1981) Spectrum analysis: A modern perspective. *Proc. IEEE*. 69:1380–1418.
- Keselbrener L, Akselrod S. (1996) Selective discrete Fourier transform algorithm for time-frequency analysis: Method and application on simulated and cardiovascular signals. *IEEE Trans. Biomed. Eng.* 43:789–802.
- Kim SY, Euler DE. (1997) Baroreflex sensitivity assessed by complex demodulation of cardiovascular variability. *Hypertension*. 29:1119–1125.
- Kuusela TA. (2004) Stochastic heart-rate model can reveal pathologic cardiac dynamics. *Phys. Rev. E* 69:031916 1–7.
- Kuusela TA, Shepherd T, Hietarinta J. (2003) Stochastic model for heart rate fluctuations. *Phys. Rev. E* 67:061904 1–7.
- Marple SL. (1987) *Digital Spectral Analysis with Applications*. Englewood Cliffs, NJ, Prentice-Hall.
- Mayer-Kress G, Yates FE, Benton L, Keidel M, Tirsch W, Pöppel SJ, Geist K. (1988) Dimensional analysis of nonlinear oscillations in brain, heart, and muscle. *Math. Biosci.* 90:155–182.
- Muzy JF, Bacry E, Arneodo A. (1991) Wavelets and multifractal formalism for singular signals: Application to turbulence data. *Phys. Rev. Lett.* 67:3515–3518.
- Novak P, Novak V. (1993) Time/frequency mapping of the heart rate, blood pressure and respiratory signals. *Med. Biol. Eng. Comput.* 31:103–110.
- Palazzolo JA, Estafanous FG, Murray PA. (1998) Entropy measures of heart rate variation in conscious dogs. *Am. J. Physiol. Heart Circ. Physiol.* 274:H1099–H1105.
- Partzen E. (1974) Some recent advances in time series modeling. *IEEE Trans. Automat. Contr.* 19:723–730.
- Peng C-K, Mietus J, Hausdorff JM, Havlin S, Stanley HE, Goldberger AL. (1993) Long-range anticorrelations and non-gaussian behaviour of the heartbeat. *Phys. Rev. Lett.* 70:1343–1346.
- Peng C-K, Havlin S, Stanley HE, Goldberger AL. (1995) Quantification of scaling exponents and crossover phenomena in nonstationary heartbeat time series. *Chaos*. 5:82–87.
- Pincus SM, Goldberger AL. (1994) Physiological time-series analysis: What does regularity quantify? *Am. J. Physiol. Heart Circ. Physiol.* 266:H1643–H1656.

- Pincus S. (1995) Approximate entropy (ApEn) as a complexity measure. *Chaos*. 5:110–117.
- Richman JS, Moorman JR. (2000) Physiological time-series analysis using approximate entropy and sample entropy. *Am. J. Physiol. Heart Circ. Physiol.* 278:H2039–H2049.
- Rissanen J. (1983) A universal prior for the integers and estimation by minimum description length. *Ann. Stat.* 11:417–431.
- Voss A, Kurths J, Kleiner HJ, Witt A, Wessel N. (1995) Improved analysis of heart rate variability by methods of nonlinear dynamics. *J. Electrocardiol.* 28:81–88.
- Voss A, Kurths J, Kleiner HJ, Witt A, Wessel N, Saparin P, Osterziel KJ, Schurath R, Dietz R. (1996) The application of methods on non-linear dynamics for the improved and predictive recognition of patients threatened by sudden cardiac death. *Cardiovasc. Res.* 31:419–433.
- Wiklund U, Akay M, Niklasson U. (1997) Short-term analysis of heart-rate variability by adapted wavelet transforms. *IEEE Eng. Med. Biol.* 16:113–118.
- Woo MA, Stevenson WG, Moser DK, Middlekauf HR. (1994) Complex heart rate variability and serum norepinephrine levels in patients with advanced heart failure. *J. Am. Coll. Cardiol.* 23:565–569.
- Yum MK, Kim NS, Oh JW, Kim CR, Lee JW, Kim SK, Noh CI, Choi JY, Yun YS. (1999) Non-linear cardiac dynamics and morning dip: An unsound circadian rhythm. *Clin. Physiol.* 19:56–67.

Stochastic model for heart-rate fluctuations

Tom Kuusela,* Tony Shepherd, and Jarmo Hietarinta

Department of Physics, University of Turku, 20014 Turku, Finland

(Received 7 February 2003; published 13 June 2003)

A normal human heart rate shows complex fluctuations in time, which is natural, because the heart rate is controlled by a large number of different feedback control loops. These unpredictable fluctuations have been shown to display fractal dynamics, long-term correlations, and $1/f$ noise. These characterizations are statistical and they have been widely studied and used, but much less is known about the detailed time evolution (dynamics) of the heart-rate control mechanism. Here we show that a simple one-dimensional Langevin-type stochastic difference equation can accurately model the heart-rate fluctuations in a time scale from minutes to hours. The model consists of a deterministic nonlinear part and a stochastic part typical to Gaussian noise, and both parts can be directly determined from the measured heart-rate data. Studies of 27 healthy subjects reveal that in most cases, the deterministic part has a form typically seen in bistable systems: there are two stable fixed points and one unstable one.

DOI: 10.1103/PhysRevE.67.061904

PACS number(s): 87.19.Hh, 02.50.Ey

I. INTRODUCTION

Various methods and models have been used in attempts to characterize the dynamics of the heart-rate control mechanism. For short time periods and under stationary conditions, there are successful models of heart-rate and blood pressure regulation [1,2], but the characterization of a long-term behavior has been a very difficult problem. Some models have been introduced in order to explain long-term fluctuations, but usually they can only describe well-controlled *in vitro* experiments, or the models depend on a large number of parameters, which cannot be easily determined from experimental data [3]. Furthermore, these models can predict only global statistical features such as scaling properties of power spectrum and correlations [4], and provide us very little information about the details of the time evolution.

Many features can be extracted from long time series of heart-rate measurements, quantities such as entropy measures [5–11], correlation dimension [12–17], detrended fluctuations [18–20], fractal dimensions [10,21–23], spectrum power-law exponents [20,24], and symbolic dynamics complexity [25–27], but these are all purely statistical characterizations and as such cannot provide us a mathematical model of heart-rate dynamics, not even a simple one. However, some of these statistical methods do characterize the complexity of the dynamics underlying the time series [28], or are directly related to their fractal or chaotic features. A mathematical analysis of many physiological rhythms, including long-term heart-rate fluctuations, has revealed that they are generated by processes that must be nonlinear, since linear systems cannot produce such a complex behavior [29]. Nonlinear, purely deterministic models can display chaotic dynamics and generate apparently unpredictable oscillations, but, in practice, it has not yet been possible to extract such models from real noisy experimental data. It is also possible that the underlying system is stochastic, i.e., the time evolution of the system is subject to a noise source. (This kind of

dynamical noise is different from measurement noise, which is mostly generated in the experimental apparatus.) In any case, there is an increasing evidence that noise, originated either from the system itself or as a reflection of external influences, is actually an integral part of the dynamics of biological systems [30–32].

A typical *R-R* interval recording is shown in Fig. 1. The time series is generated by recording a 24-h electrocardiogram and detecting the *R*-peak from each heartbeat, the *R-R* interval is the time difference between two consecutive *R*-peaks. In the upper panel of Fig. 1, we have the *R-R* interval time series for 6 h. We can see sections where the oscillations are rather regular, but there are also abrupt changes. In the lower panel of Fig. 1, we have enlarged a part of the time series of about 50 min, and also in this time range we can see apparently random oscillations with rapid changes.

It is well known that most short-time fluctuations of heart rate are generated by respiration (periods typically in the couple of seconds range) and blood pressure regulation (so

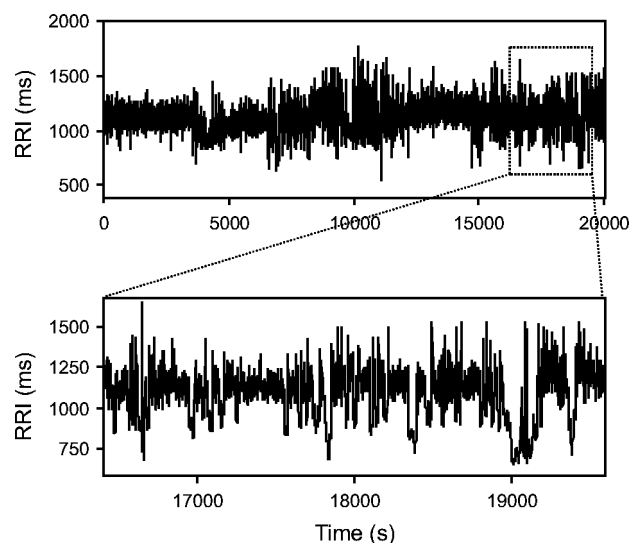


FIG. 1. Typical *R-R* interval time series recorded at night.

*Electronic address: tom.kuusela@utu.fi

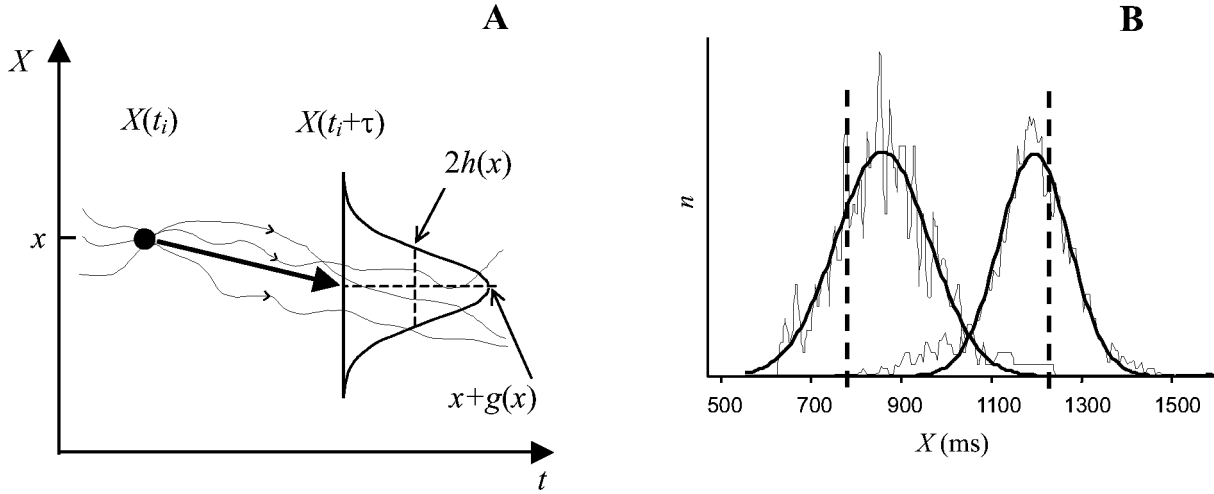


FIG. 2. Schematic presentation of the method for analyzing the stochastic time series and calculating the deterministic and stochastic parts of the dynamics [part (a)]. Whenever the trajectory of the system passes near a certain point x in the state space, i.e., $X(t_i) \approx x$, the future value $X(t_i + \tau)$ of the trajectory is recorded. The distribution of these values is fitted by a Gaussian function with the mean $x + g(x)$ and deviation $h(x)$, cf. Eq. (2). This is repeated for all x values. On the right there are two typical examples of the distribution of future values, the initial x values are marked with dashed vertical bars and the fitted Gaussian curves with a thick line [part (b)].

called Meyer waves with periods of about 10 sec [33]). In the following, we are not interested in these fast rhythms (which can be analyzed quite well using linear or semilinear models), but rather in time scales from minutes to hours. We will show that in this time range, the dynamics of the heart-rate fluctuations can be well described by a one-dimensional Langevin-type difference equation. This equation contains a deterministic part and an additive Gaussian noise, and we have found that it works well when the delay parameter in the equation is in the range of 2–20 min.

II. THE MODEL

An important and wide class of dynamic systems can be described by the Langevin differential equation [34,35]

$$\frac{dX(t)}{dt} = g(X(t), t) + h(X(t), t)\Gamma(t). \quad (1)$$

Here, $X(t)$ represents the state of the system at time t , the function g gives the nonlinear deterministic change, and, in the last term, h is the amplitude of the stochastic contribution and $\Gamma(t)$ stands for uncorrelated white noise with a vanishing mean. These kinds of stochastic differential equations always need an interpretation rule for the noise term, normally one uses the Ito interpretation [36]. In general, the functions g and h could depend explicitly on time t . Equation (1) can be easily generalized to higher dimensions. We will now show that the long-term behavior of the heart-rate can be modeled using a *difference* version of the Langevin equation [34]

$$X(t + \tau) = X(t) + g(X(t); \tau) + h(X(t); \tau)\Gamma(t). \quad (2)$$

Here $X(t)$ again represents the state of the system, which in this case is the R - R interval, at time t , and τ is the time delay. If arbitrary small delays τ are possible, then one can take the

limit $\tau \rightarrow 0$ and get the differential equation (1) [if the τ dependence is given by $g(X(t); \tau) \approx \tau g(X(t))$], but in the present case it will turn out that there is a minimum τ for which model (2) seems to be valid. We assume that g and h do not have an explicit time dependence, but they may depend on the delay τ . It is convenient to extract the term $X(t)$ in the deterministic part, as is done in Eq. (2), then a nonzero $g(X(t); \tau)$ stands for changes in the state of the system. An essential feature of models of the above type is that for time evolution, we only need to know the state at one given moment and not its evolution in the past, i.e., they are Markovian [34,37].

The computational problem is now to determine the functions g and h from measured time series and to verify that the description using Eq. (2) is accurate. The principle of the method is very simple [38,39]: at every time t_i when the trajectory of the system meets an arbitrary but fixed point x in state space, we look at the future state of the system at time $t_i + \tau$. The set of these future values (for a chosen x and τ) has a distribution in the state space and from this distribution we can determine the deterministic part $g(x)$ and the stochastic part $h(x)$, see Fig. 2(a). In practice, we first divide the range of the dynamical variable X into equal boxes. By scanning the whole measured time series we check when X is inside a given box x , i.e., $|X(t_i) - x| \leq \Delta x$, where x is the middle value of the box and Δx is the half-width of the box. When X is found on the box, we look at the future value of the variable, $X(t_i + \tau)$, where τ is the fixed delay parameter. Since the trajectory of the system passes each box several times, we can calculate the distribution of the future values $X(t_i + \tau)$ for each box x . If we assume that the noise is Gaussian, we can fit a Gaussian function on each distribution, and as a result we get the mean and the deviation parameters for each x ; the mean of this distribution is equal to $x + g(x)$ and the deviation is equal to $h(x)$ [40,41]. A typical case is given in Fig. 2(b), and it shows that the distribution is

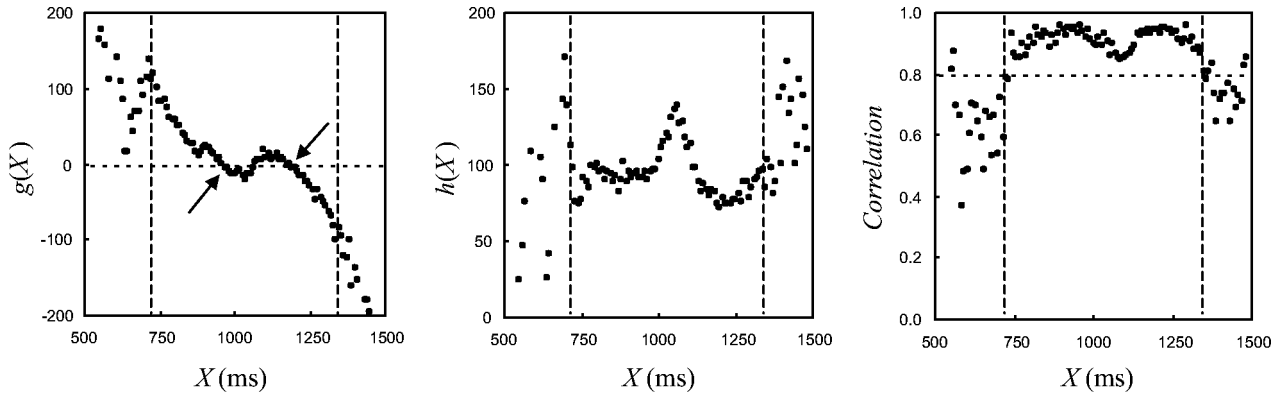


FIG. 3. Typical results derived from R - R interval time series using time delay $\tau = 500$. We have shown the deterministic part $g(X)$ (the left panel), the stochastic part $h(X)$ (the middle panel), and the correlation coefficient of the distribution (the right panel) as a function of the dynamical variable X . The range corresponding to the correlation threshold level of 0.8 is marked with the vertical lines.

actually very well described by Gaussian noise (the correlation is better than 0.95; the correlation is calculated as $\sqrt{1 - S_{res}/S_{tot}}$, where S_{res} is the sum of the squared residuals and S_{tot} is the variance). From the given data, we can in this way determine the functions $g(X)$ and $h(X)$ needed in the stochastic model (2). It should be noted that we can calculate only the absolute value of $h(X)$, since the deviation parameter found from the fitted Gaussian function is in a squared form.

In our analysis we have used R - R interval time series of 22–24 h, corresponding to 80.000–100.000 data points. Our data is actually interval data, i.e., it consists of a sequence of R - R interval values. It is then convenient to count the delay in our analysis in terms of heart beats rather than seconds, i.e., we have not used cumulative time as time variable but the beat index. Since the R - R interval values vary a lot within the used delay range, the beat index actually gives a delay as if computed with the average beat rate. We have tested both methods and found only minor differences between them (in the details of the functions g and h). We will show later that the functional forms of g and h are quite insensitive on the time delay, and since this holds for both methods we will use the more convenient beat index.

III. RESULTS

A. A typical case

In Fig. 3, we have presented results obtained for a particular case using the method described earlier. The value of the delay parameter τ was 500 beats, and the number of boxes used to construct local distributions was 150. Distributions were fitted using a Gaussian function. The $g(X)$ function, the deterministic part of the system, is displayed on the left panel in Fig. 3. It has a very clear and simple functional form (between the vertical lines) which is typical for systems exhibiting a bistable behavior [34,42]. The function crosses the zero line three times; these crossings are the fixed points of the system. The fixed points marked with arrows are stable: without any noise term these points attract all nearby states because the control function $g(X)$ is locally decreasing. The

middle fixed point is repulsive. Due to the stochastic part, the system has a tendency to jump between the stable points if the amplitude of the noise is high enough. Far away from the stable points, $g(X)$ increases or decreases strongly and this forces the system rapidly back to oscillate around the stable points. The amplitude of the stochastic part of the system, function $h(X)$, is almost constant, except between the stable points where it has a clear maximum (the middle panel in Fig. 3). One interpretation is that the system has a larger inherent freedom to oscillate randomly when the trajectory is between the stable points, but outside this range the character of the system is more deterministic. From the physiological point of view, this kind of dynamics can be useful since it lets the R - R interval to wander most of the time but prevents it from escaping too far away from the normal range. On the right panel in Fig. 3, we have shown the correlation coefficient of each local distribution. Most of the time, the correlation is remarkably high, about 0.85–0.95; but near the largest and the smallest X values, there are only rather few data points and therefore the corresponding distributions do not have a clear Gaussian shape resulting with lower correlation. The high average correlation value is a clear indication that the noise in this system is really a Gaussian type. We have used the value of 0.8 as a threshold level, and the corresponding range is marked with the vertical lines in Fig. 3.

What is remarkable in this description is that the functional forms of $g(X)$ and $h(X)$ are fairly independent of the delay parameter τ in a rather extensive delay range, typically 100–1000 beats (corresponding to 2–20 min). In Fig. 4, we have plotted the functions $g(X)$ and $h(X)$ for a range of τ values. The g function is practically τ independent, except for the shortest R - R intervals, where some cumulative effects show up. The h function seems to grow very slowly as τ increases. For still smaller delay values, $g(X)$ is more flat and $h(X)$ is more scattered, and for longer delays $g(X)$ is typically a straight line and $h(X)$ is constant. Behavior at these extremes can be easily understood by recalling that when the time scale is small, the heart-rate system is clearly multidimensional—depending directly on blood pressure, respiration, and other rapidly changing physiological

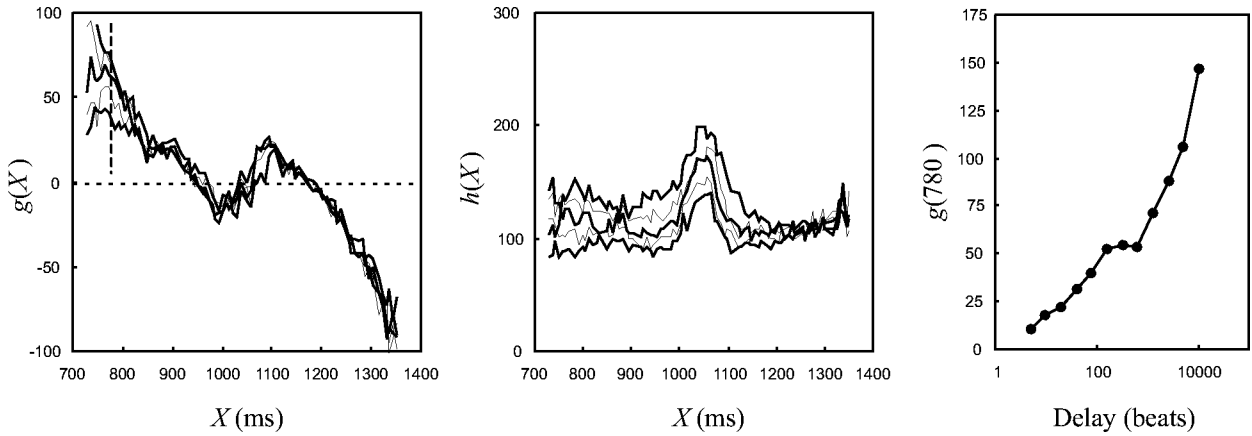


FIG. 4. Examples of the deterministic part $g(X)$ (the left panel) and the stochastic part $h(X)$ (middle panel) calculated with various values of the delay parameter τ : 40 (thick line), 80 (thin line), 160 (thick line), 320 (thin line), and 640 (thick line). The values of the $g(X)$ function at $X = 780$ ms (marked with vertical dashed line in the left panel) are plotted as a function of the delay in the right panel, there is a plateau around a delay of 100–1000 beats.

variables—and our one-dimensional description is no longer valid. On the other hand, if the delay parameter is very large, we cannot reconstruct the local dynamics in terms of local distributions, we just get the global distribution that is independent of dynamics and no longer Gaussian. In the right panel of Fig. 4, we have given the values of the $g(X)$ function at $X = 780$ ms (marked with a vertical dashed line in the left panel) computed with delays of 5–10 240 beats. We can see a plateau in the delay range of 100–1000 beats which means that the $g(X)$ curves for these delays are bundled. In principle, the curves for a delay of 2τ should be obtainable by iterating Eq. (2) with delay τ . Direct numerical calculations of joint probabilities using experimentally determined $g(X)$ (within 100–1000 beats delay range) indicate that $g(X)$ and $h(X)$ do not change significantly in one iteration, mostly because in our case the Gaussian distribution is not so narrow. In general, iterations tend to sharpen the bends in $g(X)$ and this feature is indeed visible in Fig. 4. The small τ dependency of g and h in the range of short R - R intervals can then be interpreted either as the expected result from repeated iterations or as a sign of higher-order dynamics: possibly the heart-rate regulation system is more complex when the system must readjust at a fast heart rate.

B. Variation between subjects

In order to find whether different subjects have any common features in the deterministic and stochastic parts, $g(X)$ and $h(X)$, we analyzed the data from 27 healthy subjects of various age and gender (18 cases from PhysioBank [43] and 9 cases from Kuopio University Hospital). Analyses were done using the same parameter values as in Fig. 3. The deterministic part, the $g(X)$ function, is displayed in Fig. 5 for a set of nine typical cases. The most common form for this function is the bistable type, already shown in Fig. 3, where the $g(X)$ function has three zeros, and 60% of all cases can be classified to this group (cases 1–5 in Fig. 5). The next most common group, 25% of all cases, has a $g(X)$ function with five zeros, a kind of double pitchfork system (cases 6

and 7 in Fig. 5). We also found three cases where the $g(X)$ function seems to have even more zero (case 8 in Fig. 5). Only very few cases could not be clearly classified as bistable or multistable. In these cases, it can be difficult to interpret the results. It is possible that the dynamical variable did not explore the whole state phase, and therefore we can see only part of the $g(X)$ function; case 9 in Fig. 5 is an example of this where the system has only one stable fixed point and no unstable points at all. The stochastic parts [function $h(X)$] are fairly similar: they are almost constant, except that in all cases there are maxima on the R - R interval ranges between the stable fixed points of the deterministic part, as in the example in Fig. 3.

The description given by Eq. (2) contains both a deterministic and a stochastic component. It is important to realize that the stochastic part is not a small perturbation but in fact forms an essential part of the description, furthermore, it is 10–20 times higher than the measurement noise (uncertainty in detecting the position of the R -peak), which is typically only 2–5 ms. One way to compare the deterministic and stochastic components is to note that the size of the bend in the $g(X)$ function is of the order of 30–50 ms, while the average size of the $h(X)$ function is about 70–110 ms, as can be seen in Fig. 3. [The extraction of small details in the $g(X)$ function under such noise is of course possible only because the noise is so cleanly Gaussian.] On the other hand, the distance between the stable fixed points in the $g(X)$ function is of the order of 50–250 ms and, therefore, the probability that the system jumps between stable points is not extremely high, but nevertheless possible. It is also possible that external factors drive the system from one stable point to another, since during night time, the mean R - R interval is typically longer than during day time [although the R - R interval can abruptly jump to the faster rate also during the night, as can be seen on the lower panel in Fig. 1].

C. Same subject at different times

If model (2) were to describe the true heart-rate dynamics, the functions $g(X)$ and $h(X)$ should have some constant

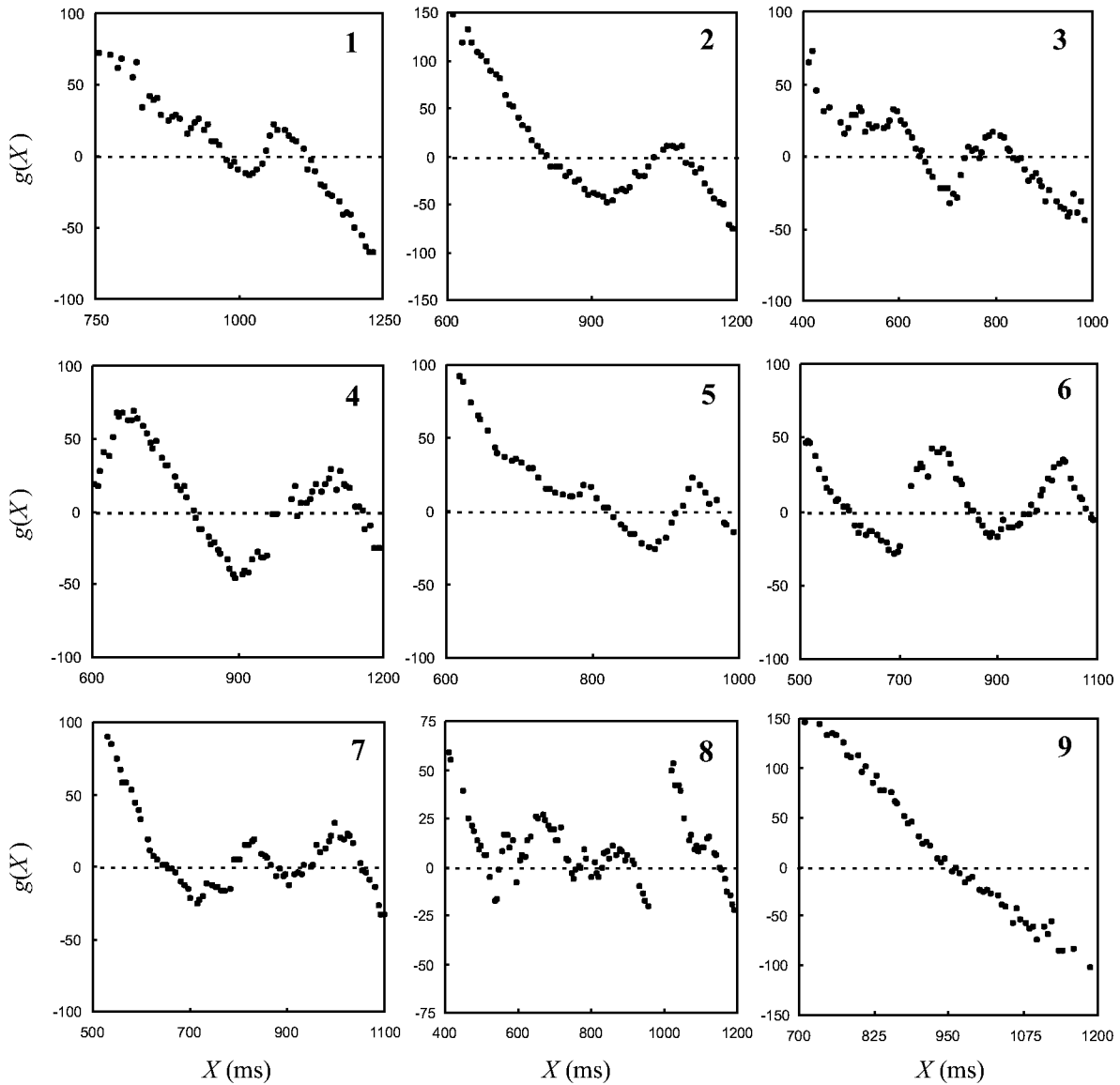


FIG. 5. Typical deterministic functions $g(X)$ derived from different subjects. Cases 1–5 represent the simple bistable situation, cases 6 and 7 have three stable points, case 8 is multistable, and case 9 has only a single stable fixed point.

features specific for each subject. In order to look at this aspect we made two recordings from the same subject within four days, the results are shown in Fig. 6. In general, the deterministic and stochastic parts from different recordings

are remarkably similar, both having clear bistable character. In the R - R interval range of 500–800 ms, the results are almost identical and the only difference seems to be a scaling towards the shorter R - R intervals in the 800–1100 ms range

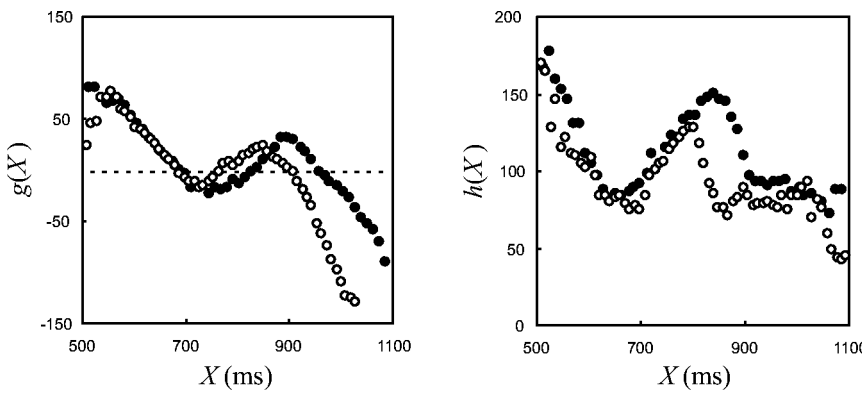


FIG. 6. The deterministic parts $g(X)$ (left panel) and stochastic parts $h(X)$ (right panel) computed from the R - R interval time series recorded from the same subject on different days. The data from the first recording are marked with solid dots and data from the second recording, four days later, with open dots.

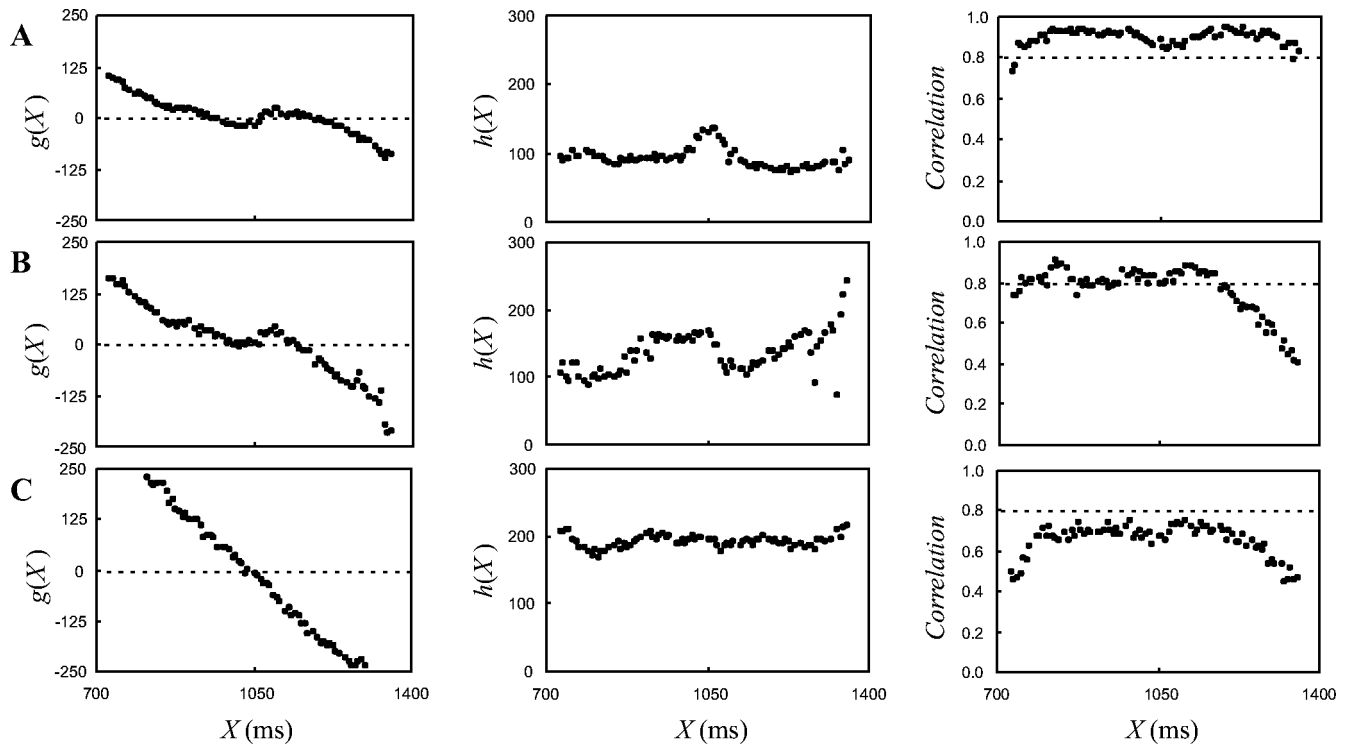


FIG. 7. The deterministic part $g(X)$ (left column), stochastic part $h(X)$ (middle column), and correlation coefficient (right column) for the original data (row A) and for two surrogate versions (rows B and C). For surrogate data, the original data have been shuffled using section sizes of 800 (row B) and 400 (row C) data points.

of the second recording. In the first recording the mean value of the R - R interval calculated over the 24 h period was 781 ms and in the second one 726 ms. Therefore in the second recording the shortest R - R intervals are significantly more frequent and this can affect the analysis results. These deviations could also reflect true changes on the underlying control system: it is well known that there are daily variations on functions of the autonomic nervous system.

D. Surrogate analysis

As a further validity check, we also performed surrogate analysis [44,45] in order to eliminate the possibility that the results are generated just from a peculiar distribution of the R - R intervals imitating real dynamics. For this purpose, the data was shuffled by dividing it into sections of equal size, which were then repositioned randomly. As a result, we get a new time series where the dynamical structure has been partially destroyed depending on the section size. Results of this surrogate analysis are shown in Fig. 7. The top panels display the deterministic $g(X)$ and stochastic $h(X)$ parts of the system and the correlation coefficient without any data shuffling (row A in Fig. 7). On the next row (row B in Fig. 7) we have used sections of 800 data points for shuffling. There are only small changes in the deterministic part, but the correlation has decreased noticeably. When the section size is 400 (row C in Fig. 7), we can no longer see the bistable character in the deterministic part, the stochastic part is flat with higher mean level, and the average level of the correlation coefficient has dropped well below our threshold value 0.8. With still smaller section sizes, the results do not change any

further. In this analysis, we have used the same delay of 500 data points as used previously, and when the section size used in the shuffling process is less than this delay, all dynamical properties disappear, as expected in the case of true time evolution. Therefore, we conclude that our results are derived from the dynamical properties of the heartbeat data, and not from their overall statistical characteristics.

IV. CONCLUSION

Our results indicate that the human heart-rate control dynamics can be accurately modeled with the one-dimensional stochastic difference equation (2), where the time delay parameter is within 2–20 min. Stochasticity is an integral part of the dynamics, and in this delay range the effects of other variables are either embedded into the stochastic part of the system or averaged over time with no net effect. It is remarkable that the form of the control function $g(X)$ is similar from case to case. Their typically bistable character is also well justified on common physiological grounds. From this initial study, we cannot yet identify what kind of dynamical structure is typical for healthy subjects (although our results already indicate that a simple bistable system is most common feature), and therefore the model cannot yet be used directly for clinical work, for this purpose, one needs extensive demographic studies. We can nevertheless speculate that the form of the control function $g(X)$ should provide us some information about the health of the subject. Also, some of the current knowledge based on statistical measures of

heart-rate time series can probably be explained within the framework of our model. Another interesting observation is the importance of the stochastic part; it could be the result of integrating the effects of a more detailed control mechanism over time, but it could also reflect some truly stochastic internal and external influences.

ACKNOWLEDGMENTS

We thank T. Laitinen from Kuopio University Hospital, Department of Clinical Physiology, for providing nine electrocardiogram recordings. This work was partially supported by the Academy of Finland.

-
- [1] H. Seidel, Ph.D. thesis, Berlin Technical University, Berlin, 1998.
 - [2] B.J. ten Voorde, Ph.D. thesis, University of Vrije, Amsterdam, The Netherlands, 1992.
 - [3] L. Glass and M.C. Mackey, *From Clocks to Chaos: The Rhythms of Life* (Princeton University Press, Princeton, 1988).
 - [4] P.C. Ivanov, L.A.N. Amaral, A.L. Goldberger, and H.E. Stanley, *Europhys. Lett.* **43**, 363 (1998).
 - [5] F. Kaspar and H.G. Schuster, *Phys. Rev. A* **36**, 842 (1987).
 - [6] S.M. Pincus and A.L. Goldberger, *Am. J. Physiol.* **266**, H1643 (1995).
 - [7] S. Pincus, *Chaos* **5**, 110 (1995).
 - [8] I.A. Rezek and S.J. Roberts, *IEEE Trans. Biomed. Eng.* **45**, 1186 (1998).
 - [9] J.S. Richman and J.R. Moorman, *Am. J. Physiol.* **278**, H2039 (2000).
 - [10] X.-S. Zhang and R.J. Roy, *Med. Biol. Eng. Comput.* **37**, 327 (1999).
 - [11] H. Bettermann and P. van Leeuwen, *Biol. Cybern.* **78**, 63 (1998).
 - [12] J.D. Farmer, E. Ott, and J.A. Yorke, *Physica D* **7**, 153 (1983).
 - [13] J. Fell, J. Röschke, and C. Schäffner, *Biol. Cybern.* **75**, 85 (1996).
 - [14] P. Grassberger and I. Procaccia, *Phys. Rev. Lett.* **50**, 346 (1983).
 - [15] H. Kantz and T. Schreiber, *Chaos* **5**, 143 (1995).
 - [16] G. Mayer-Kress, F.E. Yates, L. Benton, M. Keidel, W. Tirsch, S.J. Pöppel, and K. Geist, *Math. Biosci.* **90**, 155 (1988).
 - [17] M.-K. Yum, N.S. Kim, J.W. Oh, C.R. Kim, J.W. Lee, S.K. Kim, C.I. Noh, J.Y. Choi, and Y.S. Yun, *Clin. Physiol.* **56**, 56 (1999).
 - [18] C.-K. Peng, J. Mietus, J.M. Hausdorff, S. Havlin, H.E. Stanley, and A.L. Goldberger, *Phys. Rev. Lett.* **70**, 1343 (1993).
 - [19] C.-K. Peng, S. Havlin, H.E. Stanley, and A.L. Goldberger, *Chaos* **5**, 82 (1995).
 - [20] N. Iyengar, C.-K. Peng, R. Morin, A.L. Goldberger, and L.A. Lipsitz, *Am. J. Physiol.* **271**, R1078 (1996).
 - [21] J.B. Bassingthwaite and G.M. Raymond, *Ann. Biomed. Eng.* **23**, 491 (1995).
 - [22] N.P. Chau, X. Chanudet, B. Bauduceau, and P.L.D. Gautier, *Blood Press* **2**, 101 (1993).
 - [23] N.A.J. Gough, *Physiol. Meas.* **14**, 309 (1993).
 - [24] J.T. Bigger, R.C. Steinman, L.M. Rolnizky, J.L. Fleiss, P. Albrecht, and R.J. Cohen, *Circulation* **93**, 2142 (1996).
 - [25] J.A. Palazzolo, F.G. Estafanous, and P.A. Murray, *Am. J. Physiol.* **274**, H1099 (1998).
 - [26] A. Voss, J. Kurths, H.J. Kleiner, A. Witt, and N. Wessel, *J. Electrocardiol.* **28**, 81 (1995).
 - [27] A. Voss, J. Kurths, H.J. Kleiner, A. Witt, N. Wessel, P. Saparin, K.J. Osterziel, R. Schurath, and R. Dietz, *Cardiovasc. Res.* **31**, 419 (1996).
 - [28] T.A. Kuusela, T.T. Jartti, K.U.O. Tahvanainen, and T.J. Kaila, *Am. J. Physiol.* **282**, H773 (2002).
 - [29] L. Glass, *Nature (London)* **410**, 277 (2001).
 - [30] J.J. Collins, T.T. Imhoff, and P. Grigg, *J. Neurophysiol.* **76**, 642 (1996).
 - [31] I. Hidaka, D. Nozaki, and Y. Yamamoto, *Phys. Rev. Lett.* **85**, 3740 (2000).
 - [32] D.J. Mar, C.C. Chow, W. Gerstner, R.W. Adams, and J.J. Collins, *Proc. Natl. Acad. Sci. U.S.A.* **96**, 10450 (1999).
 - [33] A.C. Guyton and J.E. Hall, *Textbook of Medical Physiology*, 9th ed. (Saunders, Philadelphia, 1996).
 - [34] N.G. van Kampen, *Stochastic Processes in Physics and Chemistry* (North-Holland, New York, 1981).
 - [35] H. Risken, *The Fokker-Planck Equation* (Springer, Berlin, 1984).
 - [36] K. Ito, *Nagoya Math.* **1**, 35 (1950).
 - [37] P. Hägggi and H. Thomas, *Phys. Rep.* **88**, 207 (1982).
 - [38] J. Gradišek, S. Siegert, R. Friedrich, and I. Grabec, *Phys. Rev. E* **62**, 3146 (2000).
 - [39] S. Siegert, R. Friedrich, and J. Peinke, *Phys. Lett. A* **243**, 275 (1998).
 - [40] R. Friedrich, S. Siegert, J. Peinke, S. Lück, M.S.M.L.J. Raethjen, G. Deuschl, and G. Pfister, *Phys. Lett. A* **271**, 217 (2000).
 - [41] J. Timmer, *Chaos, Solitons Fractals* **11**, 2571 (2000).
 - [42] P. Bergé, Y. Pomeau, and C. Vidal, *Order within Chaos* (Wiley, New York, 1986).
 - [43] A.L. Goldberger, L.A.N. Amaral, L. Glass, J.M. Hausdorff, P.C. Ivanov, R.G. Mark, J.E. Mietus, G.B. Moody, C.K. Peng, and H.E. Stanley, *Circulation* **101**, e215 (2000).
 - [44] T. Schreiber and A. Schmitz, *Physica D* **142**, 346 (2000).
 - [45] J. Theiler, S. Eubank, A. Longtin, B. Galdrikian, and J.D. Farmer, *Physica D* **58**, 77 (1992).

WAVE PATTERN DYNAMICS IN FLUCTUATING MEDIA*

F. SAGUÉS[†] and S. ALONSO[‡]

*Departament de Química Física, Universitat de Barcelona
Diagonal 647, 08028, Barcelona, Spain*
[†]f.sagues@qf.ub.es
[‡]s.alonso@qf.ub.es

J. M. SANCHO

*Departament d'Estructura i Constituents de la Matèria
Facultat de Física, Universitat de Barcelona, Diagonal 647
08028, Barcelona, Spain*
jmsancho@ecm.ub.es

Analytical and numerical results on the ordering role of external random fluctuations in excitable systems are presented. Our study focuses on a simple model for excitable systems. Regular waves are created and sustained out of noise when the system is forced with random perturbations. Explicit results for the generation and dynamics of rings and targets are presented.

Keywords: Stochastic; excitable media; nonlinear dynamics; target patterns.

1. Introduction

We do know now that stochastic environments or external fluctuations can generate counter-intuitive effects such as ordered macroscopic phases, patterns, regular oscillations, etc.^{1,2} Physical mechanisms of such ordering role of the stochasticity have been elucidated and explained in simple modelizations. The most commonly accepted origin of this unexpected phenomenon is the cooperative interaction between fluctuations, nonlinearities and spatial coupling.

We will focus here in the so-called excitability scenario in which wave propagation appears naturally. There is a rich variety of physical,^{3,4} chemical,^{5,6} or biological⁷ among other systems which present an excitable regime exhibiting wave propagation phenomenology. These systems show a large diversity of spatio-temporal patterns, ranging from planar waves to much more complicated structures such as targets or scroll rings. Similar problems are discussed in the contribution by L. Schimansky-Geier in this paper.

A theoretical modelization based on Stochastic Partial Differential Equations (SPDE) is the most common tool for the description and study of wave dynamics

*This contribution has been prepared to honor the 50th anniversary of Prof. J. Luczka.

in fluctuating media.⁸ The question of integration of SPDE is also presented in the contribution by R. Mannella. Numerical simulations of these type of equations do show clearly the ordering effects induced by noise. Analytical, although nonexact, calculations also prove the possible existence of transitions from disorder to order as the intensity of the fluctuations is increased. This surprising scenario has recently received an important experimental support by a series of experimental evidences of these counter-intuitive ordering effects out of noise under well-controlled laboratory setups.^{9–12}

Our objective in this paper is to present the theoretical approach to SPDE's, with special emphasis in its predictive strength. Numerical simulations are used as a test of the reliability and accuracy of our treatment, because a more rigorous mathematical approach to SPDE's is not yet available.

This paper is organized as follows. In Sec. 2 we present the main aspects of our analytical and numerical methodology. Section 3 contains the explicit results for a very simple modelization of an excitable system. Finally we end up with some conclusions and perspectives.

2. Modelization and Methodology

2.1. Stochastic Partial Differential Equations (SPDE)

The common framework to model pattern formation phenomenology is by the use of partial differential equations (PDE) for the local densities of the material components. The most simple situation which presents waves has two variables called *activator*, $u(\mathbf{x}, t)$, and *inhibitor*, $v(\mathbf{x}, t)$, with different time scales, $u(\mathbf{x}, t)$, is the fast variable. These equations have the general form,

$$\begin{aligned}\partial_t u &= D\nabla^2 u + f_u(u, v, b), \\ \partial_t v &= f_v(u, v),\end{aligned}\tag{1}$$

where f_i are the reactive terms and, quite often, it is assumed that the inhibitor variable diffuses so slowly that one can discard its contribution. The conditions $f_i = 0$ determine the null-clines whose intersection points give the homogeneous stationary states of the system. The relative stability or nature of these points can be obtained by a simple linear analysis. b is an external parameter which controls the excitability properties of the medium. In the experiments on the photosensitive Belousov–Zhabotinsky reaction, the parameter b will represent the intensity of the incident light.^{9–12} This parameter can be handled easily by using opto-electronic devices and, as a consequence, controlled fluctuations can be introduced through it as, $b \rightarrow b + \eta(\mathbf{x}, t)$. Then one can arrive to the following generic system of stochastic partial differential equations (SPDE) which will be the framework of all our studies,

$$\begin{aligned}\partial_t u &= D\nabla^2 u + f_u(u, v, b) + g_u(u)\eta(\mathbf{x}, t), \\ \partial_t v &= f_v(u, v),\end{aligned}\tag{2}$$

where $\eta(\mathbf{x}, t)$ is a Gaussian noise with zero mean and a correlation,

$$\langle \eta(\mathbf{x}', t')\eta(\mathbf{x}, t) \rangle = 2\sigma^2\delta(t - t')\delta(\mathbf{x} - \mathbf{x}'). \quad (3)$$

Now depending on the modelization involved in a particular system, different reactive functions f_i and g_i , are proposed.

The set of Eqs. (2)–(3) with appropriate boundary and initial conditions define the system we want to study. Thus, we deal with nonlinear SPDE's whose analytical solution is impossible. Nevertheless analytical information is highly valuable and, as a consequence, some efforts should be invested in this direction. Numerical simulations of these equations have to complete this study.

2.2. Effective dynamics

Here we will outline the most suitable theoretical approach to understand how ordering effects out of fluctuations could appear. The idea is very simple. The initial conjecture is that fluctuations not only have a dispersive or disordering effects but also the systematic ones. If it is so, one can try to guess where is the source of them. A preliminary analysis of Eq. (2) shows that the noisy term $g(u)_u\eta(\mathbf{x}, t)$ has a nonzero mean value given by:

$$\langle g_u(u)\eta(\mathbf{x}, t) \rangle \equiv \langle \Phi(u) \rangle \neq 0, \quad (4)$$

in spite of the zero average of the noise. We are using the Stratonovich calculus to deal with the multiplicative noise. This is the usual interpretation when we face with realistic noise. The above contribution will be the source of the systematic and quite often ordering effects of the noise.¹ By adding and subtracting $\Phi(u)$ to the equation of motion for u in Eq. (2), we arrive at:

$$\begin{aligned} \partial_t u &= D\nabla^2 u + f_u(u, v, b) + \Phi(u) + R(u, t), \\ \partial_t v &= f_v(u, v). \end{aligned} \quad (5)$$

$R(u, t) = g(u)\eta(\mathbf{x}, t) - \Phi(u)$, is a more complicated random term which has now a zero mean value and whose fluctuating and nonsystematic effects can be safely discarded for not very large noise intensities. Then one arrives to the *effective deterministic model*,

$$\begin{aligned} \partial_t u &= D\nabla^2 u + f_u(u, v, b) + \Phi(u), \\ \partial_t v &= f_v(u, v), \end{aligned} \quad (6)$$

which can be studied using the standard techniques for PDE's. In the explicit example we will study in the next section, the new reactive term $\Phi(u)$ can be absorbed in the old one $f_u(u, v, b)$ through a renormalization of the model parameters in such a way that its systematic influence can be evaluated using already developed techniques for PDE's.

Our analytical approach relays on the evaluation of $\Phi(u)$. This is a simple task for a white noise,¹ but it is much involved for spatio-temporal structured noise.¹³

2.3. Numerical simulations

In order to see how is the phenomenology of systems described by SPDE's such as Eqs. (2) and (3) and also to test the accuracy of the theoretical predictions we have to proceed with the numerical simulation of this type of equations. We will follow the Heun method (a second order Runge–Kutta algorithm) extended for SPDE's.¹ The set of Eqs. (2) and (3) are discretized in a *d-dimensional lattice* with N squared cells, each one of the linear size Δx . The fields $u(\mathbf{x}, t)$ and $v(\mathbf{x}, t)$ transform into N time-dependent variables $u_i(t)$ and $v_i(t)$ where i is the position index. In the discrete lattice we have N couples of ordinary stochastic differential equations. The Laplacian operator transform according to the standard prescription,

$$D\nabla^2 u \rightarrow \mathcal{D}_i(u) = \frac{D}{\Delta x^2} \left(\sum_j u_j(i) - 2du_i \right), \quad (7)$$

where $u_j(i)$ are the $2d$ next neighbors of u_i . The noise is also discretized accordingly, $\eta(\mathbf{x}, t) \rightarrow \eta_i(t)$, with a correlation,

$$\langle \eta_i(t) \eta_j(t) \rangle = 2\sigma^2 \delta(t - t') \frac{\delta_{ij}}{\Delta x^d}. \quad (8)$$

Now the Heun algorithm reads explicitly,

$$\begin{aligned} u_i(t + \Delta t) &= u_i(t) + \frac{\Delta t}{2} (f_u(u, v) + f_u(\tilde{u}, \tilde{v}) + \mathcal{D}_i(u) + \mathcal{D}_i(\tilde{u})) \\ &\quad + \frac{1}{2} (g(u)_u + g(\tilde{u})_u) X_i, \\ v_i(t + \Delta t) &= v_i(t) + \frac{\Delta t}{2} (f_v(u, v) + f_v(\tilde{u}, \tilde{v})), \end{aligned} \quad (9)$$

where the predictor values \tilde{u} and \tilde{v} are obtained from the Euler algorithm,

$$\begin{aligned} \tilde{u}_i &= u_i(t) + \Delta t (f_u(u, v) + \mathcal{D}_i(u)) + g(u)_u X_i, \\ \tilde{v}_i &= v_i(t) + \Delta t f_v(u, v). \end{aligned} \quad (10)$$

X_i is random process given by:

$$X_i = \sqrt{\frac{2\sigma^2 \Delta t}{\Delta x^d}} \gamma_i, \quad (11)$$

where γ_i are Gaussianly distributed random numbers with zero mean and variance equal to 1. This noise prescription generates a Gaussian white noise in a lattice.

The simulations have been done either in a one- or two-dimensional lattices with appropriate Δx and Δt which will be indicated in the figure captions corresponding to the numerical results.

Choosing appropriate initial conditions for each case, respectively a circular spot, ring, spiral or a planar wave, one can observe the dynamics of a particular structure under the presence of the external fluctuations.

3. The Barkley Model

3.1. *Explicit predictions*

Our theoretical approach can be applied to any FitzHugh–Nagumo-like schemes to describe active systems. For the sake of simplicity and unless it is explicitly said, we will use Barkley modelization for a generic active media.¹⁴ This model has simple polynomial reactive terms,

$$\begin{aligned} f_u(u, v, b) &= \frac{1}{\varepsilon} u(1-u) \left(u - \frac{v+b}{a} \right), \\ f_v(u, v) &= u - v, \end{aligned} \quad (12)$$

where ε controls the time scale of the activator and a is another system parameter. Including the fluctuations in b the multiplicative noise reactive term is:

$$g_u(u) = \frac{1}{a\varepsilon} u(1-u). \quad (13)$$

Explicit calculations of the stochastic average defined in Eq. (4), using the Stratonovich interpretation, gives^{1,13}

$$\langle g_u(u)\eta(\mathbf{x}, t) \rangle = C(0)\langle g_u(u)g'_u(u) \rangle, \quad (14)$$

where $C(0) = \sigma^2/\Delta x^2$ is the effective noise intensity in the lattice. This gives, for our model,

$$\Phi(u) = \frac{C(0)}{a^2\varepsilon^2} u(u-1)(2u-1). \quad (15)$$

This systematic contribution is incorporated into the activator equation as a new reactive term. Finally the whole reactive term can be reorganized and it happens that the new effective reactive term is of the same form as the original deterministic one, but with the following new model parameters,

$$a' = a - \frac{2C(0)}{a\varepsilon}, \quad b' = b - \frac{C(0)}{a\varepsilon}, \quad \varepsilon' = \frac{\varepsilon}{1 - 2C(0)/a^2\varepsilon}. \quad (16)$$

As parameter b controls the excitability of the system one can expect important changes. In particular the decrease of b as the noise intensity increases will drive the system to more excitable regimes. These aspects will appear clearly in our simulations.

3.2. *Numerical simulation results*

First we will study the transition between a nonexcitable regime and the excitable one. In a nonexcitable regime, any initial pattern or perturbation will decay to the uniform state $u = v = 0$, and no propagation is observed. Under this conditions, we can see how increasing the intensity of the noise will arrive to an excitable regime in which the initial pattern is sustained and propagates. In Fig. 1 we find this behavior in numerical simulations. The first column in Fig. 1 has been included to

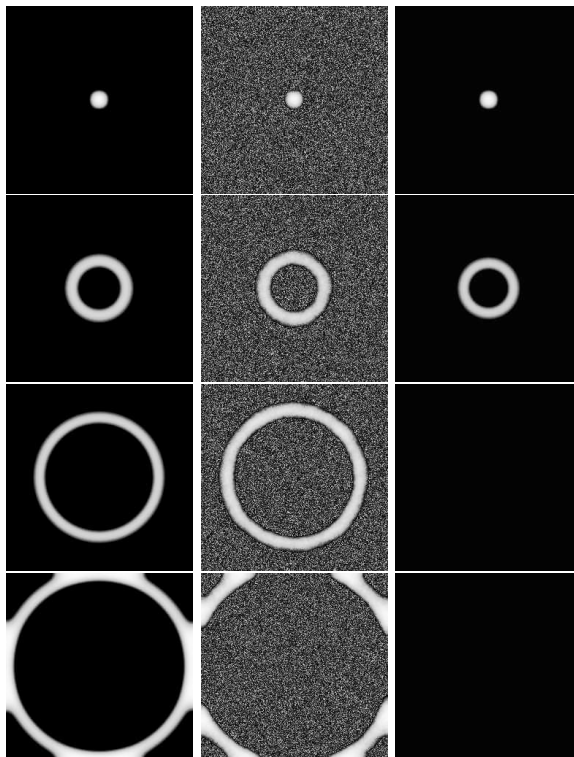


Fig. 1. Two-dimensional sub-excitable system with a circular-like initial condition. The first column corresponds to the effective model with $C(0) = 0.001$. The second one corresponds to the same system with white noise ($\sigma^2 = 0.00001$). The last column corresponds to the deterministic model in the sub-excitable regime. There are 3 t.u. between each snapshot (512×512 pixels, $a = 0.7$, $b = 0.02$, $\epsilon = 0.07$, $\Delta x = 0.1$ s.u., $\Delta t = 0.001$ t.u.).

appreciate the effective model mimics qualitatively and quantitatively the behavior found in simulations.

The transition from an excitable to an oscillatory regime can be predicted from the study of the null-clines. In Fig. 2 plots of the null-clines and stationary points are presented for the deterministic and stochastic effective models.

One can see how the stability of one of the steady points change with the presence of fluctuations. In particular the deterministically stable steady state in an excitable regime transforms, due to the presence of noise in the unstable steady point of an oscillatory regime.

This theoretical prediction has been tested by numerical simulations and a representative evolution is presented in Fig. 3. Here we observe how a system in an excitable regime of expanding rings without noise, changes to an oscillatory regime with concentric rings (targets) when noise is present. As in the former case, the first column in Fig. 3 shows that the effective deterministic model explains indeed this result.

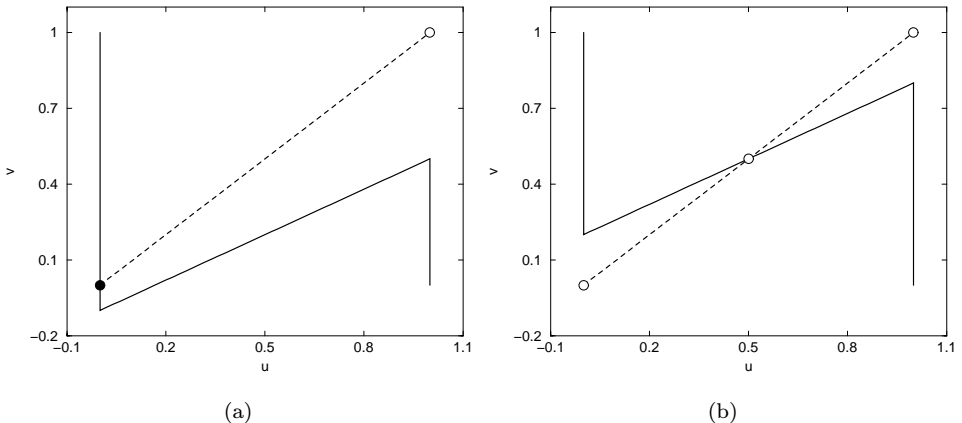


Fig. 2. (a) Null-clines of the deterministic model (12). (b) Null-clines of the effective deterministic model: Eq. (12) with parameters (16). Empty circles are the unstable steady points and full circles are the stable ones.

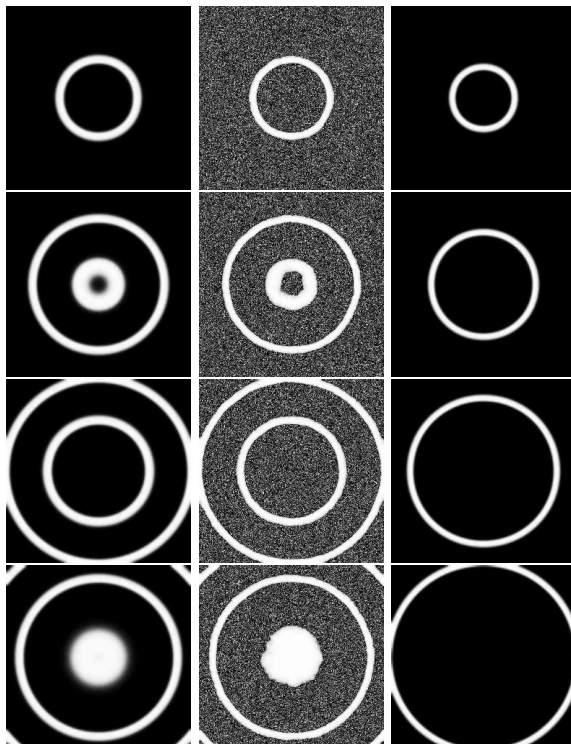


Fig. 3. Two-dimensional excitable system with a circular-like initial condition. The first column corresponds to the effective model with $C(0) = 0.001$. The second one corresponds to the same system with white noise ($\sigma^2 = 0.00001$). The last column represents the evolution of the deterministic model in the excitable regime. The snapshots are taken at 0.03, 0.09, 0.15, and 0.18 t.u. respectively. (256 \times 256 pixels, $a = 0.7$, $b = 0.02$, $\epsilon = 0.04$, $\Delta x = 0.1$ s.u., $\Delta t = 0.001$ t.u.).

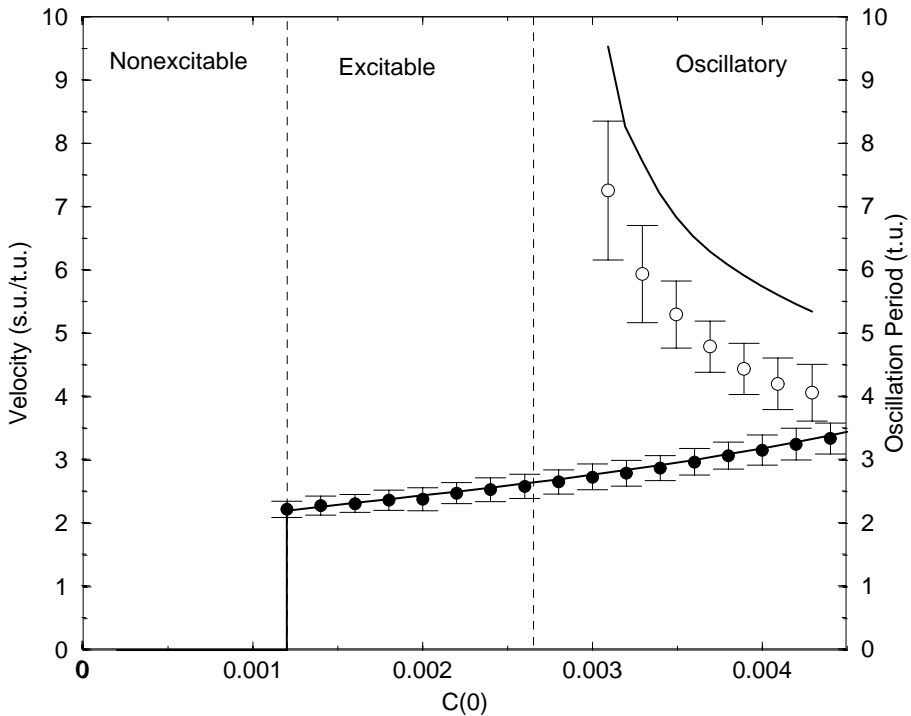


Fig. 4. Mean velocity (\bullet) and mean oscillatory period (\circ) of noisy wave trains on a one-dimensional nonexcitable media versus the noise intensity. Points calculated with an average of 25 realizations. Velocities and periods correspond to the effective model with the renormalized values of the parameter, Eqs. (12)–(16) (—). Parameters of the model are: $a = 0.7$, $b = 0.02$, $\epsilon = 0.04$, $\Delta x = 0.1$ s.u., $\Delta t = 0.001$ t.u.. Vertical lines show the transitions among different kinds of excitability regimes.

In order to characterize in a more quantitative form the transitions we have identified before, we have to choose a kind of order parameter whose drastic change would indicate the transition points. The transition from nonexcitable to excitable conditions can be defined quite easily by looking at the velocity of the wave: zero in the nonexcitable regime and nonzero in the excitable one. This criteria is useless to find the transition to the oscillatory regime. For this case we choose the period of the oscillations, or for practical purpose, the interval of time between two consecutive waves in a wave train. This period is not defined in nonexcitable and excitable regimes but it is finite in the oscillatory regime, diverging at the transition point. This analysis is shown in Fig. 4, by using numerical simulation data in one-dimensional systems from the stochastic and effective models. These two transitions appear clearly and the effective model gives very reliable results. Main differences appear in the oscillatory regime due to the very large noise intensities used.

In all the cases if noise is switched off then the properties of the pattern recover the regime of the noise-free system.

4. Conclusions and Perspectives

We have shown analytically and numerically that noise modeled in terms of Stochastic Partial Differential Equation can produce ordering effects. We have focussed our study on excitable model systems. Theoretical predictions have been checked satisfactorily by numerical simulations. Our results are not restricted to nonexcitable-excitabile-oscillatory transitions. Recently we have proved that external fluctuations can also control a transition between bistable and excitable regimes.¹⁵

It is worth to comment here that in our analytical study we have assumed that the external noise is white in time and in space. This assumption has no problems in the lattice, but in the continuum description a colored noise in space has to be considered instead.

Certainly white noise assumption is a drastic simplification of the spatio-temporal structured nature of fluctuations in real experiments. Nevertheless experimental evidence of these noisy effects have been also tested in chemical experiments with the Belousov-Zhabotinsky reaction and, of course, with truly realistic noises.¹² The theoretical analysis of this problem with real fluctuations or spatio-temporal structured noise has been done in Ref. 16.

Thus we can conclude that the ordering effects of the external fluctuations are not a academic result but a real fact in nature.

Acknowledgment

We acknowledge financial support from the Dirección General de Enseñanza Superior (Spain) under projects BFM2000-0624 and BXX2000-0638.

References

1. J. García-Ojalvo and J. M. Sancho, *Noise in Spatially Extended Systems* (Springer-Verlag, New York, 1999).
2. T. Shinbrot and F. J. Muzzio, *Nature* **410**, 251 (2001).
3. G. Giacomelli, M. Giudici, S. Balle, and J. R. Tredicce, *Phys. Rev. Lett.* **84**, 3298 (2000).
4. J. M. Buldú, J. Garcí-Ojalvo, C. R. Mirasso, M. C. Torrent, and J. M. Sancho, *Phys. Rev. E* **64**, 051109 (2001).
5. A. N. Zaikin and A. M. Zhabotinskii, *Nature* **225**, 535 (1970).
6. R. Kapral and K. Showalter, *Chemical Waves and Patterns* (Kluwer, Dordrecht, 1995).
7. A. Goldbeter, *Biochemical Oscillations and Cellular Rhythms* (Cambridge Univ. Press, Cambridge, UK, 1996).
8. A. S. Mikhailov, *Phys. Rep.* **184**, 307 (1989).
9. S. Kádár, J. Wang, and K. Showalter, *Nature* **391**, 770 (1998).
10. I. Sendiña-Nadal, A. P. Muñozuri, D. Vives, V. Pérez-Muñozuri, J. Casademunt, L. Ramírez-Piscina, J. M. Sancho, and F. Sagués, *Phys. Rev. Lett.* **80**, 5437 (1998).
11. I. Sendiña-Nadal, S. Alonso, V. Pérez-Muñozuri, M. Gómez-Gesteira, V. Pérez-Villar, L. Ramírez-Piscina, J. Casademunt, J. M. Sancho, and F. Sagués, *Phys. Rev. Lett.* **84**, 2734 (2000).
12. S. Alonso, I. Sendiña-Nadal, V. Pérez-Muñozuri, J. M. Sancho, and F. Sagués, *Phys. Rev. Lett.* **87**, 078302 (2001).

13. M. A. Santos and J. M. Sancho, *Phys. Rev. E* **64**, 016129 (2001).
14. D. Barkley, M. Kenss, and L. S. Tuckerman, *Phys. Rev. A* **42**, 2489 (1990).
15. J. García-Ojalvo, F. Sagués, J. M. Sancho, and L. Schimansky-Geier, *Phys. Rev. E* **65**, 011105 (2002).
16. S. Alonso, F. Sagués, and J. M. Sancho, *Phys. Rev. E* **65**, 066107 (2002).